FRAGILITY CURVES OF REINFORCED-CONCRETE BUILDINGS UNDER TSUNAMI LOADINGS

Mr. Piyawat Foytong

A Dissertation Submitted in Partial Fulfillment of the Requirements
for the Degree of Doctor of Philosophy Program in Civil Engineering
Department of Civil Engineering
Faculty of Engineering
Chulalongkorn University
Academic Year 2012

เส้นโค้งความบอบบางของอาคารคอนกรีตเสริมเหล็กภายใต้แรงสึนามิ

นายปิยะวัชร ฝอยทอง

วิทยานิพนธ์นี้เป็นส่วนหนึ่งของการศึกษาตามหลักสูตรปริญญาวิศวกรรมศาสตรดุษฎีบัณฑิต

สาขาวิชาวิศวกรรมโยธา ภาควิชาวิศวกรรมโยธา

คณะวิศวกรรมศาสตร์ จุฬาลงกรณ์มหาวิทยาลัย

ปีการศึกษา 2555

Thesis Title	FRAGILITY CURVES OF REINFORCED-CONCRETE BUILDINGS UNDER TSUNAMI LOADINGS
By	Mr. Piyawat Foytong
Field of Study	Civil Engineering
Thesis Advisor	Assistant Professor Anat Ruangrassamee, Ph.D.
Thesis Co-advisor	Professor Panitan Lukkunaprasit, Ph.D.

Accepted by the Faculty of Engineering, Chulalongkorn University in Partial Fulfillment of the Requirements for the Doctoral Degree

…… Dean of the Faculty of Engineering
(Associate Professor Boonsom Lerdhirunwong, Dr.Ing.)

THESIS COMMITTEE

…… Chairman
(Assistant Professor Chatpan Chintanapakdee, Ph.D.)

…… Thesis Advisor
(Assistant Professor Anat Ruangrassamee, Ph.D.)

…… Thesis Co-advisor
(Professor Panitan Lukkunaprasit, Ph.D.)

…… Examiner
(Professor Teerapong Senjuntichai, Ph,D.)

…… Examiner
(Assistant Professor Withit Pansuk, Ph,D.)

…… External Examiner
(Associate Professor Pennung Warnitchai, Ph.D.)

ปิยะวัชร ฝอยทอง : เส้นโค้งความบอบบางของอาคารคอนกรีตเสริมเหล็กภายใต้แรงสึนามิ. (FRAGILITY CURVES OF REINFORCED-CONCRETE BUILDINGS UNDER TSUNAMI LOADINGS) อ.ที่ปรึกษาวิทยานิพนธ์หลัก: ผศ.ดร.อาณัติ เรืองรัศมี, อ.ที่ปรึกษาวิทยานิพนธ์ร่วม: ศ.ดร .ปณิธาน ลักคุณะประสิทธิ์, 153 หน้า.

เหตุการณ์สึนามิได้สร้างความเสียหายต่ออาคารบ้านเรือนและคร่าชีวิตผู้คนจำนวนมากในหลายประเทศในโลก ในการป้องกันและบรรเทาความเสียหายต่อโครงสร้างในอนาคต จำเป็นต้องเข้าใจผลตอบสนองของอาคารภายใต้แรงสึนามิและการพัฒนาเส้นโค้งความบอบบาง ในปัจจุบันเส้นโค้งความบอบบางที่ถูกพัฒนาจากข้อมูลสำรวจในสนามและการสำรวจจากระยะไกลนั้นไม่เพียงพอที่จะแสดงถึงพฤติกรรมของโครงสร้างในรายละเอียด ดังนั้นในการศึกษานี้จึงได้ทำการวิเคราะห์ผลตอบสนองของอาคารตัวแทนซึ่งเป็นอาคารคอนกรีตเสริมเหล็กสูงหนึ่งชั้นเพื่อศึกษาพฤติกรรมของอาคารภายใต้แรงสึนามิและพัฒนาเส้นโค้งความบอบบางจากการวิเคราะห์อาคารโดยละเอียด

ในขั้นต้นได้ทำการวิเคราะห์ความเร็วกระแสน้ำซึ่งเป็นปัจจัยหลักในการคำนวนค่าแรงอุทกพลวัตจากภาพโทรทัศน์ที่บันทึกเหตุการณ์สึนามิที่ชายฝั่งตะวันออกของประเทศญี่ปุ่นในเดือนมีนาคม ปีพ.ศ. 2554 โดยค่าความเร็วกระแสน้ำจากการวิเคราะห์อยู่ในช่วง $1.0\sqrt{gh}$ ถึง $1.5\sqrt{gh}$

แบบจำลองอาคารตัวแทนได้ถูกสร้างขึ้นจากค่าเฉลี่ยของดัชนีโครงสร้างของอาคารบ้านพักอาศัยในภาคใต้ของประเทศไทยและได้สอบเทียบแบบจำลองกับผลการทดสอบของอาคารสำนักงานกรมอุตุนิยมวิทยาซึ่งเป็นอาคารคอนกรีตเสริมเหล็กสูงหนึ่งชั้นโดยใช้แบบจำลองอาคาร 3 มิติ โดยได้จำลองกำแพงก่ออิฐเป็นสปริงในแนวราบและได้จำลองจุดหมุนแบบพลาสติกด้วยชิ้นส่วนไฟเบอร์ที่มีพฤติกรรมแบบไม่เชิงเส้น จากผลการวิเคราะห์พบว่าค่าสตีฟเนสเริ่มต้นและการเสียรูปของอาคารสอดคล้องกับผลการทดสอบ

ผู้วิจัยได้วิเคราะห์อาคารตัวแทนเพื่อศึกษาผลตอบสนองภายใต้แรงอุทกพลวัตจากสึนามิ โดยในแต่ละความสูงน้ำท่วมได้ให้แรงกระทำด้านข้างเพิ่มขึ้นเรื่อยๆจนกระทั่งอาคารวิบัติ จากผลการวิเคราะห์พบว่าที่ระดับความสูงน้ำท่วมระดับต่ำกว่า 2.57 เมตร อาคารวิบัติเนื่องจากการเฉือนในเสา และเมื่อความสูงน้ำท่วมสูงขึ้นตำแหน่งของแรงกระทำจึงเคลื่อนสูงขึ้นตามและอาคารเกิดการวิบัติเนื่องจากการดัด เมื่อระดับความสูงสึนามิถึงระดับคานพบว่าการวิบัติเนื่องจากการดัดสามารถเกิดขึ้นที่ค่าความเร็วกระแสน้ำต่ำกว่า $0.7\sqrt{gh}$ นอกจากนั้นยังพบว่ากำแพงอิฐช่วยเพิ่มความต้านทานด้านข้างของอาคารซึ่งแสดงในรูปแบบของค่าโมเมนตัมการไหลของแรงอุทกพลวัตที่กระทำต่ออาคาร ในการพัฒนาเส้นโค้งความบอบบางได้พิจารณาความไม่แน่นอนของกำลังอัดของคอนกรีตโดยให้มีการกระจายตัวแบบปรกติและค่าความเร็วกระแสน้ำที่พิจารณาอยู่ในช่วง $0.7\sqrt{gh}$ ถึง $2.0\sqrt{gh}$ จากเส้นโค้งความบอบบางที่สร้างขึ้นแสดงให้เห็นว่าอาคารไม่เกิดการวิบัติที่ระดับความสูงน้ำท่วมต่ำกว่า 1.8 เมตร แต่จะเกิดการวิบัติเมื่อความสูงน้ำท่วมสูงกว่า 3.2 เมตร

ภาควิชา …วิศวกรรมโยธา…… ลายมือชื่อนิสิต ……..

สาขาวิชา …วิศวกรรมโยธา…….. ลายมือชื่อ อ.ที่ปรึกษาวิทยานิพนธ์หลัก …….

ปีการศึกษา …2555…… ลายมือชื่อ อ.ที่ปรึกษาวิทยานิพนธ์ร่วม ……..

5071854721 : MAJOR CIVIL ENGINEERING

KEYWORDS: TSUNAMI / REINFORCED-CONCRETE BUILDING / BUILDING RESPONSES / FRAGILITY CURVE /

PIYAWAT FOYTONG: FRAGILITY CURVES OF REINFORCED-CONCRETE BUILDINGS UNDER TSUNAMI LOADINGS. ADVISOR: ASST. PROF. ANAT RUANGRASSAMEE, Ph.D., CO-ADVISOR: PROF. PANITAN LUKKUNAPRASIT, Ph.D., 153 pp.

Tsunamis caused damage to many buildings and killed people in many countries in the world. To prevent and reduce structural damage in the future, the understanding of building responses under tsunamis and the development of fragility curves are needed. The fragility curves currently developed from field observations and remote sensing are insufficient to represent structural behaviors in details. In this study, the responses of a generic one-story reinforced concrete building are analyzed to understand behaviors of a building under tsunami loading. Then, the tsunami fragility curve is developed from a series of detailed analyses.

The tsunami flow velocity, which is a key parameter in determining hydrodynamic force, is studied by analyzing videos recorded in the March 2011 Tohoku, Japan tsunami. The analyzed velocities fall in the range of $1.0\sqrt{gh}$ to $1.5\sqrt{gh}$.

A generic building model is developed from the average values of the structural indices of residential houses in Southern Thailand. The components of the building model are calibrated with experimental results. The 3-dimensional building model of the former office of Thai Meteorological Department, which is a one-story reinforced-concrete building, is analyzed. In the building model, masonry infill walls are idealized as horizontal springs, and plastic hinges are modeled by non-linear fiber elements. The good agreement between the test and analysis is obtained in terms of initial stiffness and deformations.

The generic building is analyzed to capture responses under tsunami hydrodynamic forces. At each inundation depth, the lateral force is increased until collapse. From the analysis results, the resistance of the building is controlled by the shear failure of columns at inundation depths lower than 2.57 m. As an inundation depth increases, locations of loads move higher and the flexural failure occurs in the building. When the tsunami reaches the beam level, the flexural failure occurs even at the tsunami flow velocity lower than $0.7\sqrt{gh}$. For the building responses with masonry infill walls, walls enhance the lateral resistance represented in terms of the momentum flux of the hydrodynamic force acting on the building. In developing the fragility curve, the uncertainty of compressive strengths of concrete is assumed as the normal distribution, and the tsunami flow velocity is considered in the range from $0.7\sqrt{gh}$ to $2.0\sqrt{gh}$. The developed tsunami fragility curve shows that the building does not collapse for an inundation depth less than 1.8 m and collapses for an inundation depth higher than 3.2 m.

Department:…Civil Engineering…… Student's Signature ……..

Field of Study:…Civil Engineering……. Advisor's Signature ……..

Academic Year:…2012…… Co-advisor's Signature……..….

ACKNOWLEDGEMENTS

I would strongly express his deepest gratitude to my advisor, Asst. Prof. Anat Ruangrassamee for his experienced suggestions, kindness, support and patience while I did research. I wish to express to him all my gratitude. I would also like to thank Prof. Panitan Lukkunaprasit and Assoc. Prof. Gaku Shoji for their valuable suggestions and comments.

I am grateful for the financial support granted by the Office of the Higher Education Commission, Ministry of Education, Thailand. With this fund, I had an opportunity to conduct research at University of Tsukuba, Japan for 7 months, under the supervision of Assoc. Prof. Gaku Shoji, an expert in this research area. I am deeply grateful for his guidance and support.

I highly appreciate Asst. Prof. Chatpan Chintanapakdee to be a chair, Prof. Teerapong Senjuntichai, Assoc. Prof. Pennung Warnitchai and Asst. Prof. Withit Pansuk to be committees of my thesis defense. Their suggestions and comments help this research more completely.

Finally, special thanks go to my family for their support throughout my life. The members of Center of Excellence on Earthquake Engineering and Vibration, Chulalongkorn University is also acknowledged. Especially, Dr. Nuttawut Thanasisathit for his suggestions and testing of the masonry prisms is highly appreciated. Mr. Witsarut Prasertsukhum and Mr. Chisanuphong Suthumma for their testing of reinforcements are also appreciated.

CONTENTS

Page

Page

Page

LIST OF TABLES

page

page

page

LIST OF FIGURES

Page

Page

Page

Page

Page

Page

Page

CHAPTER I
INTRODUCTION

1.1 Problem Statement

On the December 26, 2004, the earthquake with a magnitude of 9.1 occurred at the North of Sumatra Island, Indonesia as shown in Figure 1-1. This earthquake event generated the uplift of the sea bottom which caused the 2004 Indian Ocean tsunami. The December 26, 2004 Indian Ocean tsunami caused serious damage to many buildings and killed many people in the Indian Ocean countries and also the Western coastal in the South of Thailand. In Table 1-1, the effects of 2004 Indian Ocean tsunami to people and buildings are summarized. In recent years, two major tsunamis, which are the 2009 Samoa tsunami and the 2011 Tohoku Japan tsunami, had occurred. The 2009 Samoa tsunami caused damage in Samoa, American Samoa and Tonga. More than 189 people had been killed and many buildings were damaged (USGS, 2009 : online). For the 2011 Tohoku Japan tsunami, the unexpected earthquake with a magnitude of 9.0 occurred near East coast of Honshu, Japan on March 11, 2011 (USGS, 2011 : online). The 2011 Tohoku Japan earthquake epicenter is shown in Figure 1-2. The devastating tsunami was generated and attacked the East coast of Japan with the maximum height of about 40 m at Omoe-Aneyoshi area, Miyako city (JMA, 2011). About 20,000 people were killed and about 830,000 construction buildings were damaged.

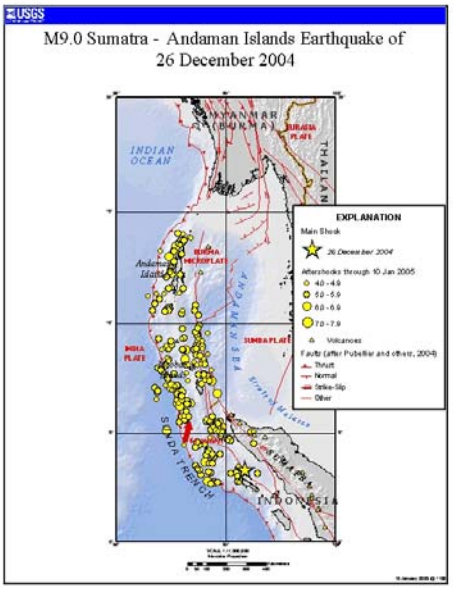

Figure 1-1. 2004 Indian Ocean earthquake epicenter and after shock (USGS, 2004 : online)

Table 1-1. Effects of the 2004 Indian Ocean Tsunami to people and residency (http://www.disaster.go.th)

Province	People		Residency (buildings)		Total (buildings)
	Persons	Family	Whole	Partial	
Phung-Nga	19,509	4,394	1,904	604	2,508
Krabi	15,812	2,759	396	262	658
Phuket	13,065	2,616	742	291	1,033
Ranong	5,942	1,509	224	111	335
Trung	1,302	1,123	34	156	190
Satun	2,920	414	2	80	82
Total	58,550	12,815	3,302	1,504	4,806

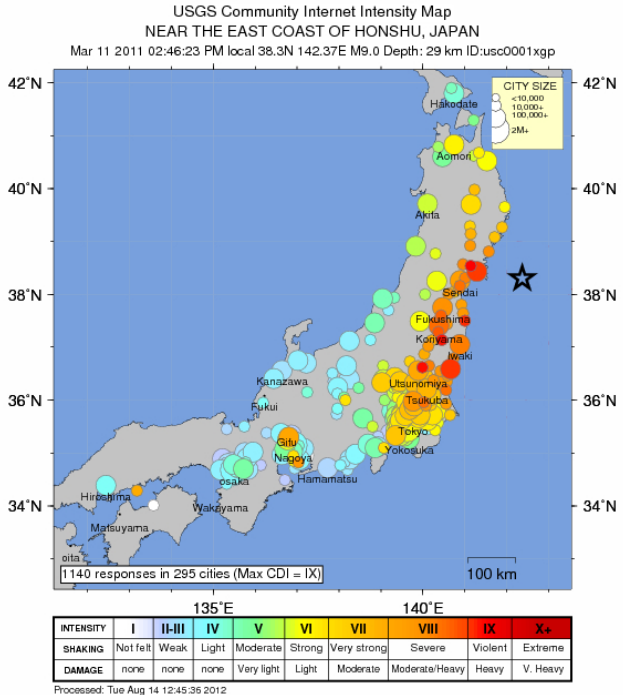

Figure 1-2. 2011 Tohoku, Japan earthquake epicenter and after shock (USGS, 2011 : online)

To prevent and reduce residential damage in the future, the understanding of building responses under tsunamis and the study of tsunami risk analysis for evacuation planning, loss estimation and structural damage estimation are needed. Currently, the risk assessment in the seismic field has been developed for many years. The primary components of risk assessment are hazard, fragility curves and structural inventory. The tsunami fragility curves from field observations and remote sensing are developed by several researches. The tsunami fragility curves are insufficient to present structural behaviors in details. The analytical fragility curve for tsunami has not been developed so far. Hence, the analytical tsunami fragility curve is developed for reinforced concrete in this study.

1.2 Research Objectives

The objectives of this research are

1) To investigate the tsunami flow velocities on land,
2) To study behaviors and responses of a reinforced-concrete building under lateral tsunami loading,
3) To analyze failure modes and load distribution of a reinforced-concrete building under lateral tsunami loading and
4) To develop the tsunami fragility curve for a one-story reinforced-concrete building.

1.3 Scopes

The scopes of this study are as follows

1) Building responses are analyzed by static pushover analysis of 3-dimensional non-linear fiber models,
2) A tsunami fragility curve is developed for a one-story reinforced-concrete building with non-load carrying walls and
3) Hydrodynamic forces are considered as lateral forces to the model.

1.4 Research Methodology

The methodology of this study is shown in Figure 1-3. The building responses are analyzed under the tsunami hydrodynamic forces acting on the building model calibrated by test results. The possible ranges of the tsunami flow velocities used in this study are discussed in Chapter 3. To analyze the building responses from the building model, the components of building are modeled and calibrated with experimental results. The calibration of building models is performed by 3-dimensional non-linear static pushover analysis using a nonlinear finite element program TDAPIII (ARK Information System, 2008) as discussed in Chapter 4. The building for analysis is developed by using structural indices from building construction drawings in Phuket province, Thailand. The generic building is a one-story reinforced-concrete building used to analyze building responses under tsunami loading and to develop the tsunami fragility curve as described in Chapter 5. The responses of the generic building are analyzed under tsunami loading in Chapter 6.

The effects of compressive strengths of concrete on the building responses are considered. The responses of building are used to develop the analytical tsunami fragility curve in Chapter 7. The analytical tsunami fragility curve is developed by considering the uncertainties of tsunami flow velocities and compressive strengths of concrete.

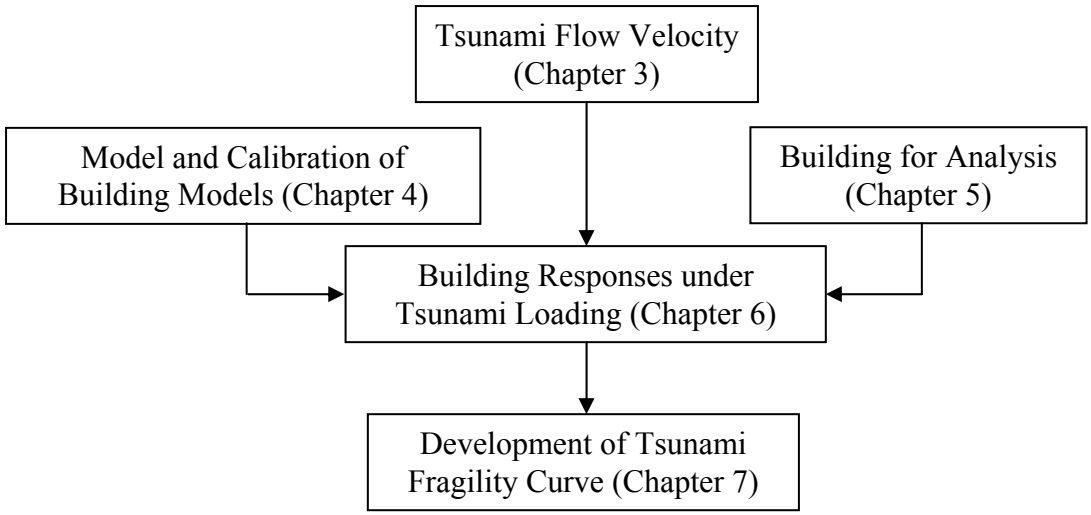

Figure 1-3. Research methodology

CHAPTER II
LITERATURE REVIEWS

2.1 Tsunami Force Acting on Onshore Buildings

Ramsden and Raichlen (1990) investigated forces acting on the vertical wall due to a bore from experiments. A tilting wave tank was used to generate the bore. 6 experimental cases were investigated with variation of the initial relative wave heights, H_0 / d_0, as described in Figure 2-1. From experimental results, the maximum force occurred after the occurrence of the maximum runup in all cases. The forces are calculated by using the measured runup and assuming hydrostatic distribution as expressed in equation 2-1. The measured forces were smaller than the calculated forces for nondimensional times, tc / H_1, less than 11, but agreed well beyond the value, where t is time (s), c is bore velocity and H_1 is incident bore height. However, the measured forces agreed well with the forces calculated by the equation proposed by Cross (1967) as in equation 2-2. They also proposed that the celerity coefficient, $N_F = c / \sqrt{gH_1}$, should be 1.55 for a smallest bore and should be 1.8 for other bores. The forces on the vertical wall due to bores varied from 5.5 to 7 times hydrostatic forces.

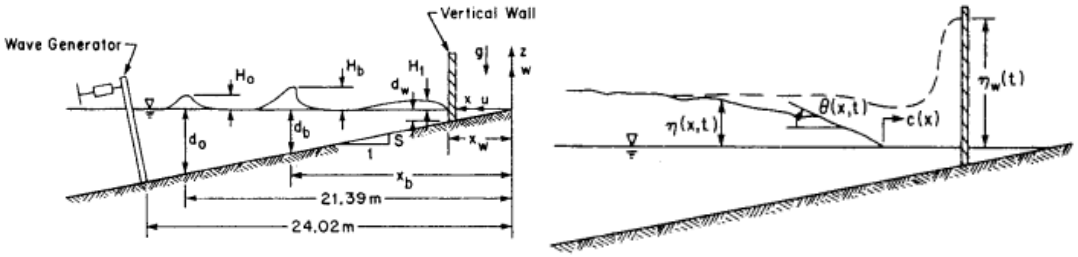

(a) Overview and definition sketch (b) Expanded view of incident bore

Figure 2-1. Experimental setup and parameters (Ramsden and Raichlen, 1990)

$$F = \frac{1}{2} b\gamma \left(\eta_w + d_w\right)^2 \tag{2-1}$$

$$F_T = \frac{1}{2}\gamma b\left(\eta + d_w\right)^2 + \frac{\gamma}{g} C_F b c^2 \left(\eta\right) \tag{2-2}$$

where

C_F is force coefficient $= 1 + \left(\tan\theta\right)^{1.2}$,

d_w is still water level from vertical wall level = 5 mm,

b is the width of the vertical wall,

γ is the distance above the base of the structure to the center of force.
g is the width of the vertical wall,

Ramsden (1996) investigated forces and moments on a vertical wall due to impact of long waves, bores impact and dry-bed surges from the experiments. The empirical formulas, for computing the maximum force and the maximum moment were also proposed. The proposed empirical formulas were a function of the ratio of a wave height and a still-water depth. The proposed empirical formulas in equation 2-3 and equation 2-4 were appropriate for mild beach slopes. As illustrated in Figure 2-2, the maximum forces, F , and the maximum moments, M , from the experiments were less than that from the calculation in the case of strong turbulent bores. For undular bores, they agreed well with results calculated by solitary wave theory proposed by Su and Mirie (1980).

$$\frac{F}{F_i} = 1.325 + 0.347\left(\frac{H}{h}\right) + \frac{1}{58.5}\left(\frac{H}{h}\right)^2 + \frac{1}{7160}\left(\frac{H}{h}\right)^3 \tag{2-3}$$

$$\frac{F}{F_i} = 1.325 + 0.347\left(\frac{H}{h}\right) + \frac{1}{58.5}\left(\frac{H}{h}\right)^2 + \frac{1}{7160}\left(\frac{H}{h}\right)^3 \tag{2-4}$$

where

F_i is linear force scale $= \frac{1}{2}\rho g b\left(2H + h_w\right)^2$,

M_i is moment of runup of $2H$ on the wall $= \frac{1}{6}\rho g b\left(2H + h_w\right)^3$

H is wave height
h is still-water depth
h_w is water depth at wall location
b is width of the wall.

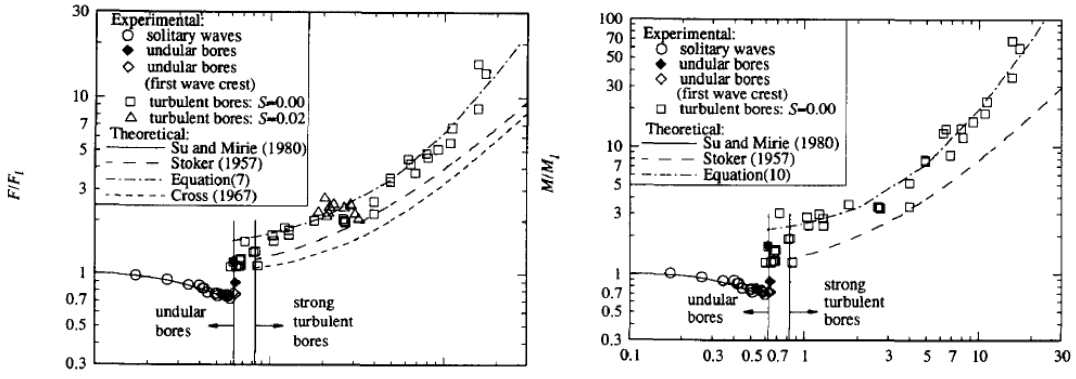

(a) Maximum forces (b) Maximum moments

Figure 2-2. Maximum forces and maximum moments on the vertical wall due to undular bore and bore impact (Ramsden, 1996)

Hamzah et al. (2000) estimated the hydrodynamic pressure of bored waves on the barrier. The experimental results were obtained from a 50 m long, 1 m wide and 1.5 m depth wave flume. From the experiments, two peak pressures were observed. The first peak was the impulsive pressure, and another peak indicated a hydrodynamic pressure distribution. The 2-D and 3-D numerical results were also considered. The experimental results and numerical results agreed well, except for the impulsive pressure.

FEMA 55 (2000) proposed formulas used to calculate design forces for floods. The flood loads consist of a hydrostatic force, a breaking wave force, a hydrodynamic force and a debris impact force. A hydrostatic force for standing or slowly moving water was proposed as equation 2-5. The hydrostatic pressure distributes as a triangle pressure as illustrated in Figure 2-3 and a resultant force act on 2/3 below the still water level.

$$F_{sta} = \frac{1}{2}\rho g d_s^2 w \tag{2-5}$$

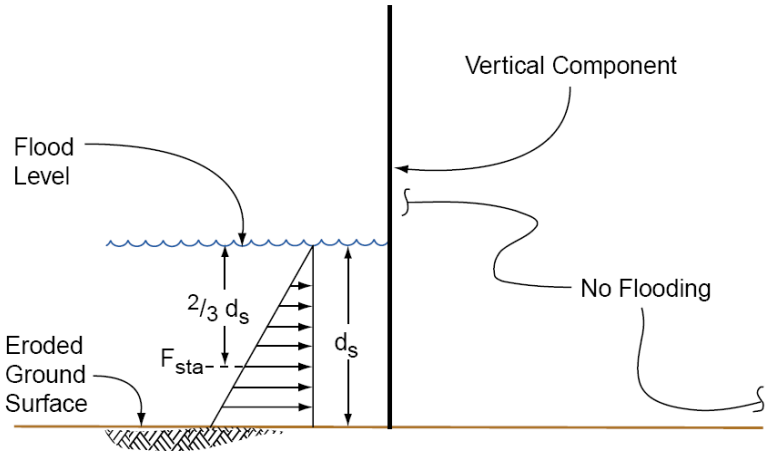

Figure 2-3. The hydrostatic pressure act on vertical surface (FEMA 55, 2000)

The formula for a hydrodynamic force or a drag force, which caused by the velocity, was proposed as equation 2-6. The hydrodynamic force for a flow velocity less than 3 m/s was converted to hydrostatic force, so the resultant force acted at the point 2/3 below the still water surface. For the flow velocity grater than 3 m/s, the resultant force was proposed acting on the middle of the flood depth due to the uniform flow. The velocity of the flood flow for a tsunami was proposed as equal to $2\sqrt{gd_s}$. The flood load combination acting on buildings was also proposed as the combination of the hydrostatic force and the hydrodynamic force.

$$F_D = \frac{1}{2} C_D \rho v^2 d_s w \tag{2-6}$$

where

F_{sta} is hydrostatic force per unit width on the surface,

F_D is hydrodynamic force per unit width on the surface,

d_s is still water flood depth,

ρ is water density,

g is gravitational acceleration,

v is velocity of flood flow,

C_D is drag coefficient (1.2 for circular piles, 2.0 for square piles, for large obstructions are given as Table 2-1),

w is width of structure.

Table 2-1. Drag coefficient for the ratio of the width of large obstructions to flood depth (FEMA 55, 2000)

Width to depth ratio (w/d_s)	Drag coefficient
1-12	1.25
13-20	1.30
21-32	1.40
33-40	1.50
41-80	1.75
81-120	1.80
>120	2.00

CCH (2000) proposed formulas to calculate the design forces for flood. A hydrostatic force was proposed as equation 2-7. The hydrostatic force always acts perpendicularly on the surface. The force resultant was proposed as equation 2-8 which is a distance above the base of flood.

$$F_{sta} = \frac{1}{2} \rho g \left\{ h + \frac{u_p^2}{2g} \right\}^2 \tag{2-7}$$

$$h_r = \frac{1}{3} \left\{ h + \frac{u_p^2}{2g} \right\} \tag{2-8}$$

For a hydrodynamic force or drag force caused by the velocity of flood flow around an object, proposed formula is shown as equation 2-9. Due to the uniform flow, the resultant force was proposed at the middle of the flood depth. The flood flow velocity was defined equal to the depth of water at the structure location.

$$F_D = \frac{1}{2} \rho C_D A u^2 \tag{2-9}$$

Moreover, a surge force on a vertical wall per unit width was also proposed and calculated as equation 2-10. The resultant force was defined at a distance h above the base of the wall. The height of a wall has to be equal or higher than $3h$

$$F_S = 4.5\rho g h^2 \tag{2-10}$$

where

F_{sta} is hydrostatic force per unit width on the surface,

F_D is hydrodynamic force,

F_S is surge force,

ρ is water density,

g is gravitational acceleration,

h is water depth,

u is velocity of flood flow,

u_p is velocity of flood flow on the perpendicular to the surface,

h_r is distant of resultant force above the base of flood,

C_D is drag coefficient (1.0 for circular piles, 2.0 for square piles, 1.5 for wall sections),

A is projection area perpendicularly with flow direction.

Asakura et al. (2002) proposed formulas to calculate the tsunami wave force acting on land structures based on experimental results. Two kinds of wave were considered which were a wave with fission and a wave without fission. Three forces and three moments acting on the rigid model were measured by pressure gauges and a six-component force sensor. The definition of inundation depth is illustrated in Figure 2-4 for both the wave with fission and the wave without fission. For the wave without fission, the distribution of dimensionless maximum wave pressure was linear as shown in Figure 2-5(a). And Figure 2-5(b) shows the distribution of the dimensionless maximum wave pressure for the wave with fission which can be expressed by a bilinear relationship. For the wave without fission, the dimensionless maximum wave pressure could be evaluated by equation 2-11.

$$\frac{P_{\max}}{\rho g \eta_{\max}} = \alpha - \frac{Z}{\eta_{\max}} \tag{2-11}$$

(a) The wave without fission (b) The wave with fission

Figure 2-4. The definition of inundation depth (Asakura et al., 2002)

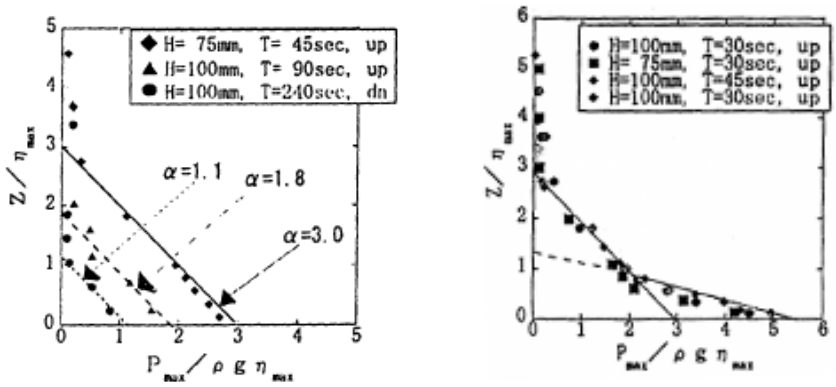

(a) The wave without fission (b) The wave with fission

Figure 2-5. The dimensionless maximum wave pressure distribution (Asakura et al., 2002)

Because the maximum pressure of the pressure gauges did not occur at the same time, the maximum wave force on the model was considered. From Figure 2-5(a), for the wave without fission, the maximum horizontal wave force was proposed as equation 2-12 that is nine times of the hydrostatic force. The measured maximum wave force was less than the computed maximum wave pressure about 20%.

$$F_x = \frac{1}{2} 3\eta_{\max} \cdot 3\rho g \eta_{\max} = \frac{9}{2} \rho g \eta_{\max}^2 \tag{2-12}$$

The dimensionless maximum wave pressure for the wave with fission was proposed by a bilinear relationship as equation 2-13. The second term of equation 2-13 expresses the result of fission wave pressure which exerts the large pressure at the lower part of the model. In the case of $\alpha = 3$, the maximum pressure was calculated by equation 2-14.

$$\frac{P_{\max}}{\rho g \eta_{\max}} = \max\left(\alpha - \frac{Z}{\eta_{\max}}, 1.8\alpha - \frac{4Z}{\eta_{\max}} \right) \tag{2-13}$$

$$\frac{P_{\max}}{\rho g} = \max\left(3\eta_{\max} - Z, 5.4\eta_{\max} - 4Z \right) \tag{2-14}$$

where

$P_{\max}$ is maximum wave pressure,
ρ is density of water,
g is gravitational acceleration,
$\eta_{\max}$ is maximum inundation depth,
Z is vertical distance from the ground level to the measurement point,
α is determined intensity of wave pressure parameter.

Okada et al. (2005) proposed a guideline of a structural design for tsunami refuge buildings. The tsunami wave pressures and forces were calculated as a function of the maximum inundation depth and perpendicularly flow to the buildings without obstructions. The tsunami wave pressure was assumed as a hydrostatic pressure. The calculated wave height was assumed to be three times of the tsunami inundation depth as illustrated in Figure 2-6. The distribution of the tsunami wave pressures and forces were proposed as equation 2-15 and equation 2-16, respectively.

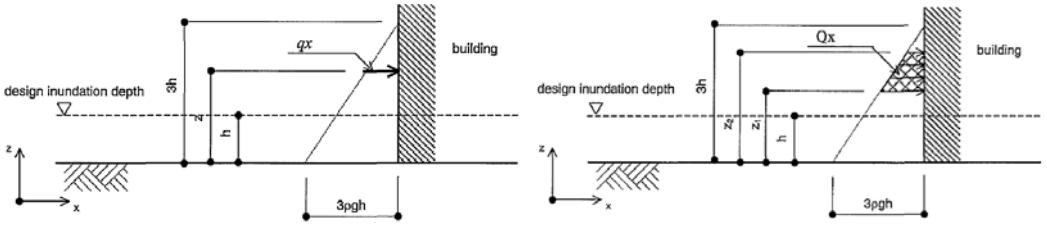

(a) Tsunami wave pressure distribution (b) Tsunami wave force distribution

Figure 2-6. Tsunami wave pressure and force act on a building (Okada et al., 2005)

In the case of buildings with the complex shapes, the tsunami wave load can be computed by using the wave pressure distribution as shown in Figure 2-7. For example, the building without open channel as Figure 2-7(a), the tsunami wave force can be computed by equation 2-17. Because of assuming the wave height equal to three times of the tsunami inundation depth, the tsunami wave force is nine times of the hydrostatic force. For the case of the inundation depth lower than open channel, the tsunami wave load dose not act on the building as shown in Figure 2-7(e).

$$qx = \rho g\left(3h - z\right) \tag{2-15}$$

$$Qx = \rho gB\int_{z_1}^{z_2}\left(3h - z\right)dz = \rho gB\left[\left(6hz_2 - z_2^2\right) - \left(6hz_1 - z_1^2\right)\right] \tag{2-16}$$

$$qx = \rho g\left(3h - z\right) \tag{2-17}$$

where

qx is tsunami wave pressure (kN/m^2),
Qx is tsunami wave force (kN),
F_x is horizontal force act on the building per unit width (kN/m),
ρ is mass per unit volume of water (t/m^3),
B is width of part of building,
g is gravitational acceleration (m/s^2),
h is design inundation depth (m),
z is height of the relevant portion from ground level ($0 \le z \le 3h$),
z_1 is minimum height of pressure-exposed surface ($0 \le z_1 \le z_2$),

z_2 is maximum height of pressure-exposed surface ($z_1 \le z_2 \le 3h$).

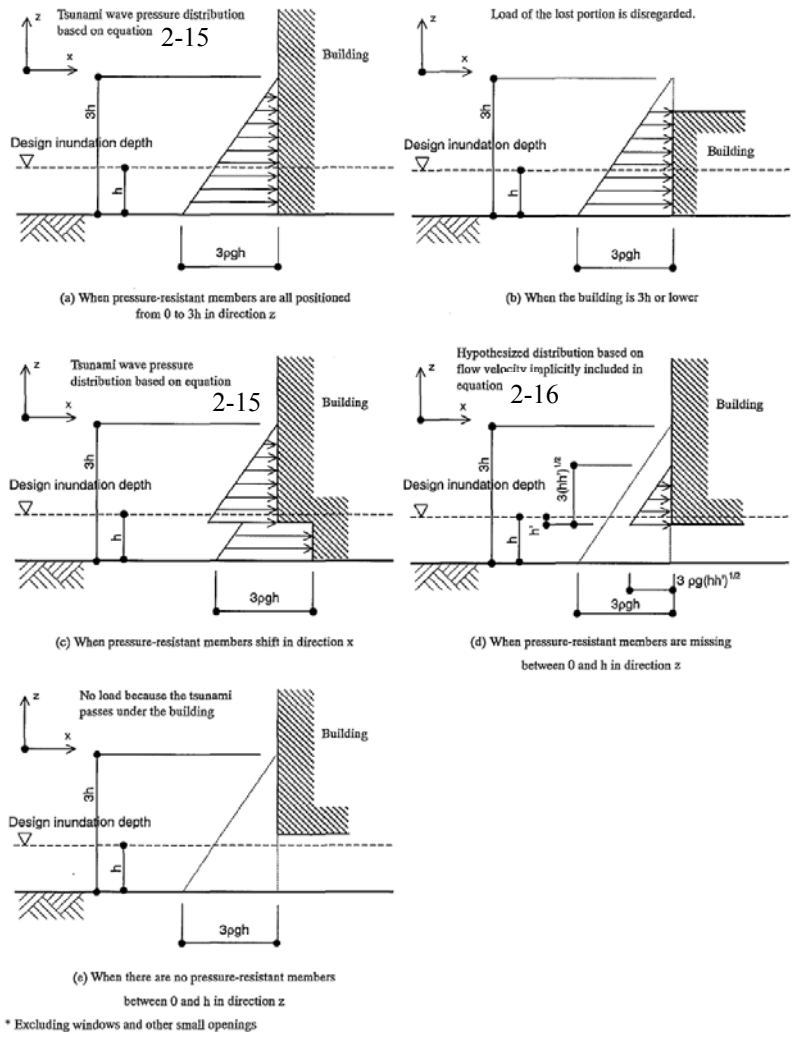

Figure 2-7. Tsunami wave pressure and force act on a building (Okada et al., 2005)

Yeh (2006, 2007) reviewed the existing design guidelines and proposed a rational methodology to determine the design tsunami forces on an onshore structure by using the tsunami inundation depth. In the proposed, a breaking wave force was not considered for an on shore building, and a hydrostatic force also was not considered because water quickly envelops all sides of a building. A hydrodynamic force was proposed in a term of the maximum moment flux, $\left(hu^2\right)_{\max}$ as shown in expressed 2-18, which was estimated when there is no building. The maximum moment flux may be obtained from the very fine grid size (less than 5 m) numerical model in the runup zone or from his proposed equations. Yeh (2006) proposed the analytical solutions to estimate the maximum moment flux of the nonlinear shallow-water wave theory for a uniform beach slope. The analytical solutions were developed to determine the wave height and the wave velocity on shore. The proposed equation

was obtained from fitting envelope of 9 initial conditions with four initial wave forms. The proposed equations are expressed in equation 2-19 and equation 2-20 those base on the distance and the ground elevation at the maximum runup height, respectively.

$$F_D = \frac{1}{2}\rho C_D B\left(hu^2\right)_{\max} \tag{2-18}$$

$$\frac{hu^2}{g\alpha^2 L^2} = 0.11\left(\frac{x}{L}\right)^2 + 0.015\left(\frac{x}{L}\right) \tag{2-19}$$

$$\frac{hu^2}{gR^2} = 0.125 + 0.11\left(\frac{z}{R}\right)^2 - 0.235\left(\frac{z}{R}\right) \tag{2-20}$$

where

F_D is hydrodynamic force,
C_D is drag coefficient = 2.0 for square or rectangular section,
= 1.2 for cylindrical section, from FEMA 55, 2000),
B is width of part of building,
h is flow depth when there is no building,
u is flow velocity when there is no building,
ρ is mass per unit volume of water,
g is gravitational acceleration,
α is uniform beach slope,
x is distance from the maximum runup height to the building location,
L is distance from the shoreline to the maximum runup height,
z is ground elevation of the building location,
R is ground elevation at the maximum runup height.

FEMA P646 (2008) proposed the structural design guidelines for a vertical evacuation from tsunami. In the guidelines, tsunami loads consist of a hydrostatic force, a buoyant force, a hydrodynamic force, an impulsive force, a debris impact force, a debris damming force, an uplift force and additional gravity loads. The hydrostatic force, F_h, was proposed that caused by the different pressure on both side of a structure, and can be neglected for a narrow structure. The hydrostatic force acting on a wall panel can be computed as equation 2-21, and a resultant force acts on 2/3 below the still water level. From the inundation map or the numerical simulation, in the case of fully submerged wall, the hydrostatic forces could be computed as equation 2-22.

$$F_h = \frac{1}{2}\rho g b h_{\max}^2 \tag{2-21}$$

$$F_h = \rho g b h_w\left(h_{\max} - \frac{h_w}{2}\right) \tag{2-22}$$

The hydrodynamic force, F_d, were proposed as equation 2-23. Due to the hydrodynamic force uniformly acting on a structure, the resultant force is applied on the centroid of the submerged level. The term of maximum moment flux, $\left(hu^2\right)_{\max}$, was computed from the numerical simulation with a very fine grid size (less than 10 m), or estimated from equation 2-24. However, the numerically simulated value should not be less than 80% of computed value by equation 2-24.

$$F_d = \frac{1}{2}\rho C_d B\left(hu^2\right)_{\max} \tag{2-23}$$

$$\left(hu^2\right)_{\max} = gR^2\left(0.125 - 0.235\frac{z}{R} + 0.11\left(\frac{z}{R}\right)^2\right) \tag{2-24}$$

where

ρ is fluid density (1200 kg/m^3),
C_d is drag coefficient = 2.0 (recommended),
B is breadth of the structure in the normal plane of flow direction,
$h_{\max}$ is the maximum inundation height = $1.3R^* - z_w = R - z_w$,
R is the maximum tsunami runup elevation,
R^* is the design tsunami runup elevation,
z_w is the base elevation of the wall,
g is gravitational acceleration,
b is breadth of the wall,
h_w is wall panel height.

The impulsive force, F_s caused by acting of the tsunami bore at the impinging edge on the structure in a very short duration. From past experiments and for conservative, the impulsive force was proposed as equal to 1.5 times the hydrodynamic force. As shown in Figure 2-8, the force combination of the hydrostatic force and the impulsive force for overall structure is the most severe when a surge acts on the latest row of building and other columns are acted by hydrodynamic forces. The hydrostatic force acts on the enclosing watertight walls.

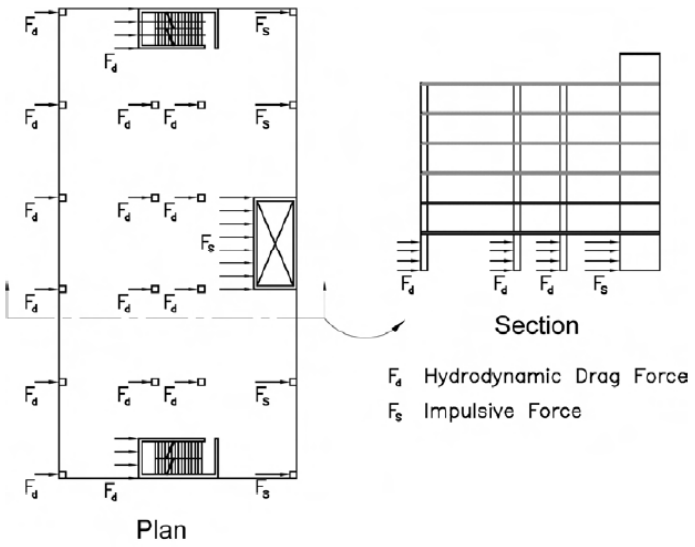

Figure 2-8. Impulsive and drag forces applied to an example building (FEMA P646, 2008)

Lukkunaprasit et al. (2009) verified the FEMA P646 design guideline by using some laboratory experiments. Their experiments were a 1:100-scale building models in a 40 m long, 1 m wide and 1 m depth wave flume. The hydrodynamic force and the surge force, which were recommended in FEMA P646, are expressed as equation 2-25 and equation 2-26, respectively. These two equations were compared with the measured experimental forces. The wave velocity was obtained from the experiments. The water depth was the thickness of the leading surge tongue. As shown in Figure 2-9, the measured forces agreed well with the calculated hydrodynamic forces with the drag coefficient of 2.0 better than the surge forces.

$$F_d = \frac{1}{2}\rho C_d B h u^2 \tag{2-25}$$

$$F_s = 4.5\rho g B h^2 \tag{2-26}$$

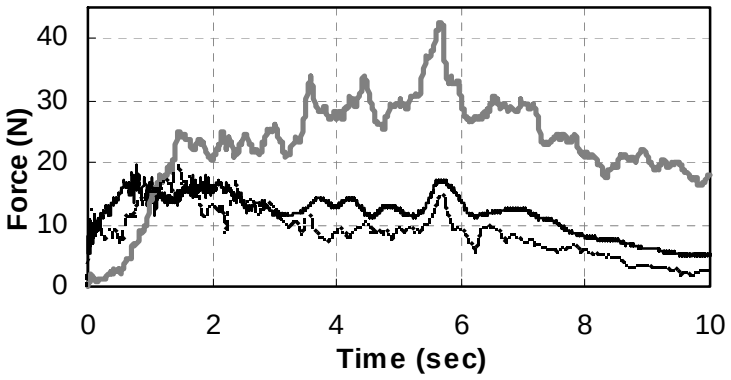

Figure 2-9. The comparison of the temporal variation of forces (solid line), measured (dotted line) and prediction by the hydrodynamic forces (dark grey line) (Lukkunaprasit et al., 2009)

2.2 Material Models

In this study, the building model primarily consists of an unconfined concrete model, a confined concrete model, a longitudinal reinforcement model, a shear model and a plane masonry infill model. The material models are reviewed as follows.

2.2.1 Unconfined concrete model

Kent and Park (1971) proposed the stress-strain relationship of unconfined concrete as shown in Figure 2-10. The stress-strain relationship consists of 2 parts which are the ascending branch ($\varepsilon_c \le \varepsilon_0$) and the falling branch ($\varepsilon_c > \varepsilon_0$). The ascending branch is represented by a second order parabola as equation 2-27. The strain at the peak stress is assumed to be 0.002. For the falling branch, the stress-strain relationship is assumed to be linearly as equation 2-28.

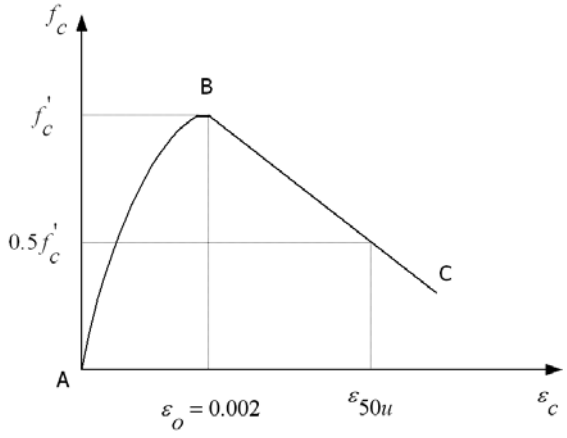

Figure 2-10. Stress-strain relationship of unconfined concrete (Kent and Park, 1971)

$$f_c = f_c'\left[\frac{2\varepsilon_c}{\varepsilon_0} - \left(\frac{\varepsilon_c}{\varepsilon_0}\right)^2\right] \tag{2-27}$$

$$f_c = f_c'\left[1 - Z\left(\varepsilon_c - \varepsilon_0\right)\right] \tag{2-28}$$

$$Z = 0.5/\left(\varepsilon_{50u} - 0.002\right) \tag{2-29}$$

$$\frac{3 + 0.002 f_c'}{f_c' - 1000} \tag{2-30}$$

where

ε_{50u} is strain at a haft of peak stress (from experimental results),
f_c is longitudinal compressive concrete stress,
ε_c is longitudinal compressive concrete strain,
f_c' is maximum stress of cylinder,
ε_0 is strain at peak stress, assumed to be 0.002.

2.2.2 Confined concrete model

Kent and Park (1971) proposed the stress-strain relationship of confined concrete under uniaxial loading as shown in Figure 2-10. The stress-strain relationship consists of 3 parts which are the ascending branch ($\varepsilon_c \le \varepsilon_0$), the falling branch ($\varepsilon_0 < \varepsilon_c \le \varepsilon_{20c}$) and the sustain branch ($\varepsilon_c > \varepsilon_{20c}$). The ascending branch and the falling branch are represented by a second order parabola and a linear similar, respectively. The falling slope is represented by the parameter Z . The falling branch slope of confined was proposed as equation 2-31. The sustaining branch was assumed to be a constant equal to 0.2 of the maximum stress of cylinder as equation 2-32.

$$Z = 0.5/\left(\varepsilon_{50h} + \varepsilon_{50u} - 0.002\right) \tag{2-31}$$

where

ε_{50h} is additional strain due to confinement (from experimental result)

$$= \frac{3}{4}\rho''\sqrt{\frac{b''}{s}}$$

ρ'' is volumetric ratio (ratio of the volume of transverse reinforcement to the volume of confined concrete core)

$$= \frac{2\left(b'' + d''\right)A_s''}{b''d''s}$$

$$f_c = 0.2\,f_c' \tag{2-32}$$

Mander et al. (1988) proposed the stress-strain model for a confined concrete which considered configuration of the transverse and longitudinal reinforcement for circular and rectangular sections. The confined concrete stress-strain model with monotonic loading at slow strain rates is illustrated in Figure 2-11 and expressed as equation 2-33.

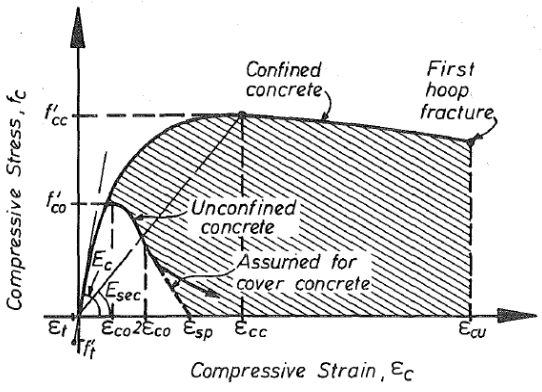

Figure 2-11. Stress-strain model proposed for monotonic loading of confined and unconfined concrete (Mander et al., 1988)

$$f_c = \frac{f'_{cc} x r}{r - 1 + x^r} \tag{2-33}$$

where

$$f'_{cc} = f'_{co}\left(2.254\sqrt{1+\frac{7.94 f'_l}{f'_{co}}} - 2\frac{f'_l}{f'_{co}} - 1.254\right) \tag{2-34}$$

$$x = \frac{\varepsilon_c}{\varepsilon_{cc}} \tag{2-35}$$

$$r = \frac{E_c}{E_c - E_{\text{sec}}} \tag{2-36}$$

$$\varepsilon_{cc} = \varepsilon_{co}\left[1 + 5\left(\frac{f'_{cc}}{f'_{co}} - 1\right)\right] \tag{2-37}$$

$$\varepsilon_{co} = 0.002 \tag{2-38}$$

$$E_{\text{sec}} = \frac{f'_{cc}}{\varepsilon_{cc}} \tag{2-39}$$

$$f'_l = f_l \cdot k_e \tag{2-40}$$

f_c is longitudinal compressive concrete stress,

f'_{cc} is confined concrete compressive stress,

f'_{co} is unconfined concrete compressive stress,

ε_c is longitudinal compressive concrete strain,

ε_{cc} is unconfined concrete compressive strain,

ε_{co} is unconfined concrete compressive strain, generally $\varepsilon_{co} = 0.002$,

E_c is tangent modulus of elasticity of the concrete, $= 5{,}000\sqrt{f'_{co}}$,

$E_{sec} = f'_{cc} / \varepsilon_{cc}$,

f'_l is effective lateral confining pressure, $f'_l = f_l k_e$,

f_l is lateral confining pressure,

k_e is confinement effectiveness coefficient, $k_e = A_e / A_{cc}$,

A_e is area of an effective confined concrete core at midway between the levels of transverse reinforcement,

A_{cc} is area of the confined concrete, $A_{cc} = A_c\left(1 - \rho_{cc}\right)$,

A_c is area of core section,

ρ_{cc} is ratio of area of longitudinal reinforcement to area of section.

The area of the confined concrete and the area of the core section are areas at the center lines of the transverse reinforcement. For the circular section, effective confined concrete core is described as Figure 2-12(a). The area of core section is

$A_c = \frac{\pi}{4} d_s^2$. The effective confined concrete core area of a circular section was proposed as equation 2-41, and then the confinement effectiveness coefficient of a circular hoop was proposed as equation 2-42. In the same manner, the confinement effectiveness coefficient of a spiral confinement was proposed as equation 2-43. The equilibrium of forces by considering the half body confined for either a spiral or a circular hoop was proposed as equation 2-44 and equation 2-45, respectively. Thus the effective lateral confining pressure for either a spiral confinement or a circular hoop was proposed as equation 2-46.

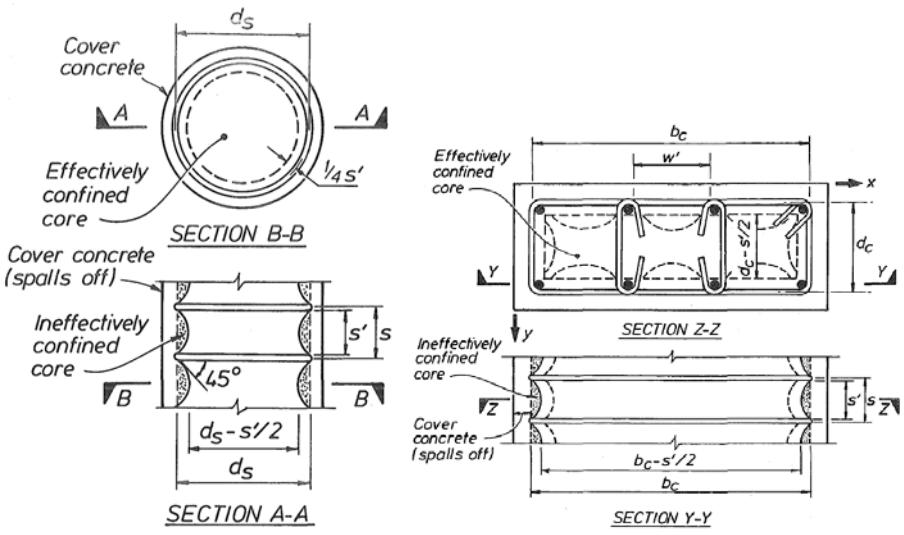

(a) Circular hoop reinforcement (b) Rectangular hoop reinforcement

Figure 2-12. Effectively confined of core concrete (Mander et al., 1988)

$$A_e = \frac{\pi}{4}\left(d_s - \frac{s'}{2}\right)^2 = \frac{\pi}{4} d_s^2 \left(1 - \frac{s'}{2d_s}\right)^2 \tag{2-41}$$

$$k_e = \frac{\left(1 - \frac{s'}{2d_s}\right)^2}{\left(1 - \rho_{cc}\right)} \tag{2-42}$$

$$k_e = \frac{1 - \frac{s'}{2d_s}}{\left(1 - \rho_{cc}\right)} \tag{2-43}$$

$$2 f_{yh} A_{sp} = f_l s d_s \tag{2-44}$$

$$f_l = \frac{1}{2} \rho_s f_{yh} \tag{2-45}$$

$$f_l' = \frac{1}{2} k_e \rho_s f_{yh} \tag{2-46}$$

where

s' is clear vertical spacing of transverse reinforcement,

d_s is diameter of transverse reinforcement between the center bar,

f_{yh} is yield strength of the transverse reinforcement,

A_{sp} is area of transverse reinforcement,

s is center to center spacing of spiral or circular hoop,

ρ_s is ratio of the volume of transverse reinforcement to the volume of confined concrete core, $\rho_s = \dfrac{A_{sp}\pi d_s}{\pi d_s^2 s/4} = \dfrac{4A_{sp}}{d_s s}$.

For a rectangular section, the effective confined concrete core is shown as Figure 2-12(b), the area of core section is $A_c = b_c d_c$. The ineffective confined area in the second-degree parabola with an initial tangent slope of 45° is $\sum_{i=1}^{n}\left(w_i'\right)^2/6$, where w_i' is the i[th] clear distance between longitudinal reinforcement. Then the effective confined concrete core area of a regular hoop can be expressed as equation 2-47. The confinement effectiveness coefficient of a rectangular hoop was proposed as equation 2-48.

$$A_e = \left(b_c d_c - \sum_{i=1}^{n}\frac{\left(w_i'\right)^2}{6}\right)\left(1-\frac{s'}{2b_c}\right)\left(1-\frac{s'}{2d_c}\right) \tag{2-47}$$

$$k_e = \frac{\left(1-\sum_{i=1}^{n}\dfrac{\left(w_i'\right)^2}{6b_c d_c}\right)\left(1-\dfrac{s'}{2b_s}\right)\left(1-\dfrac{s'}{2d_c}\right)}{\left(1-\rho_{cc}\right)} \tag{2-48}$$

The equilibrium of forces by considering the half body confined for a rectangular hoop was expressed as equation 2-49 and equation 2-50 in x-direction and y-direction, respectively. Thus the effective lateral confining pressure for a rectangular hoop can be expressed as equation 2-51.

$$f_{lx} = \frac{A_{sx}}{sd_c} f_{yh} = \rho_x f_{yh} \tag{2-49}$$

$$f_{ly} = \frac{A_{sy}}{sb_c} f_{yh} = \rho_y f_{yh} \tag{2-50}$$

$$f_{lx}' = k_e \rho_x f_{yh} \text{ and } f_{ly}' = k_e \rho_y f_{yh} \tag{2-51}$$

where

b_c is core dimensions to centerlines of rectangular hoop in x directions,

d_c is core dimensions to centerlines of rectangular hoop in y directions,
ρ_x is transverse confining steel in x directions, $\rho_x = A_{sx} / sd_c$,
ρ_y is transverse confining steel in y directions, $\rho_y = A_{sy} / sb_c$,
A_{sx} is total area of transverse steel along x directions,
A_{sy} is total area of transverse steel along y directions.

Hoshikuma et al. (1997) developed the stress-strain model of confined concrete based on experimental results for the low volumetric ratio range (0.3%-0.5%). 31 specimens were tested under uniaxial loading by varying size of specimen, sectional shape, volumetric ratio, hoop spacing, hook configuration and cross tie. The model can satisfy 4 boundary conditions; the initial condition $f_c = 0$ at $\varepsilon_c = 0$, the initial stiffness condition $df_c / d\varepsilon_c = E_c$ at $\varepsilon_c = 0$, the peak condition $f_c = f_{cc}$ at $\varepsilon_c = \varepsilon_{cc}$ and the peak stiffness condition $df_c / d\varepsilon_c = 0$ at $\varepsilon_c = \varepsilon_{cc}$. The proposed model better agreed well with the experimental results. The confined concrete stress-strain model was proposed consisting of two parts which are the ascending branch, the falling branch as shown in Figure 2-13. For the ascending branch, the stress-strain model can be written as equation 2-52. The falling branch was proposed by a straight line. The ultimate strain was defined as the strain corresponding to 50% of the peak stress. The formula can be expressed as equation 2-53.

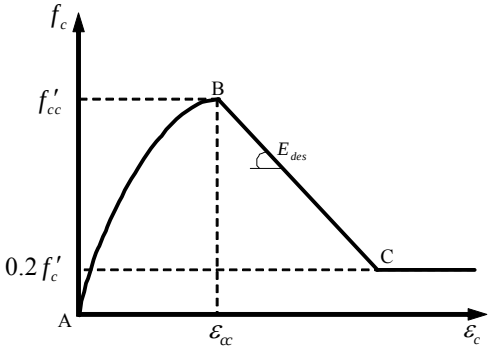

Figure 2-13. Stress-strain relationship of confined concrete (Hoshikuma et al., 1997)

$$f_c = E_c \varepsilon_c \left[1 - \frac{1}{n} \left(\frac{\varepsilon_c}{\varepsilon_{cc}} \right)^{n-1} \right] \tag{2-52}$$

$$f_c = f_{cc} + E_{des} \left(\varepsilon_c - \varepsilon_{cc} \right) \tag{2-53}$$

where

$$n = \frac{E_c \varepsilon_{cc}}{E_c \varepsilon_{cc} - f_{cc}} \tag{2-54}$$

$$\varepsilon_{cu} = \varepsilon_{cc} + \frac{f_{cc}}{2E_{des}} \tag{2-55}$$

$$\frac{f_{cc}}{f_{co}} = 1 + 3.8\alpha \frac{\rho_s f_{yh}}{f_{co}} \tag{2-56}$$

$$\varepsilon_{cc} = 0.002 + 0.033\beta \frac{\rho_s f_{yh}}{f_{co}} \tag{2-57}$$

$$E_{des} = 11.2 \frac{f_{co}^2}{\rho_s f_{yh}} \tag{2-58}$$

f_c is longitudinal compressive concrete stress,

ε_c is longitudinal compressive concrete strain,

f_{cc} is peak longitudinal compressive concrete stress,

ε_{cc} is longitudinal compressive concrete strain at peak stress,

f_{co} is unconfined concrete compressive stress,

ε_u is ultimate strain,

E_c is initial stiffness,

E_{des} is deterioration rate,

ρ_s is volumetric ratio (ratio of the volume of transverse reinforcement to the volume of confined concrete core),

f_{yh} is yield strength of the transverse reinforcement,

α and β are modification factors depending on confined sectional shape

for circular section $\alpha = 1.0$ and $\beta = 1.0$

for square section $\alpha = 0.2$ and $\beta = 0.4$.

2.2.3 Longitudinal reinforcement model

Gomes and Appleton (1997) proposed the nonlinear stress-strain relationship of longitudinal reinforcement model including buckling under cyclic loading. The proposed relationship was modified from the model proposed by Menegotto and Pinto (1973) which is illustrated in Figure 2-14 and consisted of 4 parts; elastic, yielding, hardening and Baushinger effect. The model proposed by Menegotto-Pinto can be expressed as equation 2-59. The buckling effect was considered by the equilibrium of buckled steel after the rupture of covering concrete occurs. The proposed model agreed well with the experimental results.

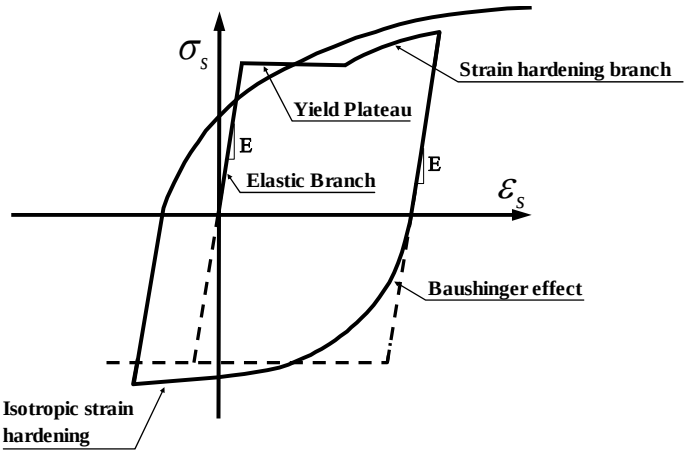

Figure 2-14. Stress-strain relationship of a longitudinal steel (Gomes and Appleton, 1997)

$$\sigma_s^* = \beta\varepsilon_s^* + \frac{(1-\beta)\varepsilon_s^*}{\left[1+\left(\varepsilon_s^*\right)^R\right]^{1/R}} \tag{2-59}$$

where

$$\sigma_s^* = \frac{\sigma_s - \sigma_{sa}}{\sigma_{s1} - \sigma_{sa}},\ \varepsilon_s^* = \frac{\varepsilon_s - \varepsilon_{sa}}{\varepsilon_{s1} - \varepsilon_{sa}} \tag{2-60}$$

$\sigma_{sa}, \varepsilon_{sa}$ are stress and strain at the yield point, respectively

$\sigma_{s1}, \varepsilon_{s1}$ are stress and strain at the intersection point of the envelop line to the elastic path, respectively

β is ratio of the hardening stiffness to the tangent modulus of elasticity $= E_{s1} / E_s$

R is expressing constant Baushinger effect = $R_0 - \dfrac{a_1\xi}{a_2 + \xi}$

ξ is plastic strain of the last loop

R_0, a_1, a_2 are constants of material = 20, 19, 0.3, respectively (suggestion)

2.2.4 Shear model

Sezen (2002) proposed the shear strength equation of light and inadequately detailed columns based on the theoretical formulations and cited experimental results under cyclic loadings. The shear strength equation was considered the effect of cross-sectional dimensions, concrete compressive strength, column aspect ratio, axial load and displacement ductility demand. From 51 cited testing columns, the shear strength increases with the increasing of axial load, longitudinal reinforcement ratio and amounts of transverse reinforcement, but decreases with the increasing of aspect ratio. The proposed shear behavior of the column under monotonic displacement consists of 4 points; cracking point, yielding point, maximum load point and gravity load

collapse point as shown in Figure 2-15. The shear strength equation was proposed as equation 2-61. The strength degradation of the transverse reinforcement was also considered and equal to the strength degradation of concrete. At the cracking point with the double-curvature deformation, the shear strength (V_{cr}) can be calculated from the cracking moment as equation 2-62. The shear strength at the yielding point (V_y) can be computed from the yielding moment as equation 2-63. The displacements at the cracking (δ_{cr}), yielding (δ_y) and maximum load (δ_n) are proposed as from equation 2-64 to equation 2-66, respectively.

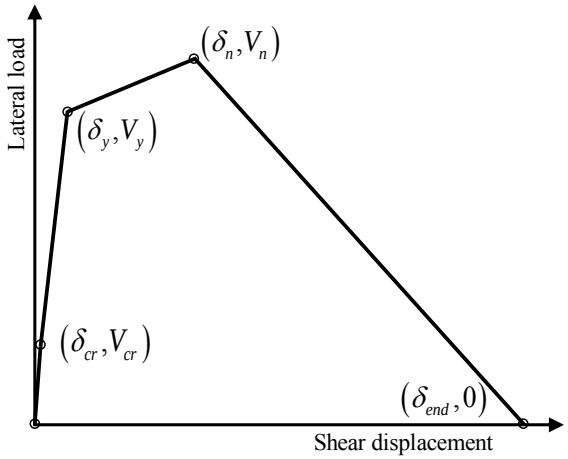

Figure 2-15. Lateral load and shear displacement relationship (Sezen, 2002)

$$V_n = V_s + V_c = k\frac{A_v f_y d}{s} + k\left(\frac{0.5\sqrt{f_c'}}{a/d}\sqrt{1+\frac{P}{0.5\sqrt{f_c'}A_g}}\right)0.8A_g \tag{2-61}$$

$$V_{cr} = \frac{2M_{cr}}{L} \tag{2-62}$$

$$V_y = \frac{2M_y}{L} \tag{2-63}$$

$$\delta_{cr} = 3\frac{V_{cr}L}{E_c A_g} \tag{2-64}$$

$$\delta_y = \left(\frac{3}{0.2+0.4P_r}\right)\frac{V_y L}{E_c A_g} \tag{2-65}$$

$$\delta_n = \frac{V_s L}{d\,b}\left[\frac{1}{\rho_w E_s} + \frac{4}{E_c}\right] \tag{2-66}$$

where

V_n is nominal shear strength

V_s is contribution shear strength from ties

V_c is contribution shear strength from concrete

k is factor relating the concrete or transverse reinforcement capacity to displacement ductility which is equal to 1.0 for displacement ductility less than 2, equal to 0.7 for displacement ductility exceeding 6 and linearly varies for intermediate displacement ductility

A_v is transverse reinforcement area within a spacing, s, in the loading direction

f_y is yield strength of transverse reinforcement

d is depth of centroid of tension reinforcement

s is spacing of transverse reinforcement

f_c' is compressive strength of concrete

a is shear span

P is axial load

A_g is gross area of section

M_{cr} is cracking moment = $\left(7.5\sqrt{f_c'}I\right)/c$

M_y is yielding moment

I is uncrack cross-sectional moment of inertia

c is neutral axis depth

L is column length

E_c is modulus of elasticity of concrete

E_s is modulus of elasticity of transverse steel

P_r is axial load ratio = P/P_0

b is width of column section

ρ_w is transverse reinforcement ratio

2.2.5 In-plane masonry infill wall model

For an in-plane masonry infill wall, some experimental researches are reviewed in this study.

Mehrabi et al. (1996) investigated twelve 1/2-scale, single-story, and single bay frame with masonry infills specimens. Specimens were varied in strengths of the boundary frame, strengths of infill, aspect ratios, distributions of vertical loads and lateral-load histories. Five primary failure modes were considered for the boundary frame, the flexural failure and midheight crack due to the shear failure, for the infill panel, the diagonal crack, horizontal slip and corner crushing. The failure modes of experiments depended on the relative strength of the boundary frame and infill. For a weak frame with weak infills, the dominant failure mode was the flexure of columns and bed-joint sliding of the infill. For a strong frame with weak infill, the bed-joint sliding failure dominated. If the strength of the frame is less than the strength of the infill, damage will occur in the boundary frame with shear failure mode. The crushing

failure occurs in an infill for the case of the strong frame with the strong infill. From the results, the lateral resistance of infilled frame increased with the strength of infill. The lateral resistance increased 1.5 times in the case of the weak infill and in the case of the strong infill increased 2.3 times. However, in the case of the strong infill, the resistance load after its peak degraded faster than the resistance load after its peak of the weak infill. The stiffnesses of infilled frames with weak infill and strong infill were higher than that of the bare frame of 15 times and 50 times, respectively. Variations of aspect ratios had little effect on the lateral resistance load and the stiffness.

Kakaletsis and Karayannis (2008) investigated seven 1/3-scale single-bay single-story masonry infill walls by varying the opening shapes (w/o opening, door and window) and the infill compressive strengths under the cyclic loading. They also predicted the lateral resistance of single-bay and single-story masonry infill walls by using the plastic analysis method and crack patterns. From experimental results, the failure mechanisms of masonry infill walls were a internal strut crushing, a shear sliding at joints, a shear sliding crack and a corner rocking crushing. For the masonry infill walls with an opening, the energy dissipation was reduced at the high lateral displacement. And the masonry infill walls with the higher compressive strength were better than the masonry infill walls with the lower compressive strength in term of the lateral load resistance, stiffness, ductility and energy dissipation capacity.

FEMA 306 (1998) proposed equations to evaluate the strength capacity of the masonry infill by considering four failure modes; sliding shear failure, compression failure, diagonal tension failure and general shear failure. The sliding shear failure occurs when the mortar is weaker than masonry unit. From the Mohr-Coulomb failure criteria, the strength of the shear failure can be expressed as equation 2-67.

$$V_{sliding} = \left(\sigma_y \tan\phi\right) L_{\text{inf}} t_{\text{inf}} = \mu N \tag{2-67}$$

The axial load of the infill is expressed in equation 2-68. And by assuming small displacement, the vertical strain of the panel can be expressed in equation 2-69. Then equation 2-68 and equation 2-69 are substituted into equation 2-67 as equation 2-70.

$$N = \varepsilon L_{\text{inf}} t_{\text{inf}} E_m \tag{2-68}$$

$$\varepsilon = \frac{\delta}{h} = \theta \frac{\Delta}{h} = \theta^2 \tag{2-69}$$

$$V_{sliding} = \mu L_{\inf} t_{\inf} E_m \theta^2 \tag{2-70}$$

The compression failure usually occurs when the masonry unit is weaker than the mortar, and the bound frame is strong. Shear strength of the diagonal strut can be express as equation 2-71.

$$V_c = a t_{\inf} f'_{m90} \cos\theta \tag{2-71}$$

The diagonal tension failure occurs when the tensile strain exceeds the cracking strain of the infill material. The cracks develop in the center of the infill and along the diagonal. The shear strength is shown as equation 2-72. The general shear failure was proposed as equation 2-73.

$$V_{cr} = \frac{2\sqrt{2} t_{\inf} \sigma_{cr}}{\left(\frac{L_{\inf}}{h_{\inf}} + \frac{h_{\inf}}{L_{\inf}} \right)} \tag{2-72}$$

$$V_{mi} = A_{sh} 2\sqrt{f'_{me}} \tag{2-73}$$

The deflection of masonry infill wall was proposed by FEMA 356 (2000) in term of the drift ratio according to the geometry ratio of masonry infill wall ($L_{\inf} / h_{\inf}$) and the shear strength ratio of bare frame and infill wall (V_{fre} / V_{ine}) as listed in Table 2-2.

Table 2-2. Simplified force-deflection relationships for masonry infill panels (FEMA 306, 1998)

$\beta = V_{fre} / V_{ine}$	$L_{\inf} / h_{\inf}$	Drift (%)
$\beta < 0.7$	0.5	0.5
	1.0	0.4
	2.0	0.3
$0.7 \le \beta < 1.3$	0.5	1.0
	1.0	0.8
	2.0	0.6
$\beta \ge 1.3$	1.5	1.5
	1.0	1.2
	2.0	0.9

where

ϕ is the angle of sliding friction of the masonry along a bed joint

$L_{\inf}$ is length of infill panel

$t_{\inf}$ is thickness of infill panel

μ is coefficient of sliding friction along the bed joint

N is vertical load in the panel

δ is vertical deformation of the upper beam

h is interstory height (center to center of beams)
Δ is interstory drift
θ is interstory drift angle
f'_{m90} is strength of masonry in the horizontal direction $\approx 0.5 f'_{me}$
f'_{me} is compression strength of a masonry prism
σ_{cr} is the cracking strength $\approx v_{me} = 20\sqrt{f'_{me}}$
A_{vh} is horizontal shear area of infill $= L_{\inf} t_{\inf}$
a is equivalent strut width = $0.175(\lambda h)^{-0.4} d_m$
d_m is diagonal length of infill panel (cm)

$$\lambda = \left[\frac{E_m t \sin 2\theta}{4 E_c I_g h_m} \right]^{1/4}$$

E_m is Young's modulus of infill material = $750 f'_p$ (ksc)
E_c is Young's modulus of frame material = 240000 (ksc)
I_g is moment of inertial of column, (cm^4)
h_m is height of infill panel, (cm)
$\theta = \tan^{-1}(h_{\inf} / L_{\inf})$

Mostafaei and Kabeyasawa (2004) analyzed the Bam telephone center building by using 3-dimensional nonlinear time history analysis including the effect of infill masonry walls under the 2003 Bam earthquake. The model was analyzed by the Opensees program. The model was performed for 3 different categories; bare frame without considering of stiffness and strength of infill wall, bare frame and masonry infill walls and bare frame with considering only masonry infill mass. The results of models were compared with the damage and residual cracks of the building. For masonry infill walls, the compressive strength, f'_p, is computed by equation 2-74.

$$f'_p = \frac{f'_{cb}\left(f'_{tb} + \alpha_c f'_j\right)}{U_u\left(f'_{tb} + \alpha_c f'_{cb}\right)} \tag{2-74}$$

where

f'_{cb} is compressive strength of the brick
f'_{tb} is tension strength of the brick
f'_j is mortar compressive strength
U_u is the stress non-uniformity coefficient = 1.5
$\alpha_c = j / 4.1 h_b$
j is mortar joint thickness
h_b is height of the solid brick

Shear strength of infill wall was considered by 2 failure modes; sliding shear failure and compressive failure of diagonal strut. Figure 2-16 shows the equivalent diagonal compressive action parameters. The shear strength of the sliding shear failure V_f is expressed as equation 2-75. From Figure 2-16, V_f and N can be written in the term of diagonal compression force, R_c, then substituting into equation 2-75. For the compressive failure of diagonal strut, the shear strength was proposed as equation 2-77.

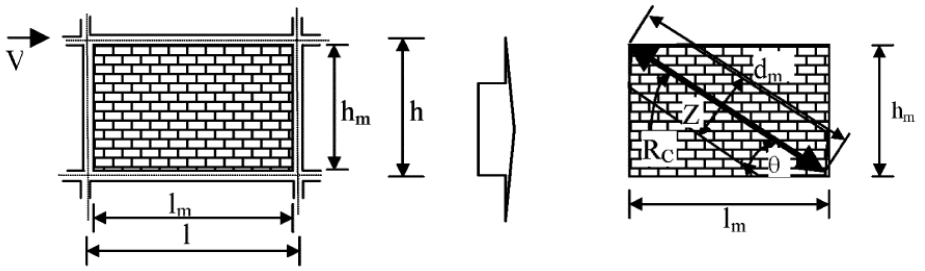

Figure 2-16. Infill masonry walls and the equivalent diagonal compressive action parameters (Mostafaei and Kabeyasawa, 2004)

$$V_f = \tau_0 t l_m + \mu N \tag{2-75}$$

$$V_f = \frac{\tau_0 t l_m}{\left(1 - \mu \tan\theta\right)} \tag{2-76}$$

$$V_c = Z t f_p \cos\theta \tag{2-77}$$

Where

τ_0 is cohesive capacity of the mortar beds = $0.04 f_b'$ (ksc)

t is infill wall thickness (cm)

l_m is length of infill panel, (cm)

μ is sliding friction coefficient along the bed joint

= $0.654 + 0.000515 f_j'$ (from experimental results)

N is vertical load in infill walls

Z is equivalent strut width = $0.175\left(\lambda h\right)^{-0.4} d_m$

d_m is diagonal length of infill panel (cm)

$$\lambda = \left[\frac{E_m t \sin 2\theta}{4 E_c I_g h_m}\right]^{1/4}$$

E_m is Young's modulus of infill material = $750 f_p'$ (ksc)

E_c is Young's modulus of frame material = 240000 (ksc)

I_g is moment of inertial of column, (cm^4)

h_m is height of infill panel, (cm)

$\theta = \tan^{-1}\left(h_m / l_m\right)$

To model the masonry infill walls, the analytical model and the strength envelope are shown in Figure 2-17. The envelope can be conducted by 6 parameters which are the shear strength at the yielding point, V_y, at the maximum point, V_m which is the minimum shear strength of the sliding shear failure and compressive failure of diagonal strut, for sustain region, V_p, their corresponding displacements, U_y, U_m and U_p, respectively and the initial stiffness, K_0. All enveloped parameter can be computed by the following equations.

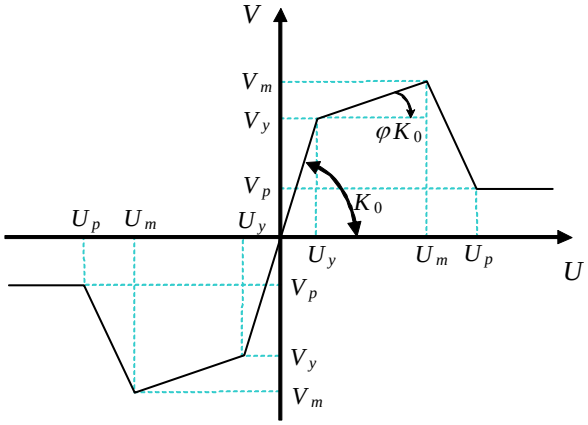

Figure 2-17. Strength envelope for conventional masonry infill walls and the analytical model (Mostafaei and Kabeyasawa, 2004)

$$U_m = \frac{\varepsilon'_m d_m}{\cos\theta},\ K_0 = 2\left(V_m / U_m\right) \tag{2-78}$$

$$V_y = \frac{V_m - \alpha_f K_0 U_m}{1-\alpha},\ U_y = V_y / K_0 \tag{2-79}$$

$$V_p = 0.3V_m,\ U_y = 3.5\left(0.01h_m - U_m\right) \tag{2-80}$$

The parameter α_f was assumed to be equal to 0.2. For the stress-strain relationship of masonry infill walls, the parameters were computed by the following equations.

$$\sigma_i = V_i / \left(A_d \cos\alpha\right),\ \varepsilon_i = U_i \cos\alpha / L_d \tag{2-81}$$

$$A_d = Zt,\ \alpha = h/l,\ L_d = \sqrt{l^2 + h^2} \tag{2-82}$$

The model was considered as a zero length horizontal spring by using nonlinear pushover analysis that is convenient to model a wall with opening channel and a multi materials wall. The results were similar to the results of the model by using the zero length diagonal spring as illustrated in Figure 2-18. The equivalent spring model for multi-spring panels was also proposed. The masonry infill wall with

opening channel was divided to sub-walls and determined the shear strength of each sub-walls individually as shown in Figure 2-19. The parameters of equivalent spring model were obtained by subtracting the lateral force-displacement response of the bare frame from the lateral force-displacement response of multi-spring infilled frame as described in Figure 2-20(a). Figure 2-20(b) shows the response of equivalent single-spring model.

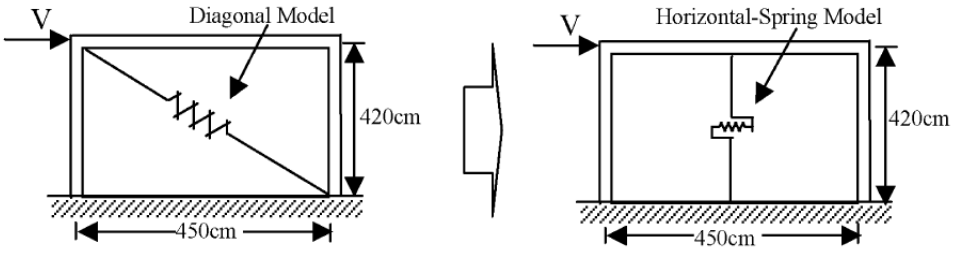

(a) Diagonal spring (b) Horizontal spring

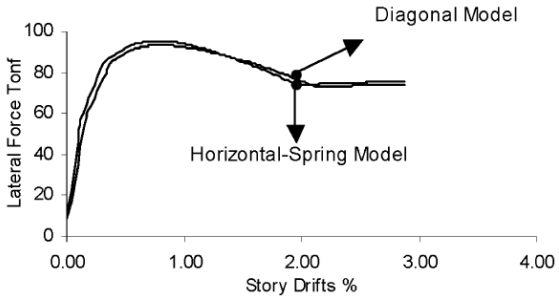

(c) Result of pushover analyses

Figure 2-18. Comparison of diagonal spring and horizontal spring
(Mostafaei and Kabeyasawa, 2004)

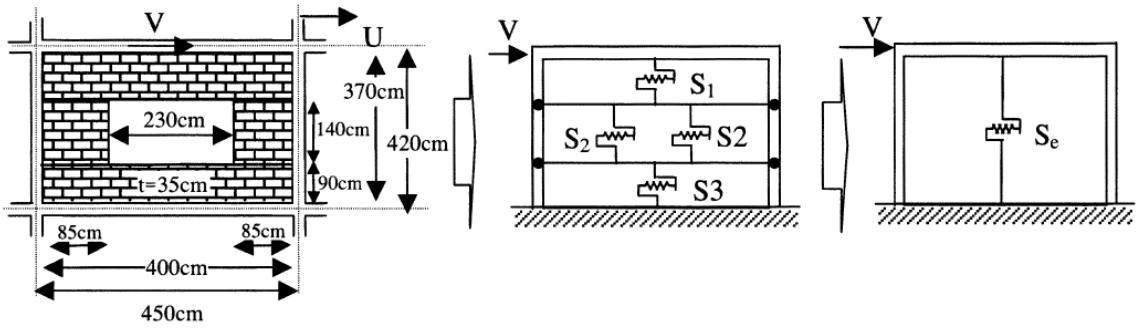

Figure 2-19. An infilled frame with window opening and its equivalent with a single-spring
(Mostafaei and Kabeyasawa, 2004)

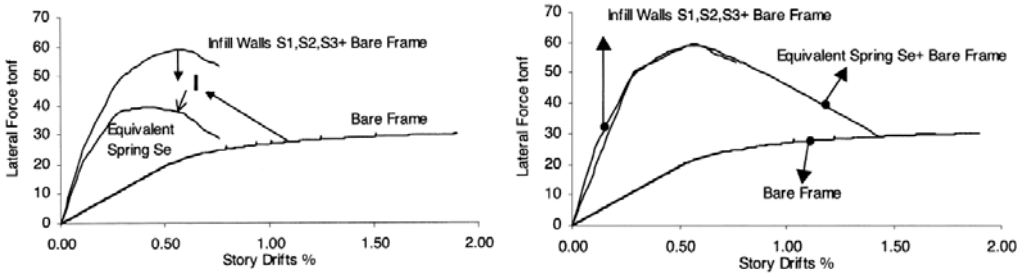

(a) Processing by subtracting (b) Response of equivalent spring model

Figure 2-20. The processing and response of equivalent spring model
(Mostafaei and Kabeyasawa, 2004)

2.3 Development of Fragility Curves

In earthquake engineering, there are many proposed fragility curves developed by both empirical method and analytical methods.

2.3.1 Fragility curves for earthquakes

Yamazaki et al. (1999) proposed empirical fragility curves for expressway structures in Japan based on observed data from the 1995 Hyogoken-Nanbu Earthquake. The spatial distributions of earthquake ground motion which are PGA, PGV and JMA (Japan Meteorological Agency) intensity were estimated by the Kriging technique and fitted well with observed values. Four damage levels ranging from minor or no damage to collapse were considered. The fragility curves were developed by using the least square method and assuming as a log-normal distribution as functions of PGA, PGV and JMA intensity.

Karim and Yamazaki (2001) developed analytical fragility curves of reinforced-concrete bridge piers based on numerical simulation. The structural parameters and variation of input ground motions were considered. The damage indices of the bridge piers were obtained from the static pushover analysis and non-linear dynamic response analysis of an equivalent single degree of freedom model. The damage of model was estimated by the damage index, DI, proposed by Park and Ang (1985) as equation 2-83. After that, the damage index was converted to the damage rank proposed by Ghobarah et al. (1997). The damage rank was classified into 5 ranks as listed in Table 2-3. Finally, fragility curves were developed as functions of PGV and PGA by using the damage indices and ground motion parameters by using least-square method and assuming a lognormal distribution. The proposed fragility curves agreed well with fragility curves from the past earthquake experience.

Table 2-3. Relationship of between the damage index and the damage rank (Ghobarah et al., 1997)

Damage Index (DI)	Damage Rank	Definition
$0.00 < DI \leq 0.14$	D	No Damage
$0.14 < DI \leq 0.40$	C	Slight Damage
$0.40 < DI \leq 0.60$	B	Moderate Damage
$0.60 < DI < 1.00$	A	Extensive Damage
$1.00 \leq DI$	As	Complete Damage

$$DI = \frac{\mu_d + \beta\mu_h}{\mu_u} \tag{2-83}$$

where

μ_d is displacement ductility = δ / δ_y,

β is cyclic loading factor which was assumed equal to 0.15,

μ_h is cumulative energy ductility = E_h / E_e,

μ_u is ultimate ductility = $\delta_{\max} / \delta_y$,

E_h is cumulative hysteretic energy,

E_e is elastic energy.

Lee et al. (2001) constructed the seismic fragility curves of the building damage on Chi-Chi earthquake. 44,880 damaged buildings were considered. The fragility curves were constructed for 4 types of building and 3 construction periods as a function of peak ground acceleration by assuming as a lognormal distribution. For damage levels, totally collapsed and partially collapsed were considered.

Shinozuka et al. (2001) developed empirical fragility curves of bridges damage by the 1994 Northridge and the 1995 Hyogo-ken Nanbu (Kobe) earthquakes. The fragility curves were established for four damage levels by using the maximum likelihood procedure and assuming as a lognormal distribution. Two difference methods were used to develop fragility curves. In the first method, each fragility curve is developed independently and in another method, the fragility curves were developed simultaneously using common value of the log-standard derivation to avoid the intersection of them. They also developed analytical fragility curves for the Caltrans' bridges and Hanshin Expressway Public Corporation's bridges. The analytical fragility curves were considered 2 damage levels; minor damage and major damage. The minor damage was defined as the ductility demand exceeding one, and the major damage was defined as the ductility demand exceeding two. Finally, the testing goodness of fit of the fragility curves and the estimating the confidence intervals of the fragility parameters were introduced.

Tantala and Deodatis (2002) developed seismic fragility curves for tall buildings as a function of PGA. Uncertainties of the ground motion characteristics and structural materials were considered. Ground motion characteristic uncertainties were seismic duration, amplitudes and phases. Uncertainties were concrete compressive strengths and steel tensile strengths which were assumed to have a normal distribution. For establishing fragility curves, a structural model was a two-dimension model which consisted of elastic beam elements, elastic column elements and non-linear plastic rotational springs at each end. The fragility curves were developed by using maximum likelihood method and assumed as a log-normal distribution. Two fragility curve parameters, which are median and standard deviation, of three damage levels were calculated simultaneously with the same standard deviation to avoid an intersection of fragility curves.

Kircil and Polat (2006) developed analytical seismic fragility curves of the mid-rise reinforced-concrete frame buildings as functions of peak ground acceleration (PGA), elastic pseudo spectral acceleration (Sa) and elastic spectral displacement (Sd). The variations of ground motions were magnitudes, durations and fault distances. The variations of structural material properties were compressive strength of concrete assumed as a normal distribution. The fragility curves were developed by using the least-square method and assumed as a lognormal distribution for 2 damage levels which are yielding and collapse.

Yi et al. (2007) proposed analytical fragility curves as a function of the return period, which is useful in the design, for a bridge by using the maximum likelihood estimation method and assuming as a log-normal distribution. 60 Los Angeles earthquake time histories were used to analyze a bridge response which developed by FEMA SAC. In the model, non-linear plastic hinges were used at the both end of the bridge columns. The plastic hinge behavior was modeled by using the bilinear hysteretic. For the damage levels, Dutta's recommendation was used which established by using real-scaled bridge tests and classified into 5 damage levels according to the drift limit as listed in Table 2-4. They avoided the intersection of fragility curves by using a common log-standard deviation for all damage levels. Finally, they also developed the fragility curves as a function of PGA.

Table 2-4. Description of damage states (Yi et al., 2007)

Damage State	Description	Drift Limits
Almost No Damage	First Yield	0.005
Slight Damage	Cracking and Spalling	0.007
Moderate Damage	Loss of Anchorage	0.015
Extensive Damage	Incipient column collapse	0.025
Complete Damage	Column Collapse	0.050

2.3.2 Damage and fragility curves for tsunamis

For tsunami fragility curves, the tsunami intensity scales developed from past experiences, empirical fragility curves developed from observed data and remote sensing by satellite images were proposed in recently years, which are briefly detailed in the following. Firstly, the overview observed damage data are summarized here.

For the tsunami intensity scale, Shuto (1993) proposed a tsunami intensity and disaster for wooden house, stone house, reinforced-concrete building fishing boat, tsunami control forest and aquaculture raft from the past tsunami events: 4 events in Japan and 4 events outside Japan. The damage of reinforce-concrete buildings was specified by observed damaged data. The tsunami intensity and disaster were classified into 6 levels as a function of the local tsunami height. Papadopoulos and Imamura (2001) developed the tsunami intensity which was classified into 12 levels. The tsunami intensity levels based on the wave amplitude, sensitivity and the effect on the human, natural environment and structures from the past tsunami experience.

Rossetto et al. (2007) investigated the damage of buildings and lifelines due to the 2004 Indian Ocean tsunami in Thailand and Sri Lanka. In the investigation, a tsunami intensity scale was classified into 6 levels based on the tsunami intensity proposed by Papadopoulos and Imamura (2001). Four buildings types were considered: low-rise timber houses, low-rise masonry residential houses, low-rise reinforced-concrete infilled frame and mid-rise reinforced-concrete infilled frame. The low-rise timber houses generally suffered the total collapse. The low-rise masonry residential houses were destroyed and most suffered severe damage for the tsunami height exceeding of 2 m. The low-rise reinforced-concrete infilled frame damaged in infill walls and windows and a few suffered partial failures. The mid-rise reinforced-concrete infilled frame only suffered the collapse of a window and infill panels, even though the run-up exceeded 4 m.

Reese et al. (2007) investigated the effect of the 2006 Java tsunami on buildings in the South of Java and also estimated the damage ratio of buildings and

casualty rates as a function of an inundation height. Four building types were estimated; timber buildings, brick traditional buildings, brick traditional with reinforced-concrete column buildings and reinforced-concrete frame with brick infill wall buildings. In the estimation, damage ratio was defined as the ratio of cost to repair and cost to replace.

Shoji and Moriyama (2007) proposed tsunami fragility curves of a bridge structure. The fragility curves were developed by observed data from the December 26th, 2004 Indian Ocean tsunami in Sri Lanka and Indonesia. There are 58 data in Sri Lanka and 17 data in Indonesia. The observed damaged bridges were classified into 4 damage ranks as listed in Table 2-5. The fragility curves were established by the least-square method and assumed as a lognormal distribution as a function of inundation heights. The inundation height is described as Figure 2-21 and expressed as equation 2-84. The fragility curve can be expressed as equation 2-85.

Table 2-5. Damage pattern of a bridge structure due to a tsunami (Shoji and Moriyama, 2007)

Rank	Damage pattern
A	Washout and fall-down of a deck
B	Movement of a deck, damage to an abutment and scouring and erosion of a soil embankment around an abutment
C	Damage to a deck attachment such as bridge railings
D	No damage

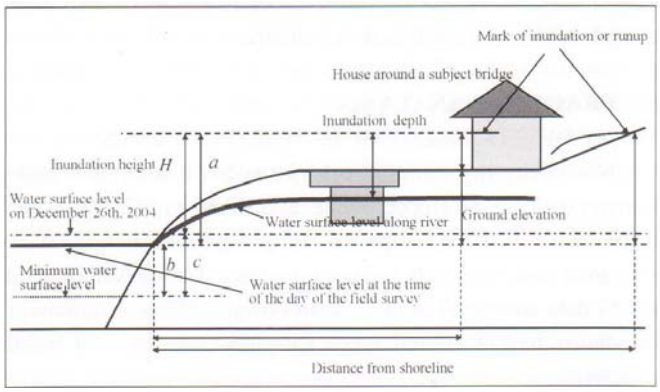

Figure 2-21. Definition of a tsunami inundation height (Shoji and Moriyama, 2007)

$$H = a + b - c \tag{2-84}$$

$$P_c^i = \int_0^z \frac{1}{\sqrt{2\pi}\sigma_y z} \exp\left\{-\frac{1}{2}\left(\frac{\ln z - \mu_y}{\sigma_y}\right)^2\right\} dz \tag{2-85}$$

where

H is inundation height

a is difference of the mark of inundation height and the water surface level at the time on the day of the field survey

b is water surface level at the time on the day of the field survey
c is water surface level in December 26th, 2004
P_c^i is cumulative damage probability of damage rank i
μ_y is mean of the logarithm of the inundation height
σ_y is standard deviation of the inundation height

To solve the unknown variables, μ_y and σ_y, the data is divided with interval of 1 m for data in Sri Lanka and 4 m for data in Indonesia. After that P_c^i is transformed to $\Phi^{-1}\left(P_c^i\right)$ by the inversion of normal distribution function as equation 2-86. Figure 2-22(a) and Figure 2-22(b) show the relationship of $\Phi^{-1}\left(P_c^i\right)$ and $\ln z$ for data in Sri Lanka and data in Indonesia, respectively. For Indonesia data, there is only rank A because the number of damage data for rank B and rank C is not sufficiently obtained for the linear regression analysis. From the relationship, the y-intercept is the value of μ_y / σ_y and the slope is the value of $1/\sigma_y$. These values and the coefficient of determination are shown in Table 2-6. The fragility curves for the data in Sri Lanka and Indonesia are illustrated in Figure 2-23.

$$\Phi^{-1}\left(P_c^i\right) = \frac{\ln z - \mu_y}{\sigma_y} = \frac{1}{\sigma_y}\ln z - \frac{\mu_y}{\sigma_y} \tag{2-86}$$

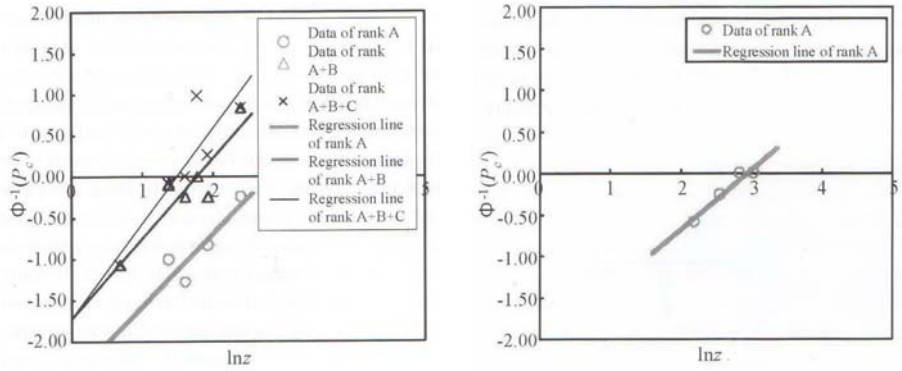

(a) Sri Lanka data (b) Indonesia data

Figure 2-22. Relationship of the data of $\Phi^{-1}\left(P_c^i\right)$ and $\ln z$ (Shoji and Moriyama, 2007)

Table 2-6. Mean, μ_y and Standard deviation, σ_y of inundation height (Shoji and Moriyama, 2007)

Location	Sri Lanka data			Indonesia data
Damage rank	A	A+B	A+B+C	A
Slope	0.88	0.97	1.15	0.7169
Intercept	-2.46	-1.73	-1.74	-2.112
Coefficient of determination	0.79	0.83	0.80	0.94
Mean, μ_y	2.08	1.78	1.51	2.95
Standard deviation, σ_y	1.14	1.03	0.87	1.39

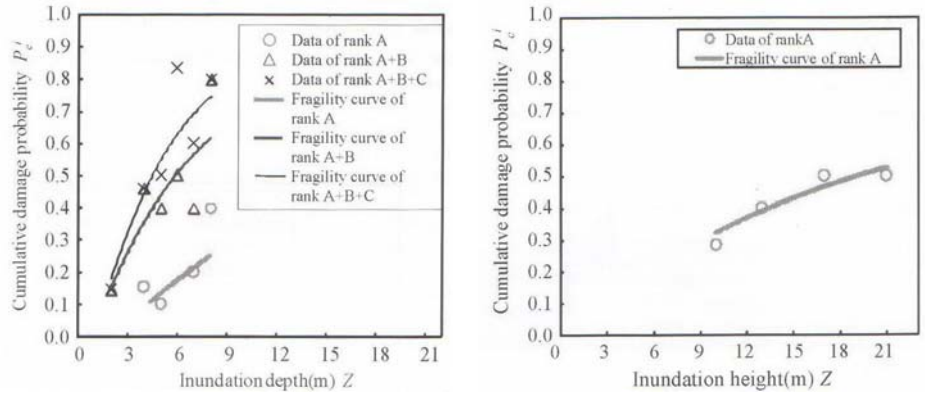

(a) Sri Lanka data (b) Indonesia data

Figure 2-23. Fragility curves of a bridge structure due to a tsunami (Shoji and Moriyama, 2007)

Dias et al. (2009) developed tsunami fragility curves for single-story buildings in Sri Lanka after the December, 26th 2004 tsunami. The single-story buildings were separated into 2 types which depended on the constructional material. The fragility curves were developed from the collected data of the Department of Census and Statistic (DCS), Sri Lanka which covered 47 administrative districts. Only completely damage state was considered. The developed fragility curves were a function of highest submerged height and assumed as a function of lognormal distribution as shown in Figure 2-24.

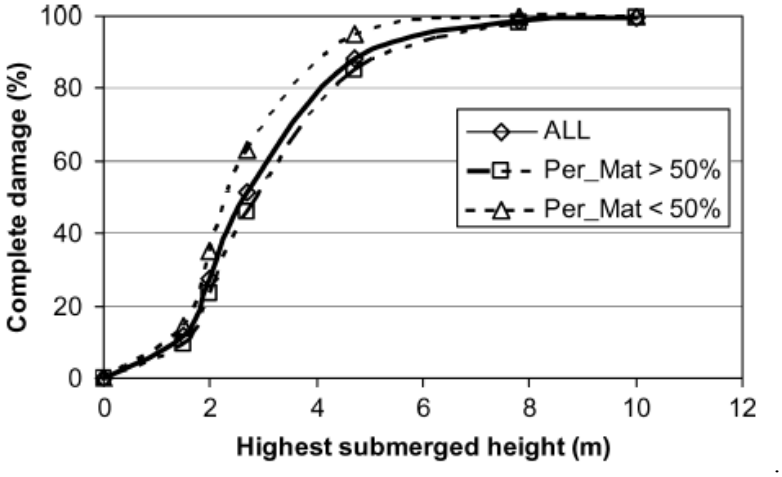

Figure 2-24. Fragility curves of various categories (Dias et al., 2009)

Koshimura et al. (2009) proposed tsunami fragility curves for buildings and casualty from the 2004 tsunami. The fragility curves were developed by using high-resolution satellite images in Banda Aceh, Indonesia, validated tsunami model and least-square fitting. The fragility curves were developed as functions of tsunami inundation depth, current velocity and hydrodynamic force. From the high-resolution

satellite images, the damaged buildings were classified for surviving and destruction from remained and disappeared of the roofs, respectively. The fragility curves were expressed by the cumulative probability of damaged occurrence. The fragility curve was developed as a function of inundation depth with a standardized normal distribution as expressed in equation 2-87. The fragility curves were developed as functions of current velocity and hydrodynamic force with a lognormal distribution as expressed in equation 2-88. The unknown variables, μ and σ (μ' and σ') were an intercept and a slope of the inverse of standard normal (lognormal) distribution and x ($\ln x$), which were fitted by the least-square method. The fitted unknown variables are listed in Table 2-7. The proposed tsunami fragility curves are shown in Figure 2-25 and the casualty curve is shown in Figure 2-26.

$$P(x) = \Phi\left[\frac{x-\mu}{\sigma}\right] \tag{2-87}$$

$$P(x) = \Phi\left[\frac{\ln x-\mu'}{\sigma'}\right] \tag{2-88}$$

where

x is inundation depth (equation 2-87)
is current velocity and the hydrodynamic force (equation 2-88)
Φ is the standard normal (equation 2-87)
is the lognormal distribution (equation 2-88)
μ and σ are mean and standard deviation of x (equation 2-87)
μ' and σ' are mean and standard deviation of $\ln x$ (equation 2-88)

Table 2-7. The unknown variables, μ and σ (μ' and σ') of damaged buildings and casualty (Koshimura et al., 2009)

	x for fragility function $P(x)$	μ	σ	μ'	σ'	R^2
Buildings damage	Inundation depth (m)	2.99	1.12	N/A	N/A	0.99
	Current velocity (m/s)	N/A	N/A	0.80	0.28	0.97
	Hydrodynamic force per width (kN/m)	N/A	N/A	1.47	0.75	0.99
Casualty	Inundation depth (m)	3.75	1.35	N/A	N/A	0.80

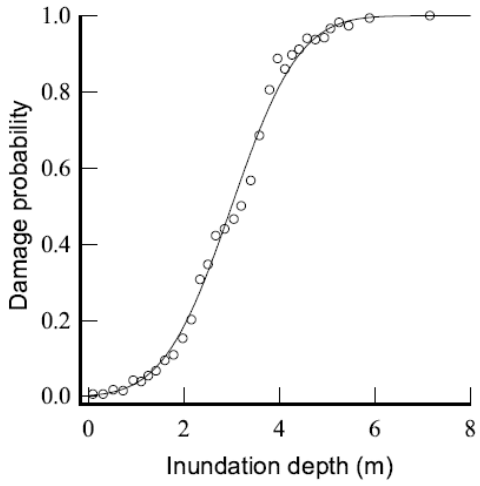

(a) Inundation depth

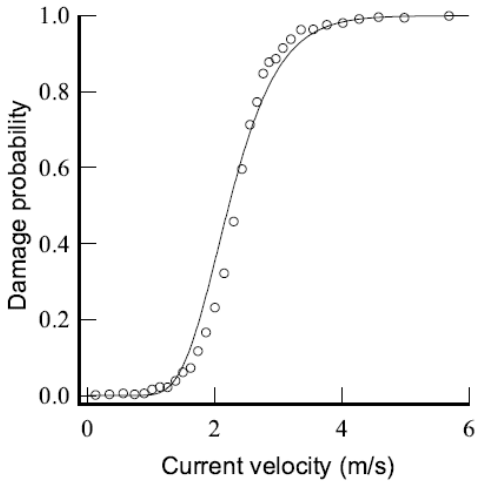

(b) Current velocity

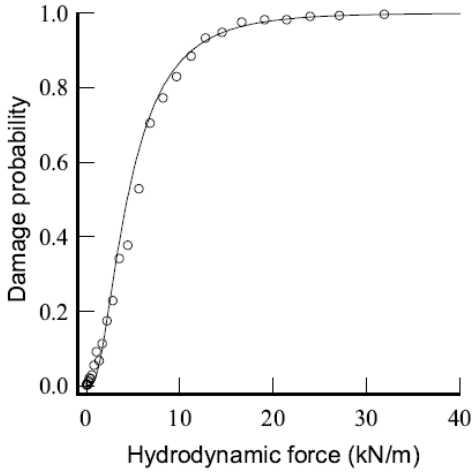

(c) Hydrodynamic force

Figure 2-25. Fragility curves of building damage in Banda Aceh, Indonesia as function of inundation depth, current velocity and hydrodynamic force (Koshimura et al., 2009)

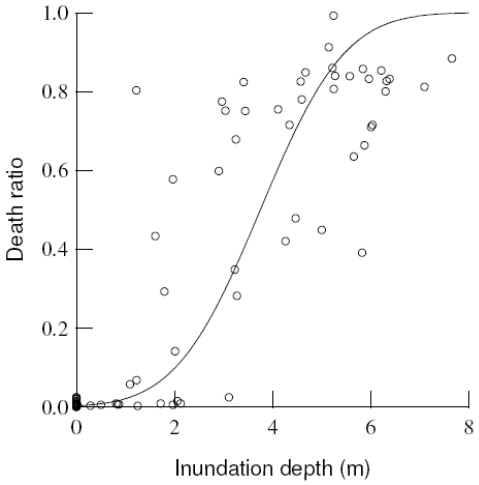

Figure 2-26. Casualty curve in Banda Aceh, Indonesia (Koshimura et al., 2009)

Suppasri et al. (2011) developed tsunami fragility curves for buildings in Thailand from the 2004 tsunami. The fragility curves were developed by using high-resolution satellite images in Khao Lak area, Phung Nga province, Thailand, validated tsunami model and least-square fitting. The fragility curves were developed as functions of tsunami inundation depth, current velocity and hydrodynamic pressure by assuming as a lognormal distribution. From the high-resolution satellite images, the damaged buildings were classified for surviving and destruction from remained and disappeared of the roofs, respectively. The developed fragility curves are expressed as in equation 2-89. The unknown variables, μ' and σ' were an intercept and a slope of the inverse of the standard lognormal distribution and $\ln x$, which were fitted by the least-square method. The developed tsunami fragility curves are shown in Figure 2-27.

$$P(x) = \Phi\left[\frac{\ln x - \mu'}{\sigma'}\right] \tag{2-89}$$

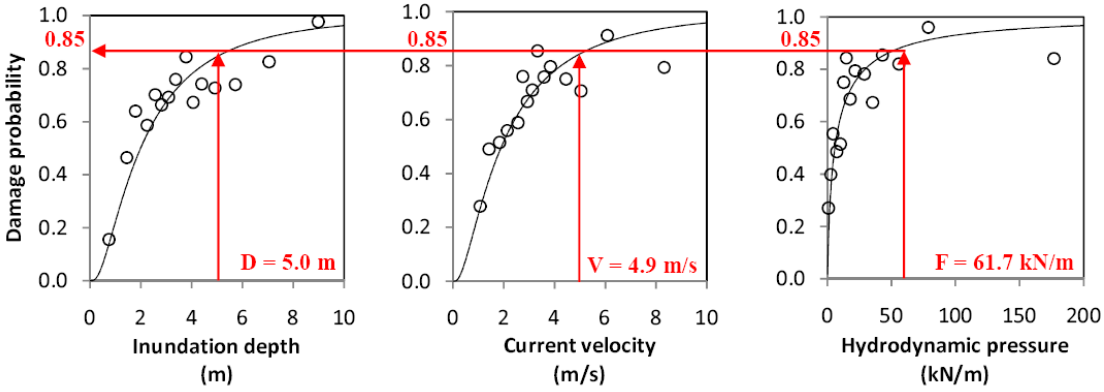

(a) Inundation depth (b) Current velocity (c) Hydrodynamic pressure

Figure 2-27. Fragility curves of building damage in Khao Lak area, Phung Nga province, Thailand as function of inundation depth, current velocity and hydrodynamic pressure (Suppasri et al., 2011)

CHAPTER III
TSUNAMI FLOW VELOCITY

3.1 Introduction

This chapter focuses on tsunami flow velocities from proposed formulations in past studies and field observations. Tsunami flow velocities on land have high uncertainties. In this research, the variation of tsunami flow velocities is considered in analyzing building responses and developing the tsunami fragility curve. The proposed formulations in past studies are summarized in section 3.2. Section 3.3 explains about tsunami velocities of the 2004 Indian Ocean tsunami in Patong beach and Kamala beach, Phuket province, Thailand. In Section 3.4, the tsunami flow velocities of the March 2011 Tohoku, Japan tsunami are estimated from videos by estimating movement distances from reference dimensions measured from known objects or Google Earth or satellite images in Kamaishi city, Ofunato city, Kesennuma city and Iwaki city.

3.2 Study on Tsunami Flow Velocities

After tsunamis, several researchers reported tsunami run-ups and inundation depths along coastlines based on field surveys (DPRI, 2006, Fritz et al., 2006, Tsuji et al., 2006, Bapat and Murty, 2008, The 2011 Tohoku Earthquake Tsunami Joint Survey Group, 2011). However, the information on tsunami velocities is scarce. In this section, the proposed estimating tsunami flow velocities are summarized.

Ramsden and Raichlen (1990) investigated forces acting on a vertical wall due to bores from experiments. The proposed celerity coefficient, N_F, are 1.55 for the smallest bore and be 1.8 for the other bores.

FEMA 55 (2000) proposed the lower bound and upper bound velocities of the flood flow as equal to h/t and $1.0\sqrt{gh}$, respectively, where h is an inundation depth, g is the gravitational acceleration, and t is the time equal to 1.0. FEMA 55 (2000) also proposed the velocity of the conservative flood flow for a tsunami as equal to $2.0\sqrt{gh}$.

CCH (2000) proposed formulas used to calculate the designed forces due to flood. The flood flow velocity was defined equal to the depth of water at the structure location.

Asakura et al. (2002) proposed tsunami wave force formulas acting on land structures by using experimental results in a hydraulic flume. From their experimental results, the velocities of the tsunami wave ranged from $0.1\sqrt{gh}$ to $1.5\sqrt{gh}$.

Fritz et al. (2006) analyzed the tsunami flow velocities from the 2004 Indian Ocean tsunami by using videos recorded by survivors in Banda Aceh, Indonesia. The particle image velocimetry analysis was applied to rectify video images without any physical distortions. The video frames were transformed to the real coordinate by using the direct linear transformation. The tsunami flow velocities in Banda Aceh were about 2 - 5 m/s as shown in Figure 3-1. From Figure 3-1, the tsunami flow velocities are calculated in term of the inundation depth as listed in Table 3-1. The tsunami velocities range from $0.53\sqrt{gh}$ to $1.31\sqrt{gh}$.

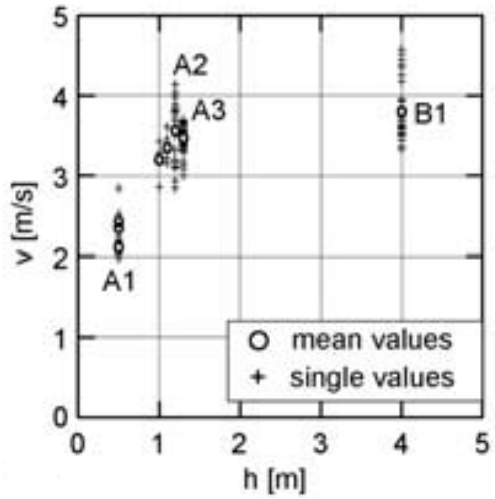

Figure 3-1. Analyzed tsunami flow velocity versus inundation depths (Fritz et al., 2006)

Table 3-1. Calculated tsunami flow velocity in term of inundation depth from the analyzed tsunami flow velocity by Fritz et al. (2006)

Point	h (m)	Velocity (m/s)		Froude number	
		From	To	From	To
A1	0.5	2.1	2.9	0.95	1.31
A2	1.0	2.9	3.2	0.93	1.02
	1.1	3.2	3.6	0.97	1.10
	1.2	2.9	4.1	0.83	1.19
A3	1.3	3.0	3.7	0.84	1.04
B1	4.0	3.3	4.6	0.53	0.73

Matsutomi et al. (2006) reported results of field surveys in Southern Thailand and Northern Sumatra from the 2004 tsunami. From the observed tsunami inundation depth, the tsunami flow velocities were estimated by using equation 3-1, where h_f and h_r are inundation depths at the front and back side of building, respectively. The approximated tsunami flow velocities were about 3 - 4 m/s in Patong beach area, Thailand, 6 - 8 m/s in Khao Lak area, Thailand and 5 - 16 m/s in Northern Sumatra, Indonesia. From the ranging of tsunami inundation depths and tsunami flow velocities, the tsunami flow velocities are calculated in term of the inundation depth as listed in Table 3-2. The tsunami velocities range from $0.43\sqrt{gh}$ to $1.11\sqrt{gh}$.

$$u = \sqrt{2g\left(h_f - h_r\right)} \tag{3-1}$$

Table 3-2. Calculated tsunami flow velocity in term of inundation depth from the analyzed tsunami flow velocity by Matsutomi et al. (2006)

Location	h (m)	Velocity (m/s)	Froude number
Patong, Thailand	2	3 - 4	0.68 - 0.90
Khao Lak, Thailand	4 - 7	6 - 8	0.96 - 0.97
Banda Aceh	3.9	5.8	0.94
	4.0	5.2	0.83
	4.9	7.7	1.11
West coast of Northern Sumatra	30.5	16.0	0.92

Yeh (2006) proposed the analytical solutions to estimate the maximum moment flux of the nonlinear shallow-water wave theory for a uniform beach slope. The algorithms in this study based on the study of Carrier et al. (2003), which developed the exact-solution to evaluate wave heights and wave velocities on shore in the dimensionless form from the initial conditions. The proposed equation was obtained from the fitting envelope of 9 initial conditions with four initial wave forms. The proposed equations are expressed in equation 2-19 and equation 2-20 those base on the distance and the ground elevation at the maximum runup height, respectively.

Lukkunaprasit et al. (2010) verified the tsunami velocity from their full-scale pushover test on the former office of Thai Meteorological Department located in Khao Lak area, Phung-Nga province, Thailand. This building is a one-story reinforced-concrete building and suffered the inundation depth of 4.4 m from the 2004 Indian Ocean tsunami. The flow velocity was calculated from the lateral forces assumed as hydrodynamic forces. The effect of an open terrain was considered to

estimate the flow velocity. The proposed tsunami flow velocities, that acted on the building, range from $1.20\sqrt{gh}$ to $1.36\sqrt{gh}$.

Matsutomi and Okamoto (2010) proposed the relationship of the inundation flow velocity and inundation depth from field surveys of the past events. The inundation flow velocity was estimated by using Bernoulli's theorem and the inundation depth, and examined with experiments. The tsunami flow velocities were calculated from equation 3-1, where h_f and h_r are inundation depths at the front and back side of building, respectively. The proposed tsunami velocities range from $0.7\sqrt{gh_r}$ to $2.0\sqrt{gh_r}$ as shown in Figure 3-2, where R is a tsunami height or a nearest tsunami run-up height from the sea level.

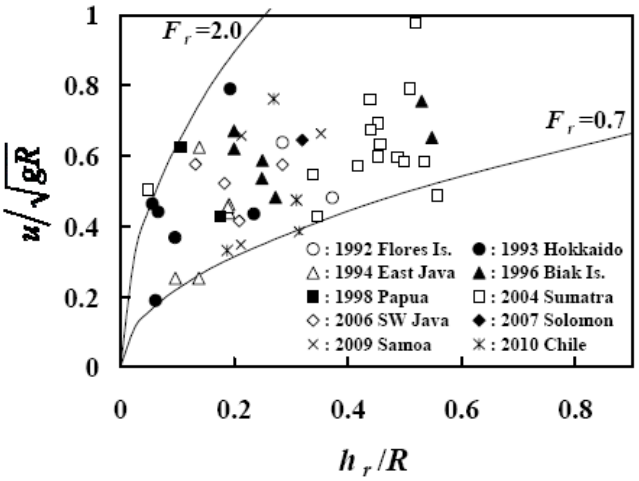

Figure 3-2. Relationship between nondimensionalized depth h_r / R and inundation flow velocity $u / \sqrt{gR}$ inundation depth for the case used inundation depth on the back side (Matsutomi and Okamoto, 2010)

EERI (2011) reported the tsunami flow velocities in Sendai of the March 2011 Tohoku, Japan tsunami. The tsunami velocities were analyzed by using videos recorded on a helicopter. The movement distances were measured in the field. The average velocities were 6.7 m/s for bore travelling in the Natori River and 6.3 m/s for the case on a farmland. For the Natori River, the observed tsunami inundation depth is 1.2 m. The tsunami flow velocity for a bore travelling in the Natori River in term of the inundation depth is $1.94\sqrt{gh}$.

Koshimura and Hayashi (2012) analyzed the tsunami flow velocity and estimated the tsunami force of the 2011 Tohoku, Japan tsunami in Miyagi Prefecture, Tohoku, Japan by using image processing of recorded videos. The video frames were

rectified with identified ground control points by 2-D projective transformation. The tsunami flow velocity was estimated as 6 m/s. with the inundation depth of 5 m and the Froude number of 0.90.

Fritz et al. (2012) analyzed the tsunami current velocities and measured the tsunami height of the 2011 Japan tsunami in the Kesennuma Bay by using videos recorded by survivors. The particle image velocimetry analysis was applied to rectify the video images similarly as Fritz et al. (2006). The tsunami heights were measured by terrestrial laser scanning based on the light detection and ranging. The tsunami current velocities range from 3 to 11 m/s. The maximum tsunami height is 9 m. The velocity of the March 2011 Tohoku, Japan tsunami at the Kesennuma Bay approaches about $1.0\sqrt{gh}$.

3.3 Flow Velocity in Thailand of the 2004 Indian Ocean Tsunami

CU (2007) analyzed the tsunami flow velocity from the recorded videos from the 2004 Indian Ocean tsunami in Thailand. Recorded videos of the tsunami flow in Thailand are collected from web sites. Four cases were analyzed in Patong beach and Kamala beach, Phuket province, Thailand. The locations of Patong beach and Kamala beach are shown in Figure 3-3. The method of estimating tsunami flow velocities comprises selecting video frame, determining recorded location, measuring movement distance and calculating the velocity. Movement distances in recorded videos are measured in the field. Finally, tsunami flow velocities can be computed by equation 3-2. The estimated tsunami flow velocities in Thailand are summarized in Table 3-3. The tsunami flow velocities range about 1 - 3 m/s in Patong beach and 7 - 9 m/s in Kamala beach.

$$Velocity = \frac{\text{Movement Distance}}{\text{No. of Frame/Frame Rate}} \tag{3-2}$$

Table 3-3. The estimated tsunami flow velocities in Thailand (CU, 2007)

Case No.	Location	Velocity (m/s)
1	Patong Beach	3.2
2		1.4
3	Kamala Beach	7.0
4		8.9

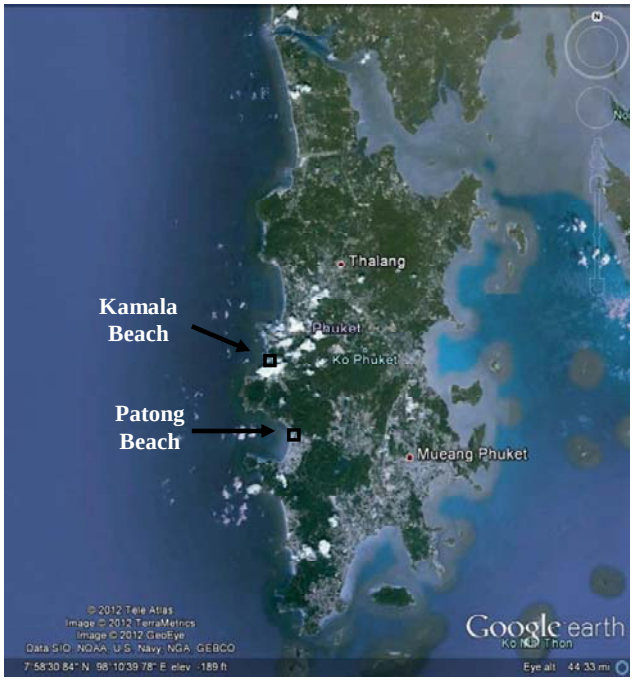

Figure 3-3. Locations of cities in Thailand where videos were recorded (Google Earth, 2011 : online)

3.4 Flow Velocities in the March 2011 Tohoku, Japan, Earthquake and Tsunami

The March 2011 Tohoku, Japan tsunami caused severe damage to many buildings, bridges and other lifelines. More than 20,000 people were killed and missing at the Pacific coast of Tohoku in Japan (JMA, 2011). From this event, videos recording tsunami flows on land were available on web sites. In this section, tsunami flow velocities on land are estimated from videos by estimating movement distances from reference dimensions measured from known objects or Google Earth or satellite images in Kamaishi City, Ofunato City, Kesennuma City and Iwaki City. The inundation depth is also estimated in some cases. The relation between tsunami flow velocity and inundation depth is compared with proposed formulations in past studies.

3.4.1 Method for estimation of tsunami flow velocity

Video frames are selected from videos according to three criteria; 1) movement track of objects should be perpendicular to the direction of a camera, 2) the observed object should flow close to and parallel to the object with known dimensions as illustrated in Figure 3-4, and 3) the observed object should flow with the same velocity as the tsunami. The locations where videos were taken are determined with an aid of Google Street View.

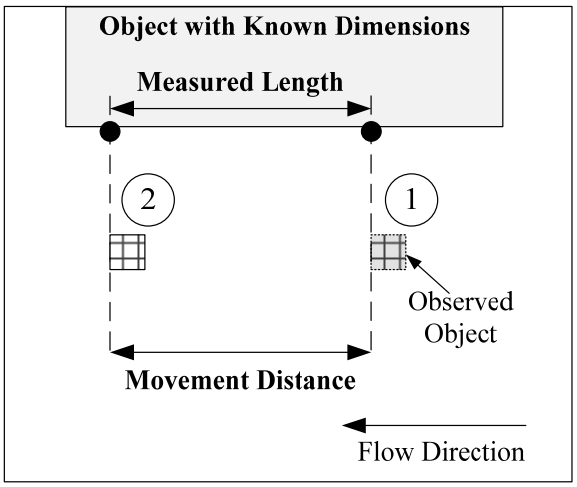

Figure 3-4. Definition of terms used to determine velocities

The dimensions can be determined by measurement in Google Earth or satellite images. Two high-resolution satellite images are used for Kamaishi City and Kesennuma City. The satellite image of Kamaishi City was taken on 5 May 2010 by the GeoEye-1 satellite with a resolution of 50 cm. For Kesennuma City, the satellite image was taken on 22 April 2009 by QuickBird satellite with a resolution of 60 cm. The tsunami flow velocity can be computed by equation 3-3.

$$Velocity = \frac{\text{Movement distance}}{\text{Time between two frames}} \tag{3-3}$$

3.4.2 Recorded videos used in analysis

Videos were recorded using handheld video cameras by survivors and made available on websites. Eight videos are selected based on the criteria stated above. There are three videos in Kamaishi City, one video in Ofunato City, three videos in Kesennuma City and one video in Iwaki City. The locations are shown in Figure 3-5.

Ten cases are analyzed to estimate the tsunami flow velocity as listed in Table 3-4. There are four cases in Kamaishi City. one case in Ofunato City, four cases in Kesennuma City and one case in Iwaki City as shown in Figure 3-6 to Figure 3-9, respectively. In Kesennuma City, Cases No.6 and 9 are at the same location.

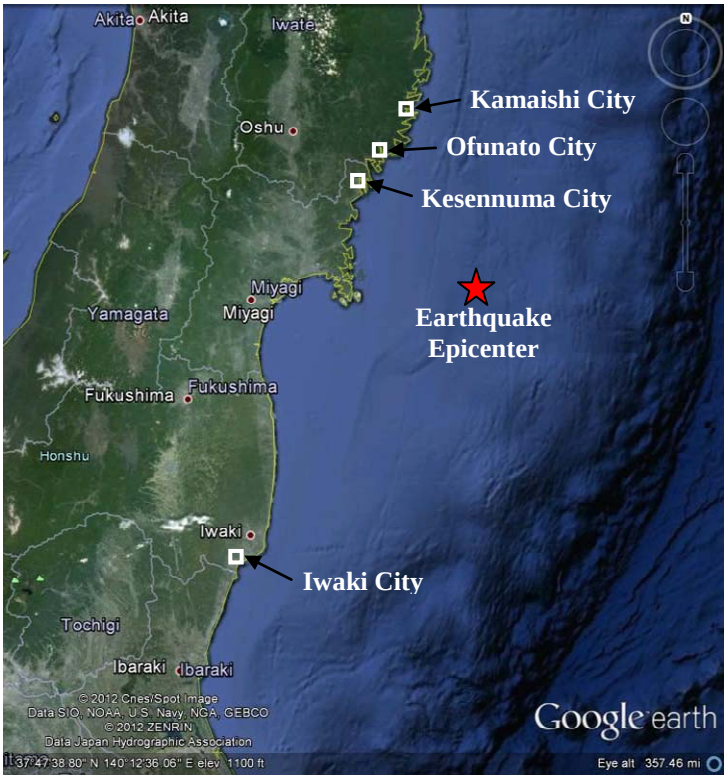

Figure 3-5. Locations of cities where videos were recorded (Google Earth, 2011 : online)

Table 3-4. Locations of recorded videos and video frames

Case No.	Location	Coordinates		Frame (s)		Videos No.	Video Source
		Latitude	Longitude	From	To		
1	Kamaishi, Iwate	39.27454	141.88876	123.3	124.6	1	http://www.guardian.co.uk/world/video/2011/mar/14/japan-tsunami-amateur-footage-video
2		39.27498	141.88818	9.4	10.2	2	http://www.youtube.com/watch?v=Nnu4K7mvJwY
3		39.27486	141.88825	11.6	12.2		
4		39.27512	141.88961	129.4	133.0	3	http://www.youtube.com/watch?v=M535NGr9vbo
5	Ofunato, Iwate	39.05628	141.72298	123.9	125.4	4	http://www.youtube.com/watch?v=oKzEQwAx0m8
6	Kesennuma, Miyagi	38.89893	141.57822	55.8	57.0	5	http://www.youtube.com/watch?v=j5upJN7Sgzs
7		38.89876	141.57815	64.7	66.1		
8		38.90754	141.58001	21.1	23.0	6	http://www.youtube.com/watch?v=hK1zBRA9T3k
9		38.89893	141.57822	239.3	240.7	7	http://www.youtube.com/watch?v=2uJN3Z1ryck&feature=related
10	Iwaki, Fukushima	36.91204	140.79252	2.6	6.9	8	http://www.youtube.com/watch?v=q8ufzRIVipI

Figure 3-6. Cases in Kamaishi City (Google Earth, 2011 : online)

Figure 3-7. Case in Ofunato City (Google Earth, 2011 : online)

Figure 3-8. Cases in Kesennuma City (Google Earth, 2011 : online)

Figure 3-9. Cases in Iwaki City (Google Earth, 2011 : online)

3.4.3 Estimation of tsunami flow velocity

1) Kamaishi City, Iwate prefecture

There are four cases in Kamaishi City as shown in Figure 3-6. From Video No.1, between frames at 123.3 s and 124.6 s, three cars flowed in front of a warehouse from Point No.1 to Point No.2 as shown in Figure 3-10(a). The flow direction is perpendicular to the shoreline as shown in Figure 3-10(b). The length of the warehouse is measured from the GeoEye-1 satellite image as in Figure 3-10(c). The measured length is 5.3 m, and the time that three cars flowed from Points No.1 to 2 is 1.3 s. Thus, the tsunami flow velocity of Case No.1 is estimated as 4.1 m/s.

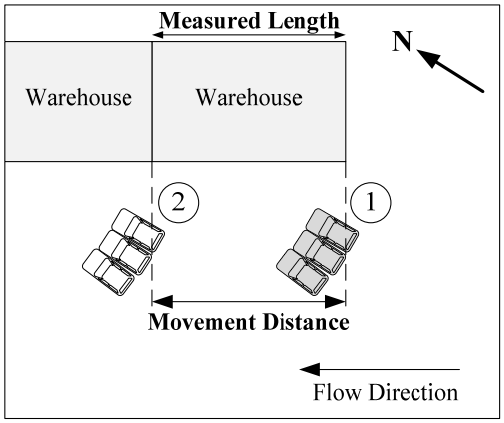

(a) Movement of observed object (Video No.1 from 123.3 s to 124.6 s)

(b) Flow direction (Google Earth, 2011 : online) (c) Measurement from satellite image

Figure 3-10. Details of Case No.1 in Kamaishi City

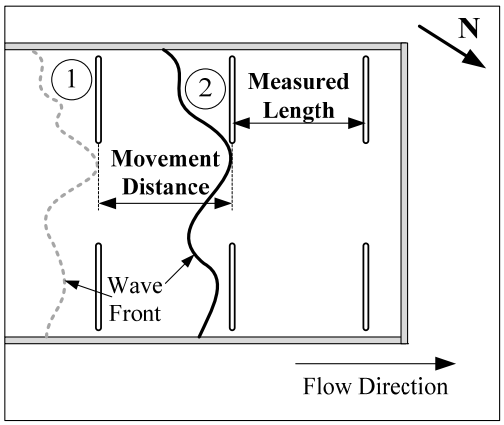

(a) Movement of observed object (Video No.2 from 9.4 s to 10.2 s)

(b) Flow direction (Google Earth, 2011 : online) (c) Measurement from satellite image

Figure 3-11. Ddetails of Case No.2 in Kamaishi City

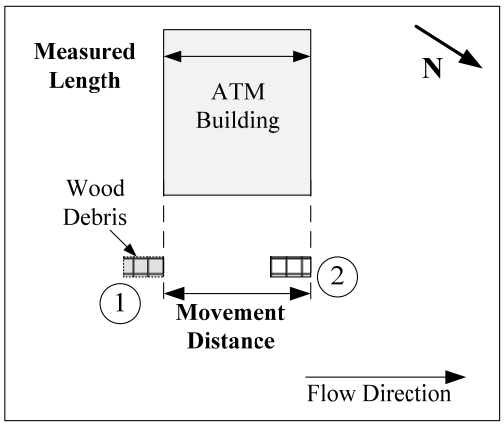

(a) Movement of observed object (Video No.2 from 11.6 s to 12.2 s)

(b) Flow direction (Google Earth, 2011 : online) (c) Measurement from satellite image

Figure 3-12. Details of Case No.3 in Kamaishi City

For Case No.2, the tsunami flowed in a parking area as shown in Figure 3-11(a). The flow direction is perpendicular to the shoreline as in Figure 3-11(b). The wave front passed the lane marking No.1 in Figure 3-11(a) at 9.4 s to the lane marking No.2 at 10.2 s. The distance between the lane markings is measured from the GeoEye-1 satellite image as 2.5 m as shown in Figure 3-11(c). Hence, the tsunami flow velocity in Case No.2 is estimated as 3.1 m/s.

The tsunami flowed past an ATM building from Point No.1 to Point No.2 in frames at 11.6 s and at 12.2 s, respectively as shown in Figure 3-12(a). The flow direction is quite perpendicular to the shoreline as shown in Figure 3-12(b). The movement distance is considered from the width of the ATM building, measured from the GeoEye-1 satellite image as 3.0 m as shown in Figure 3-12(c). The tsunami flow velocity for Case No.3 is estimated as 5.0 m/s.

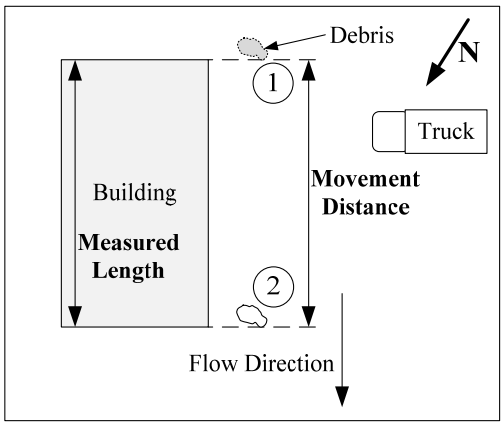

(a) Movement of observed object (Video No.3 from 129.4 s to 133.0 s)

(b) Flow direction (Google Earth, 2011 : online) (c) Measurement from satellite image

Figure 3-13. Details of Case No.4 in Kamaishi City

For Case No.4, the tsunami flowed past the building as shown in Figure 3-13(a). The flow direction is shown in Figure 3-13(b). The debris flowed from Point No.1 at 129.4 s to Point No.2 at 133.0 s in Video No.3. The building length is 9.7 m as measured from the GeoEye-1 satellite image in Figure 3-13(c). Hence, the tsunami flow velocity of this case is estimated as 2.7 m/s.

2) Ofunato City, Iwate prefecture

A car flowed from the first pole at Point No.1 to the second pole at Point No.2 as in Figure 3-14(a). The tsunami flowed in the direction quite perpendicular to the shoreline as shown in Figure 3-14(b). The movement distance is the distance between 2 poles. The distance between 2 poles is estimated by the known width of the moving car. Hence, the distance between 2 poles can be estimated as 3.2 m. The time between Point No.1 to Point No.2 is 1.5 s. The tsunami flow velocity is estimated as 2.1 m/s.

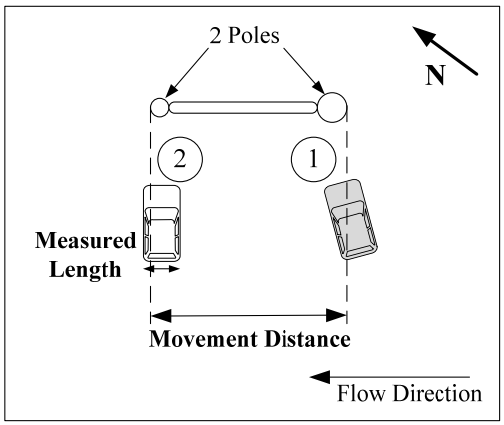

(a) Movement of observed object (Video No.4 from 123.9 s to 125.4 s)

(b) Flow direction (Google Earth, 2011 : online)

Figure 3-14. Details of Case No.5 in Ofunato City

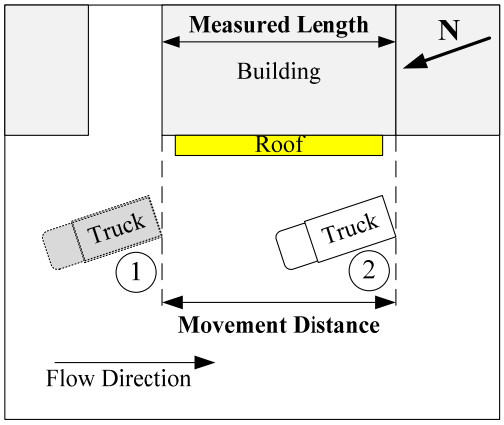

(a) Movement of observed object (Video No.5 from 55.8 s to 57.0 s)

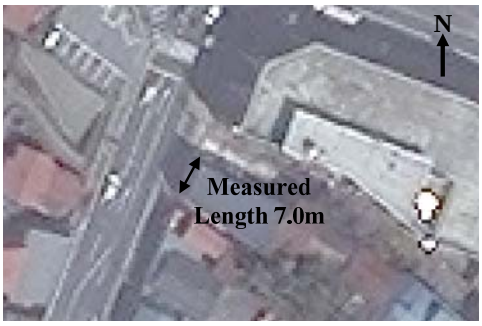

(b) Flow direction (Google Earth, 2011 : online) (c) Measurement from satellite image

Figure 3-15. Details of Case No.6 in Kesennuma City

3) Kesennuma City, Miyagi prefecture

There are four cases in Kesennuma City. The dimensions are estimated by measurement in the QuickBird satellite image with a resolution of 0.5 m. For Case No.6, a white truck flowed past a building from Point No.1 to Point No.2 as shown in Figure 3-15(a). The tsunami flow direction is quite parallel to shoreline as shown in Figure 3-15(b). The building width is measured from the QuickBird satellite image as 7.0 m in Figure 3-15(c). Therefore, the tsunami flow velocity of this case is estimated as 5.8 m/s.

The location of Case No.7 is close to the location of Case No.6. Between the frames at 64.7 s and at 66.1 s in Video No.5, a car flowed from Point No.1 to Point No.2 past the house in Figure 3-16(a). The tsunami flow direction is the same as Case No.6 as shown in Figure 3-16(b). The house width is measured from the QuickBird satellite image as 6.8 m in Figure 3-16(c). Hence, the tsunami flow velocity of Case No.7 is estimated as 4.9 m/s.

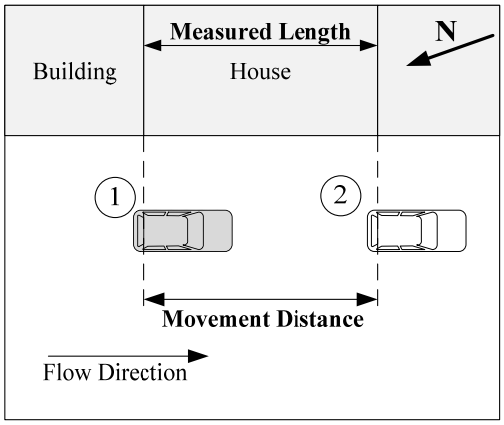

(a) Movement of observed object (Video No.5 from 64.7 s to 66.1 s)

(b) Flow direction (Google Earth, 2011 : online)

(c) Measurement from satellite image

Figure 3-16. Details of Case No.7 in Kesennuma City

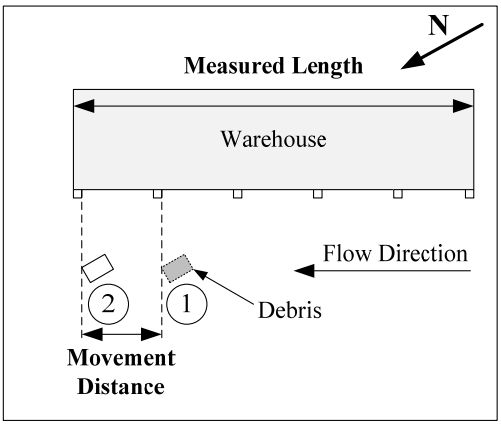

(a) Movement of observed object (Video No.6 from 21.1 s to 23.0 s)

(b) Flow direction (Google Earth, 2011 : online) (c) Measurement from satellite image

Figure 3-17. Details of Case No.8 in Kesennuma City

For Case No.8, the debris flowed past the last bay of a warehouse from Point No.1 to Point No.2 between the frames at 21.1 s and at 23.0 s as shown in Figure 3-17(a). The tsunami flow direction is parallel to the shoreline as shown in Figure 3-17(b). The bay width of the warehouse is estimated as 5.7 m by the satellite image in Figure 3-17(c). The tsunami flow velocity is estimated as 3.0 m/s.

The location of Case No.9 is the same as that of Case No.6. A bag flowed past a building from Point No.1 to Point No.2 between the frames at 239.3 s and 240.7 s in Video No.7 as shown in Figure 3-18(a). The tsunami flowed to the South as in Figure 3-18(b). The estimated building width is 7.0 m measured from the QuickBird satellite image in Figure 3-18(c). The tsunami flow velocity of Case No.9 is estimated as 5.0 m/s.

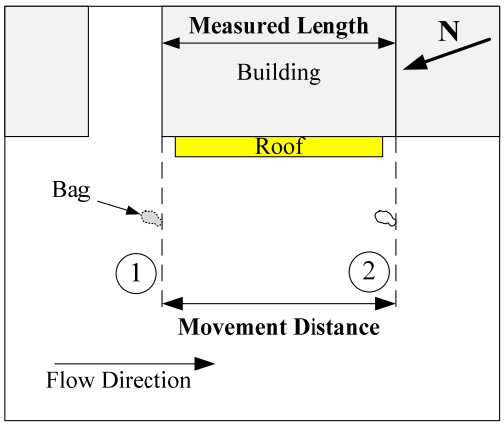

(a) Movement of observed object (Video No.7 from 239.3 s to 240.7 s)

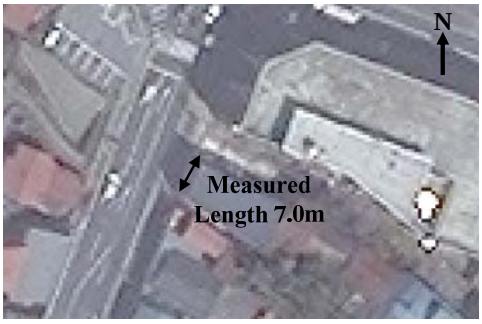

(b) Flow direction (Google Earth, 2011 : online) (c) Measurement from satellite image

Figure 3-18. Details of Case No.9 in Kesennuma City

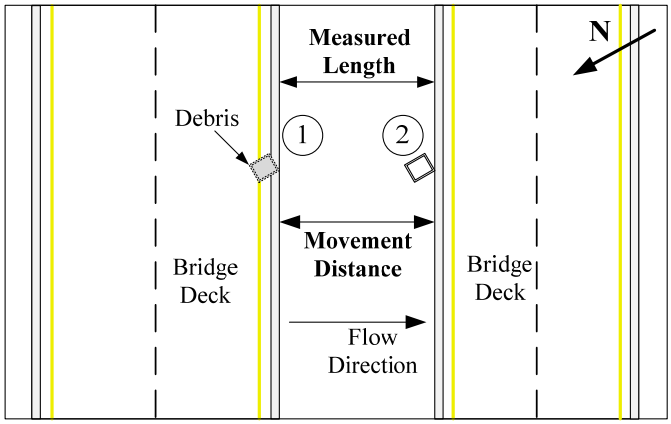

(a) Movement of observed object (Video No.8 from 2.6 s to 6.9 s)

(b) Flow direction (Google Earth, 2011 : online) (c) Measurement from Google Earth

Figure 3-19. Details of Case No.10 in Iwaki City

4) Iwaki City, Fukushima prefecture

In Case No.10, the debris flowed underneath 2 bridge decks from Point No.1 to Point No.2 between the frames at 2.6 s and at 6.9 s as shown in Figure 3-19(a). The tsunami flow direction is along the river as in Figure 3-19(b). The estimated distance between 2 bridge decks is 6.3 m measured from Google Earth as shown in Figure 3-19(c). The velocity is estimated as 1.5 m/s.

The estimated tsunami flow velocities of all cases are summarized in Table 3-5. The analyzed tsunami flow velocities are about 3 - 5 m/s in Kamaishi City, 2 m/s in Ofunato City, 3 - 6 m/s in Kesennuma City and 2 m/s in Iwaki City. In Kamaishi City, the locations of Cases No.2 and 3 are very close, but the tsunami flow velocities of them are 3.1 m/s and 5.0 m/s, respectively. In Kesennuma City, Cases No.6 and 9 are the same location, but the tsunami flow velocities of them are 5.8 m/s and 5.0 m/s. The tsunami flow velocity of Case No.7, whose the location is close to the location of Cases No.6 and 9, is 4.9 m/s

Table 3-5. The tsunami flow velocities

Case No.	Location	Object		Time (sec)	Distance (m)	Velocity (m/s)
		Moving	Reference			
1	Kamaishi, Iwate	3 cars	Warehouse	1.3	5.3	4.1
2		Front Wave	Parking Lane	0.8	2.5	3.1
3		Wood Debris	ATM Building	0.6	3.0	5.0
4		Debris	Building Length	3.6	9.7.5	2.7
5	Ofunato, Iwate	White Car	2 Poles	1.5	3.2	2.1
6	Kesennuma, Miyagi	White Truck	Building	1.2	7.0	5.8
7		White Car	House	1.4	6.8	4.9
8		Debris	One Span of Warehouse	1.9	5.7	3.0
9		Bag	Building	1.4	7.0	5.0
10	Iwaki, Fukushima	Debris	2 Bridges	4.3	6.3	1.5

The tsunami flow directions for all cases are summarized in Figure 3-20. The tsunami flow directions in Kamaishi City, Ofunato City and Iwaki City are perpendicular to the shoreline, but the tsunami flow directions of all cases in Kesennuma City are quite parallel to the shoreline. The flow direction on land in a city depends on many factors, such as building layouts, obstruction and topography.

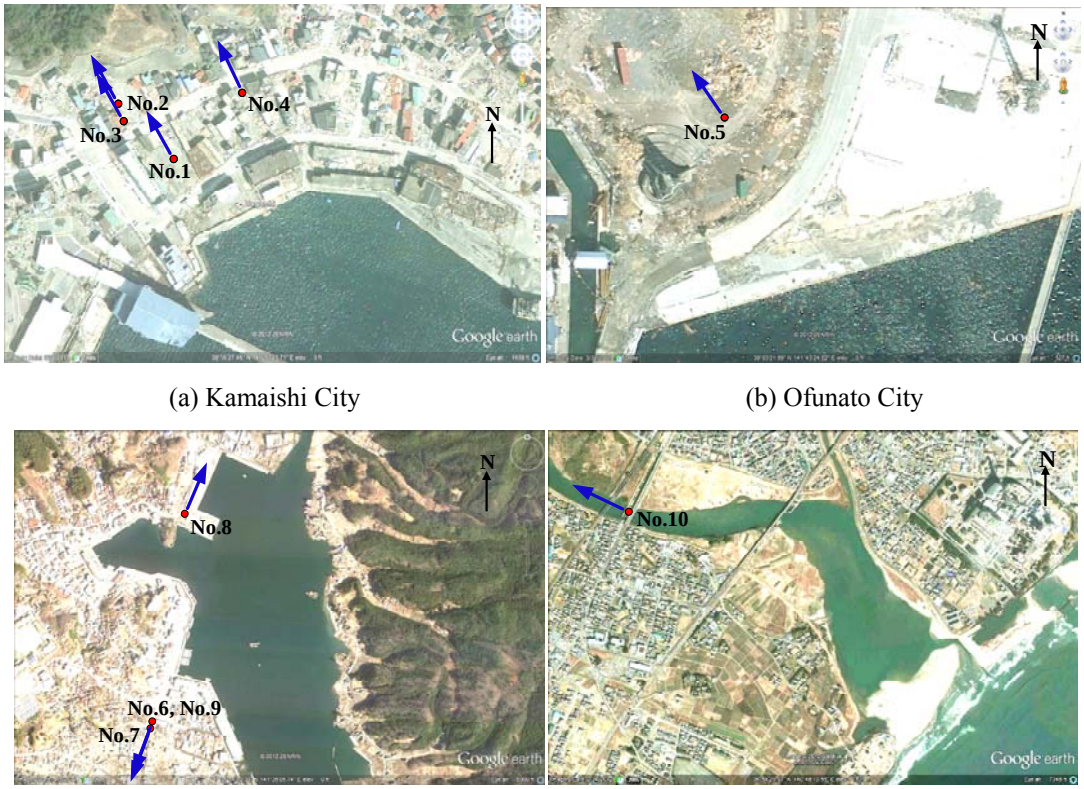

(a) Kamaishi City (b) Ofunato City

(c) Kesennuma City (d) Iwaki City

Figure 3-20. Summary of tsunami flow directions for all cases (Google Earth, 2011 : online)

3.4.4 Relation of tsunami flow velocity and inundation depth

From the recorded videos, inundation depths can be estimated for four cases; Case No.4 in Kamaishi City and Cases No.6, 7 and 9 in Kesennuma City as listed in Table 3-6. For Case No.4, the inundation depth is estimated from the inundated of truck wheels in Figure 3-13(a). Halves of truck wheels are inundated; therefore, the inundation depth of Case No.4 is estimated as 0.5 m. For Cases No.6, 7 and 9, the inundation depths are estimated by using Google Street View and deriving vertical dimensions from horizontal dimensions known from satellite images. The estimated inundation depths of Cases No.6, 7 and 9 are 1.5 m, 2.5 m and 3.0 m, respectively. All analyzed tsunami flow velocities are less than $1.5\sqrt{gh}$. The analyzed results in Kesennuma City are about $1.0\sqrt{gh}$, which agrees with the results by Fritz et al. (2012). From the reviews on tsunami flow velocity, Tsunami flow velocities from proposed formulations in past studies are summarized in Table 3-7. The comparison of the analyzed tsunami flow velocity with proposed velocity equations and observation is shown in Figure 3-21. The analyzed and estimated tsunami flow velocities from the past events are mostly in the range from $0.7\sqrt{gh}$ to $1.5\sqrt{gh}$.

Table 3-6. The estimated inundation depth from the recorded videos and the tsunami flow velocities

Case No.	Location	Estimated Inundation Depth (m)	Velocity (m/s)	Froude Number ($F = v/\sqrt{gh}$)
4	Kamaishi, Iwate	0.5	2.7	1.2
6	Kesennuma, Miyagi	1.5	5.8	1.5
7		2.5	4.9	1.0
9		3.0	5.0	0.9

Table 3-7. Tsunami flow velocities from proposed formulations in past studies

Proposed	From	Velocity (m/s)	Remark
Ramsden and Raichlen (1990)	Experiments	$1.8\sqrt{gh}$	-
FEMA 55 (2000)	Code	h/t	Lower Bound
		$1.0\sqrt{gh}$	Upper Bound
		$2.0\sqrt{gh}$	Tsunami
CCH (2000)	Code	h/t	-
Asakura et al. (2002)	Experiments	$1.5\sqrt{gh}$	-
Lukkunaprasit et al. (2010)	The 2004 tsunami in Thailand	$1.2\sqrt{gh} - 1.36\sqrt{gh}$	-
Matsutomi and Okamoto (2010)	Past Tsunami Events	$0.7\sqrt{gh_r} - 2.0\sqrt{gh_r}$	h_r is inundation depth at back side of building

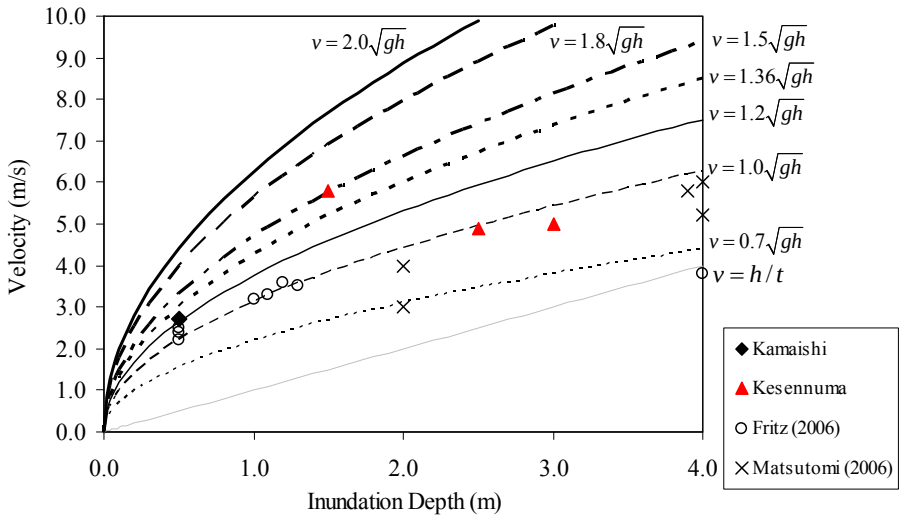

Figure 3-21. The relationship of the tsunami flow velocity and tsunami inundation depth

3.5 Discussion

This chapter focuses on the uncertainty of tsunami flow velocities from proposed formulations in past studies and past events. Tsunami flow velocities on land have high uncertainties.

1) From the 2004 Indian Ocean tsunami, the tsunami flow velocities on land are estimated from recorded videos in Patong beach and Kamala beach in Phuket province, Thailand. The movement distances in recorded videos are measured in the

field. The analyzed tsunami flow velocities are estimated as about 1 - 3 m/s in Patong beach and 7 - 9 m/s in Kamala beach.

2) From the March 2011 Tohoku, Japan tsunami, the tsunami flow velocities on land are estimated from videos by estimating movement distances from reference dimensions measured from known objects or Google Earth or satellite images in Kamaishi City, Ofunato City, Kesennuma City and Iwaki City. The analyzed tsunami flow velocities are about 3 - 5 m/s in Kamaishi City, 2 m/s in Ofunato City, 3 - 6 m/s in Kesennuma City and 1.5 m/s in Iwaki City.

3) The tsunami flow directions in Kamaishi City, Ofunato City and Iwaki City are perpendicular with the shoreline, but the tsunami flow directions of all cases in Kesennuma City are closely parallel with the shoreline. The flow direction on the land in a city depends on many factors, such as building layouts, obstruction and topography.

4) The inundation depth of Cases No.4, 6, 7 and 9 is estimated from the recorded videos. The relationship of tsunami flow velocity and tsunami inundation depth is compared with the proposed velocity with the proposed tsunami velocity estimated from the inundation depth. All analyzed tsunami flow velocities from are less than $1.5\sqrt{gh}$. The analyzed results in Kesennuma City are about $1.0\sqrt{gh}$, which agree well with the results by Fritz et al. (2012).

5) From Figure 3-21, the analyzed and estimated tsunami flow velocities from the past events are mostly in the ranges from $0.7\sqrt{gh}$ to $1.5\sqrt{gh}$. FEMA 55 (2000) suggested that the velocity of the conservative flow for tsunamis is $2.0\sqrt{gh}$. Therefore, in the development of a tsunami fragility curve, the uncertainty of the tsunami flow velocity is considered in the ranges from $0.7\sqrt{gh}$ to $2.0\sqrt{gh}$ as proposed by Matsutomi and Okamoto (2010).

CHAPTER IV
MODELS AND CALIBRATION

4.1 Introduction

This chapter focuses on the model and calibration of a building by using 3-dimensional non-linear static pushover analysis. To analyze the building responses from the building model, the components of building are modeled and calibrated with experimental results. The calibration of building models is performed by 3-dimensional non-linear static pushover analysis using a nonlinear finite element program TDAPIII (ARK Information System, 2008)

4.2 Analytical Model

The building in this study is analyzed by using 3-dimensional non-linear static pushover analysis by a nonlinear finite element program TDAPIII (ARK Information System, 2008). A building model is developed to evaluate the force distribution in each member, the lateral resistance and building damage under tsunami loading. A fiber element is modeled in plastic hinge regions by separately considering behaviors of each material. The building model primarily consists of an unconfined concrete model, a confined concrete model, a longitudinal reinforcement model, a shear spring model and an in-plane masonry infill model.

4.2.1 Material model of reinforced-concrete frame

A 3-dimensional fiber model is used in plastic hinge regions at the ends of beams and columns. The plastic hinge lengths of beams and columns are evaluated by using the equation proposed by Pauley and Priestley (1992) as equation 4-1.

$$L_p = 0.08L + 0.022d_b f_y \tag{4-1}$$

where

L is distance from a critical section to the point of contraflexure (m)
d_b is diameter of longitudinal reinforcement (m)
f_y is yield stress of longitudinal reinforcement (MPa)

The fiber model comprises an unconfined concrete model, a confined concrete model, and a longitudinal reinforcement model. The stress-strain relationship of unconfined concrete is modeled using the equation proposed by Kent and Park (1971) as shown in Figure 2-10. After the peak point, the stress is assumed to be decreased immediately. The stress-strain relationship of confined concrete is modeled using the

equation proposed by Hoshikuma et al. (1997) as shown in Figure 2-13, because the amount of confinement used in the study covers the range of the amount of confinement used in typical columns in Thailand. The stress-strain relationship of the longitudinal reinforcement is modeled using the equation proposed by Menegotto and Pinto (1973) as shown in Figure 2-14. The shear behavior of columns is considered by using a non-linear spring. The equation proposed by Sezen (2002) is used to model a non-linear shear spring behavior as shown in Figure 2-15.

4.2.2 Material model of masonry infill wall

Many researchers found that masonry infill walls in buildings could resist the lateral load significantly. There are several models proposed for masonry infill walls. A horizontal spring model is used in this research because it is a widely accepted model (Mostafaei and Kabeyasawa, 2004, FEMA 306, 1998). The horizontal spring model cannot represent the behavior of forces transferred to frame columns that may cause the shear failure in frame columns. The equations proposed by FEMA 306 (1998) and Mostafaei and Kabeyasawa (2004) are compared in estimating the lateral resisting capacity of infill walls. The test results from Mehrabi et al. (1996) are used for the comparison. Table 4-1 lists three specimens tested under monotonic loading, which are specimens No.3, No.8 and No.9 from the experiments by Mehrabi et al. (1996). All three specimens had the same perimeter frame, but had different masonry types and different vertical loads. As shown in Figure 4-1, the bare frame had 1.537 m high columns and a 2.312 m long beam. The longitudinal reinforcement bars consisted of eight 12-mm-diameter bars in the columns and four 16-mm-diameter bars in the beam. Material properties are given in Table 4-2. Table 4-3 lists the comparison of lateral resisting forces with the calculated forces by the equations proposed by FEMA 306 (1998) and Mostafaei and Kabeyasawa (2004). The equations proposed by Mostafaei and Kabeyasawa (2004) give closer estimates when comparing with the experimental results. Hence, the equations proposed by Mostafaei and Kabeyasawa (2004) are used to calculate the resisting forces in this study. The backbone curve of the masonry infill wall model was also proposed by Mostafaei and Kabeyasawa (2004) as shown in Figure 2-17.

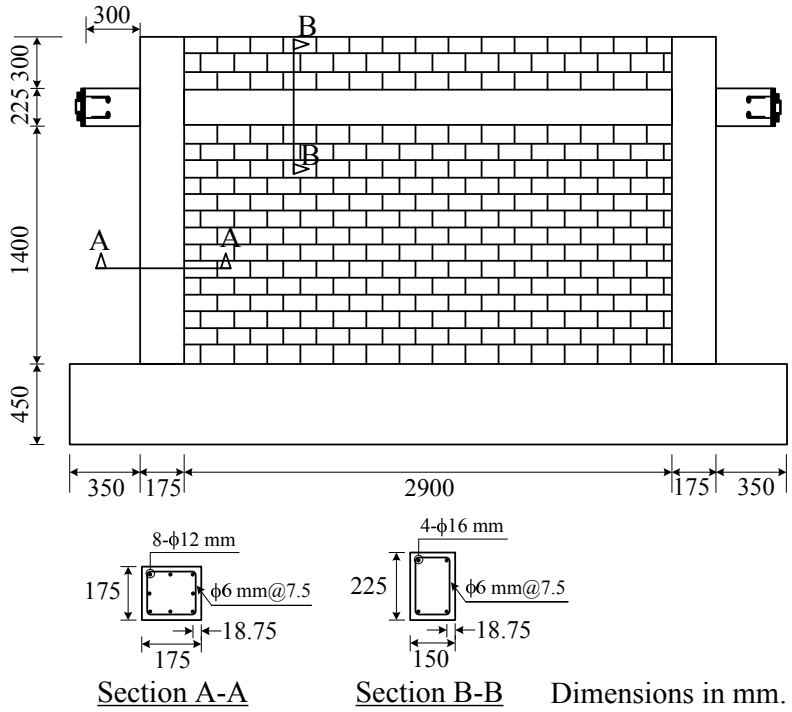

Figure 4-1. Frame dimension and section details from the test by Mehrabi et al. (1996)

Table 4-1. Specimens No. 3, 8 and 9 by Mehrabi et al. (1996)

Specimen	Type of frame	Type of masonry unit	Panel aspect ratio (h/L)	Vertical load distribution (kN)	
				Columns	Beam
No.3	Weak	Solid	0.67	293.7	-
No.8	Weak	Hollow	0.67	195.8	97.9
No.9	Weak	Solid	0.67	195.8	97.9

Table 4-2. Material properties of the tested specimens by Mehrabi et al. (1996)

Compressive of concrete (MPa)	Yield strength of bars (MPa)		
	ϕ16-mm	ϕ12-mm	ϕ6-mm
30.9	414	420	368

Table 4-3. Comparison of lateral resisting force

Specimen	Experiment (1)	Mostafaei and Kabeyasawa (2004) (2)	FEMA 306 (1998) (3)	(2)/(1)	(3)(1)
No.3	28304.5	23845.1	14017.8	0.84	0.50
No.8	19368.6	14975.9	9178.3	0.77	0.47
No.9	29846.7	21898.6	13059.8	0.73	0.44

4.2.3 Analytical models and comparison with experimental results

To validate structural models, experimental results by Wehbe et al. (1999) for RC columns and Anil and Altin (2007) for RC frames are used for comparison with analytical results. The structural parameters of both experiments are listed in Table 4-4. The rectangular reinforced-concrete column with the 380 mm x 610 mm section shown in Figure 4-2(a) was tested under cyclic loading and subjected to an axial force of 615 kN. The columns height was 2.050 m. The longitudinal reinforcement bars of columns consisted of eighteen 19-mm-diameter bars. The transverse reinforcement

was provided by rectangular ties made of 6-mm-diameter bars with two 6-mm-diameter bars crossties and two 10-mm-diameter bars crossties equally spaced at a 110-mm interval along the column height. The material properties of the specimen are listed in Table 4-5.

Table 4-4. Material properties of the tested specimens

Experiment	Span to depth ratio	Longitudinal reinforcement ratio	Volumetric ratio of confinement	Failure mode
Wehbe et al. (1999)	3.828	0.0223	0.0040	Flexure
Anil and Altin (2007)	3.750	0.0209	0.0364	Flexure

Table 4-5. Material properties of the tested specimens by Wehbe et al. (1999)

Compressive of concrete (MPa)	Yield strength of bars (MPa)		
	ϕ19-mm	ϕ10-mm	ϕ6-mm
27.2	445	428	448

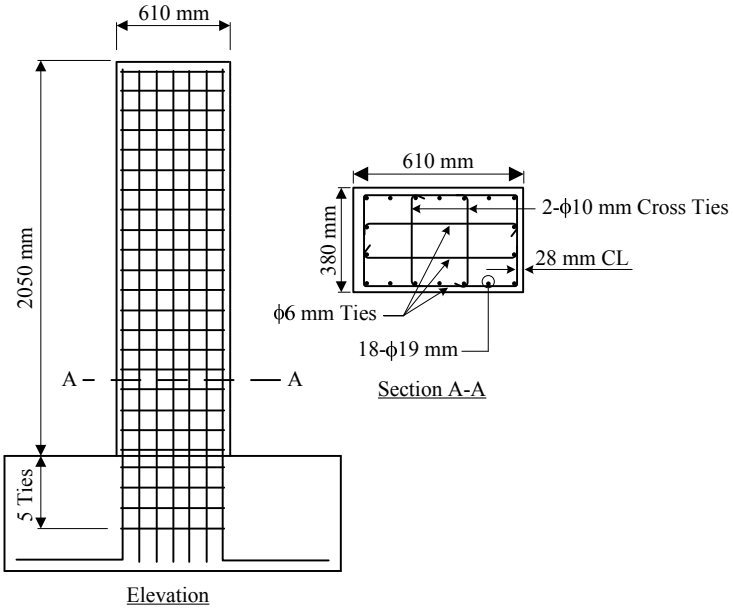

(a) Specimen by Wehbe et al. (1999)

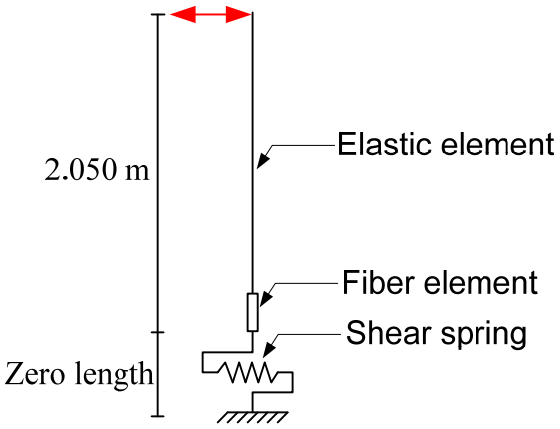

(b) Column model

Figure 4-2. Column for comparison of results

The column model consists of the zero length shear spring, the fiber section element, and the elastic element as shown in Figure 4-2(b). The calculated plastic hinge length of the column is 0.352 m. The comparison between the analytical result and experimental result of this column are shown in Figure 4-3. It is found that the reinforced-concrete column model can capture the actual behaviors satisfactorily. The initial stiffness in the analytical result is slightly higher than the experiment result.

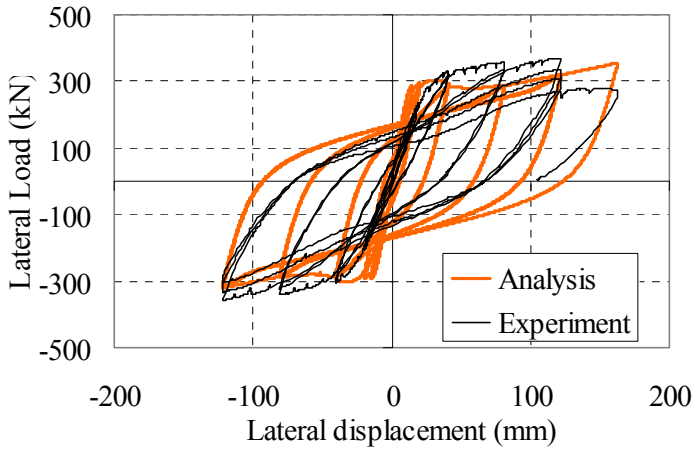

Figure 4-3. Comparison of experimental results by Wehbe et al. (1999) and analytical results

In the study by Anil and Altin (2007), the bare frame with the 100 mm x 150 mm column section and the 150 mm x 300 mm beam section was tested under cyclic loading. As shown in Figure 4-4(a), the bare frame had 750-mm-high columns and a 1,300-mm-long beam. The longitudinal reinforcement bars were four 10-mm-diameter bars in the columns and eight 8-mm-diameter bars in the beam. The transverse reinforcement was 6-mm-diameter bars spaced at 40 mm in the columns near plastic hinge zones and 4-mm-diameter bars spaced at 40 mm in the beam. Material properties of the specimen are listed in Table 4-6. The analytical frame model comprises the zero length shear springs, the fiber elements at the plastic hinges of the columns and the beam, and elastic elements as shown in Figure 4-4(b). The plastic hinge lengths are 0.174 m and 0.150 m for the columns and beam, respectively. The comparison between analytical result and experimental result of this column are shown in Figure 4-5. It is found that the reinforced-concrete column model can capture the actual behaviors satisfactorily.

Table 4-6. Material properties of specimens by Anil and Altin (2007)

Compressive of concrete (MPa)	Yield strength of bars (MPa)				
	ϕ16-mm	ϕ10-mm	ϕ8-mm	ϕ6-mm	ϕ4-mm
21.8	425	475	592	427	326

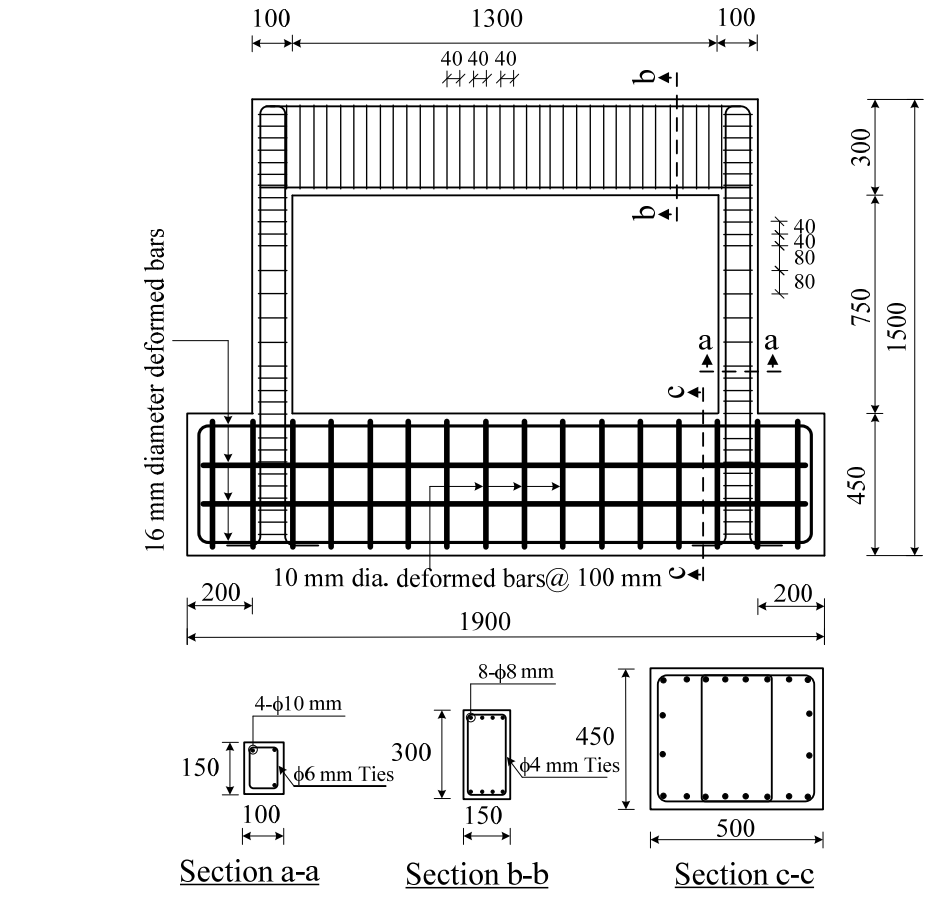

(a) Frame dimensions and reinforcement details in the test by Anil and Altin (2007)

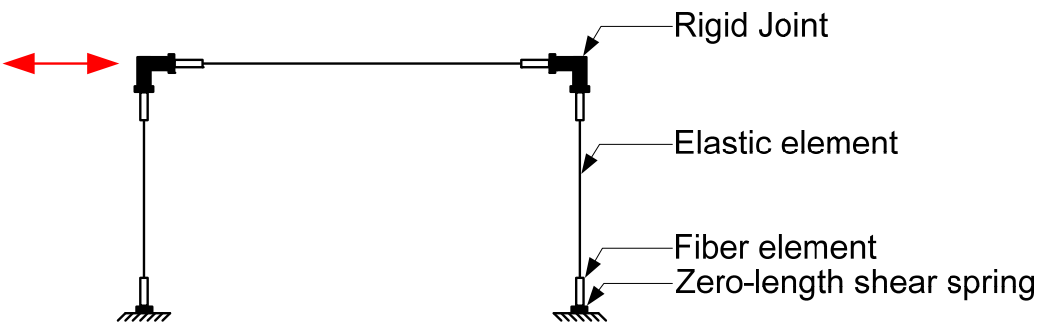

(b) Frame model

Figure 4-4. RC frame for comparison of results

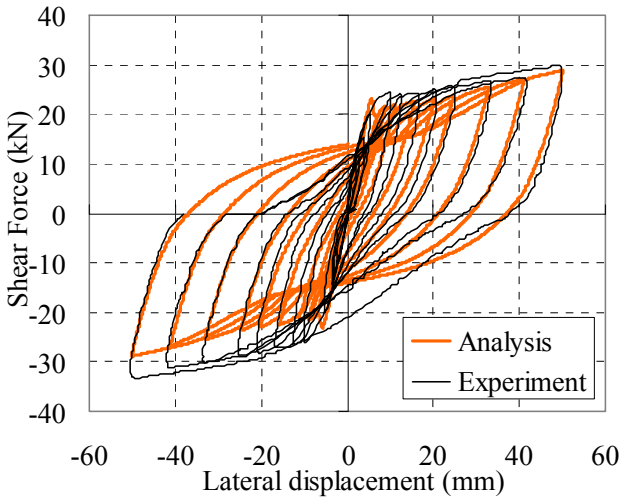

Figure 4-5. Comparison of experimental results by Anil and Altin (2007) and analytical results

The experimental results by Mehrabi et al. (1996) are used to compare with results from analysis of a reinforced-concrete frame with a masonry infill wall. The model is shown in Figure 4-6. The masonry infill wall is modeled as a horizontal spring. The horizontal spring model cannot represent the behavior of forces transferred to frame columns that causes the shear failure in frame columns. The fiber elements are used in the plastic hinge regions at the end of beams and columns. The plastic hinge lengths are 0.174 m for the column and 0.237 m for the beam. Beam-column joints are treated to be rigid. The comparison of the lateral load and lateral displacement relationship between the experimental results and analytical results is shown in Figure 4-7. It is found that the model can predict the maximum load well. The curve from the analysis has the same trend as that from the test.

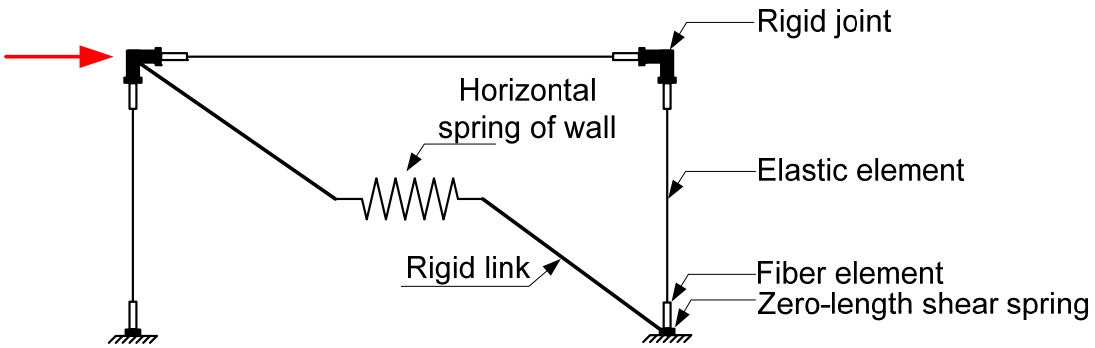

Figure 4-6. Analytical model of the RC frame with an infill wall

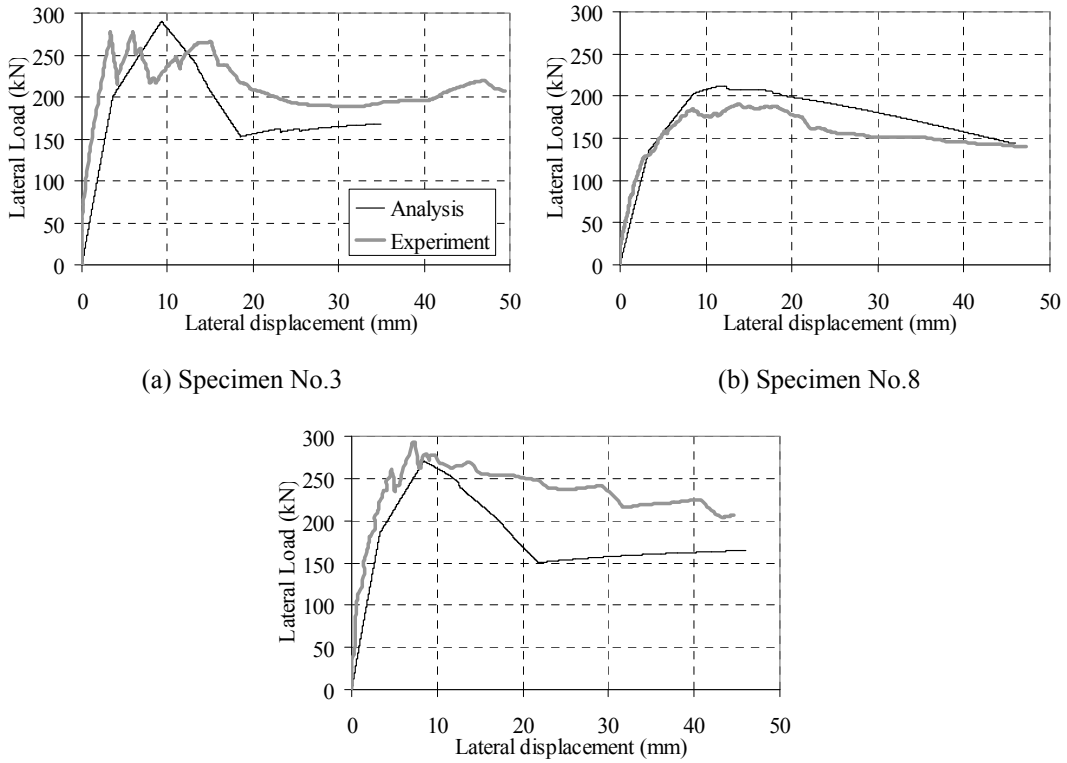

(a) Specimen No.3

(b) Specimen No.8

(c) Specimen No.9

Figure 4-7. Comparison between experimental results by Mehrabi et al. (1996) and analytical results

4.3 Experiment on RC Building under Tsunami Load Pattern

4.3.1 Building configuration and experimental results

Figure 4-8 shows the former office of Thai Meteorological Department located in Phang-Nga province tested by Lukkunaprasit et al. (2010). This building was estimated to be exposed to a tsunami inundation depth of 4.4 m. The building was damaged mainly in non-structural members especially brick walls. Hairline cracks were observed in columns. The beam and column plan of the building is illustrated in Figure 4-9. Figure 4-10 shows the masonry infill walls for the frames in Grids A, B and C referred to as Frames A, B and C, respectively. There is no masonry infill wall on the first floor in Frame A. For Frame B, there is the masonry infill wall at the front span. For Frame C, there are walls under window panels. The compressive strength of cored concrete samples was 12 MPa, and the specified yield strength of reinforcement was 240 MPa. Figure 4-11(a) depicts the pushover test setup. The lateral pushover force was applied by the hydraulic jacks at six beam-column joints at the building front to represent the hydrodynamic force due to the tsunami. Figure 4-11(b) shows the relationship of the lateral force and displacement of each frame. The building was

loaded up to 381 kN until large cracks were observed in the wall in Frame B. The maximum roof displacement was 14 mm.

Figure 4-8. The former office of Thai Meteorological Department in Phang-Nga (Lukkunaprasit et al., 2010)

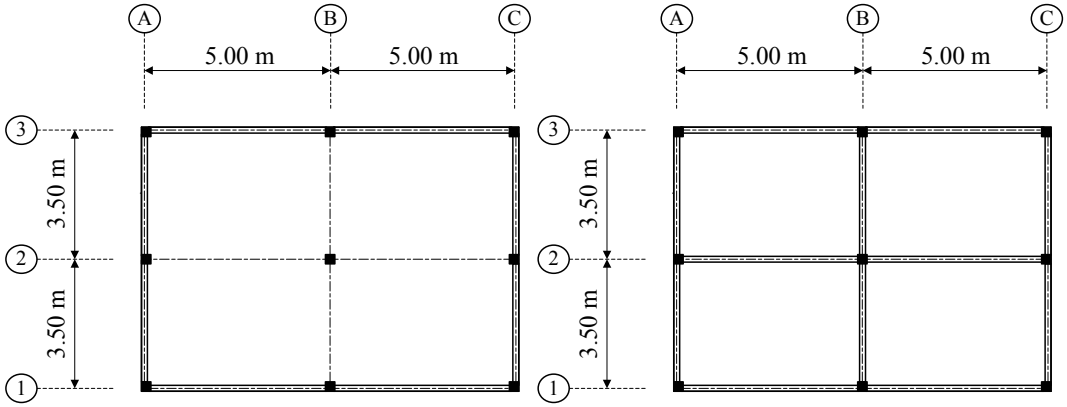

(a) Ground floor plan (b) 1st floor plan

Figure 4-9. Plan of the former office of Thai Meteorological Department

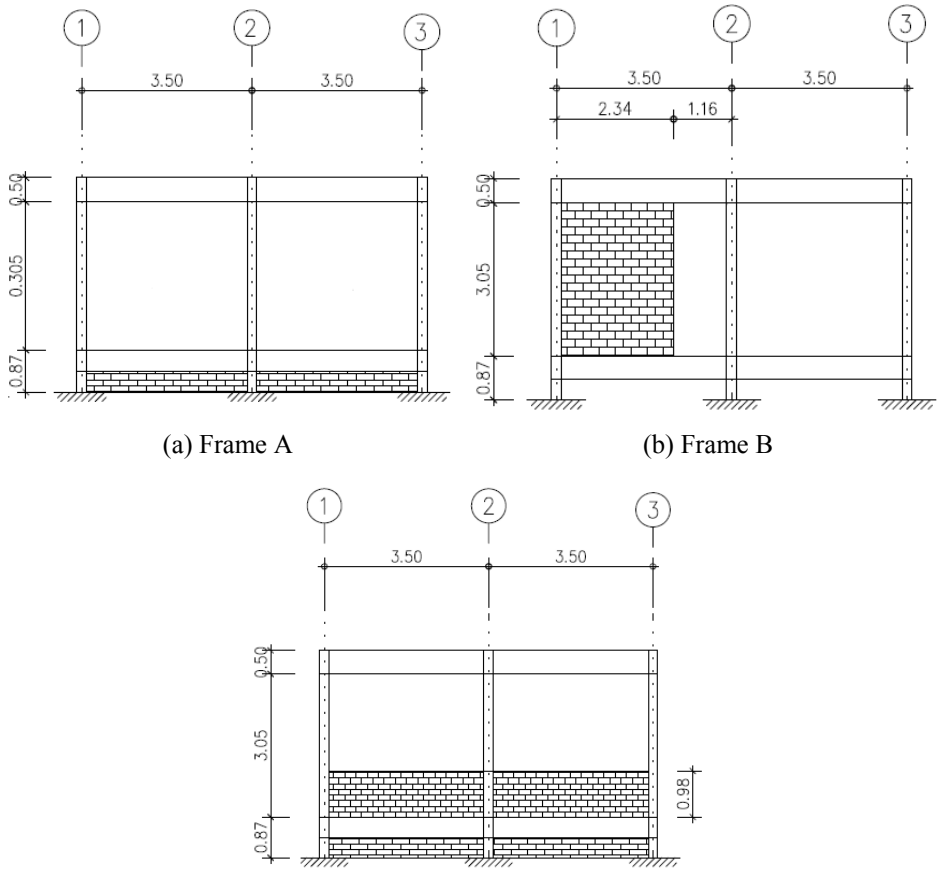

(a) Frame A (b) Frame B

(c) Frame C

Figure 4-10. Location of masonry infill wall of each frame

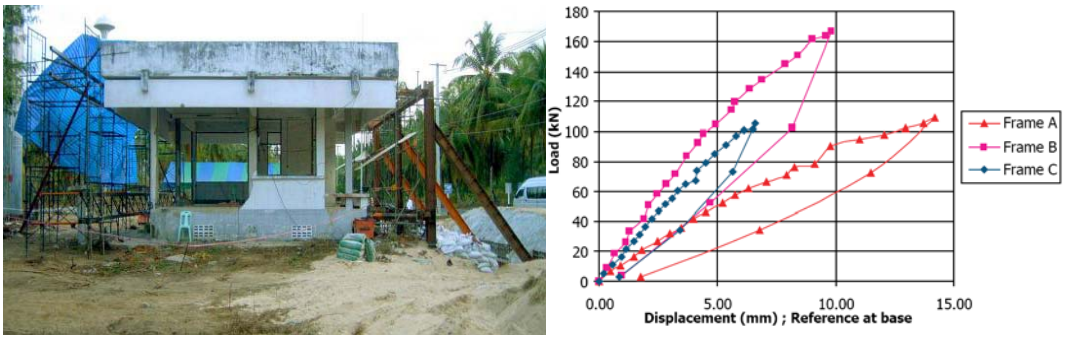

(a) Test setup (b) Lateral force vs displacement relation

Figure 4-11. Pushover test setup and results (Lukkunaprasit et al., 2010)

4.3.2 Behavior of masonry infill

In this study, masonry specimens were collected from the tested building to determine the compressive strength of the masonry prism. The compressive test method of the masonry prism was carried out according to ASTM C 1314-03b (2003). The test setup of the masonry prism is shown in Figure 4-12(a), and the stress-strain relationship of the masonry prism is shown in Figure 4-12(b). The maximum compressive stress is 6.36 MPa.

Figure 4-13 shows cracks on the wall in Frame B at the initial state, maximum lateral load and unloading. The crack width in mm is also shown in the figure. Cracks on the wall in Frame B significantly widened at the maximum lateral load.

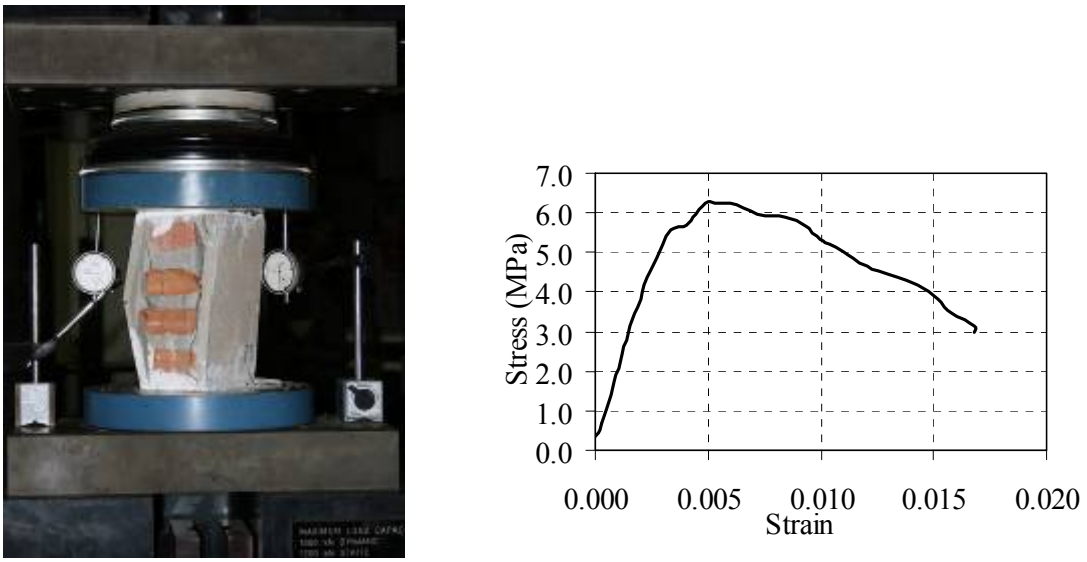

(a) Experiment setup (b) Stress-strain relationship

Figure 4-12. Experiment setup and stress-strain relationship of the masonry prism

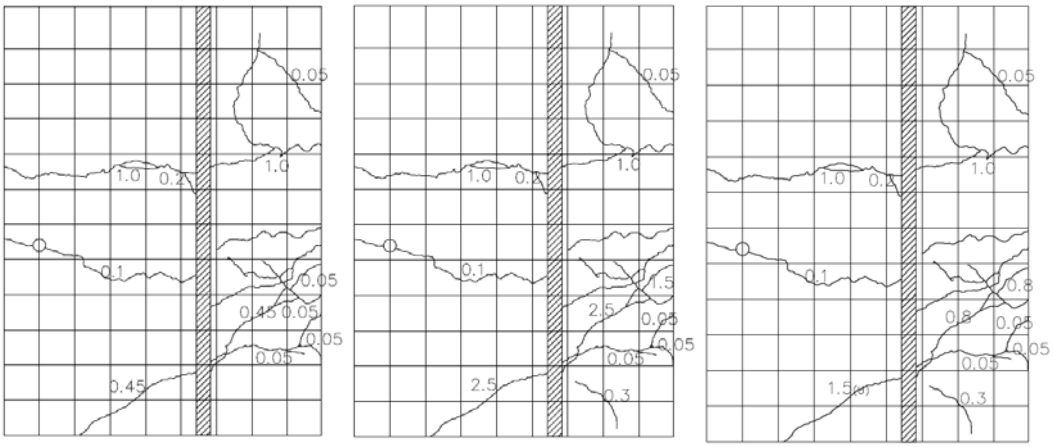

(a) Initial (b) Maximum load (c) Unloading

Figure 4-13. Cracks on the masonry infill wall in Frame B

4.4 Correlation Analysis of RC Building Subjected to Tsunami Loads

4.4.1 Behavior of masonry infill

The building model of the former office of Thai Meteorological Department located in Phang-Nga province is developed using the models presented in the previous section. Since the value of the span to depth ratio of the columns on the first floor is large, the flexural failure of columns is expected. So, shear springs are omitted in the model. However, shear springs are included for the short columns under the

first floor. The building model is analyzed by using 3-dimensional non-linear static pushover analysis under force-controlled. The masonry infill wall is modeled as a horizontal spring. The horizontal spring model cannot represent the behavior of forces transferred to frame columns that causes the shear failure in frame columns. As shown in Figure 4-14, six point loads, which are three point loads at the roof level and three point loads at the first floor level, act on the building at the same locations as the loading points in the field load test.

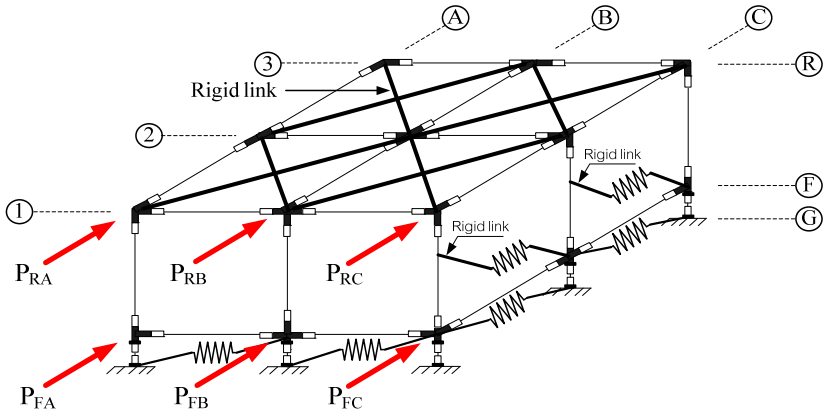

(a) 3-dimensional model of the building

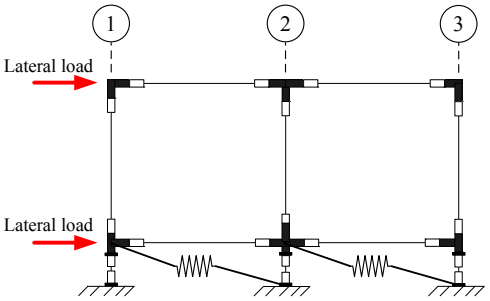

(b) Frame A

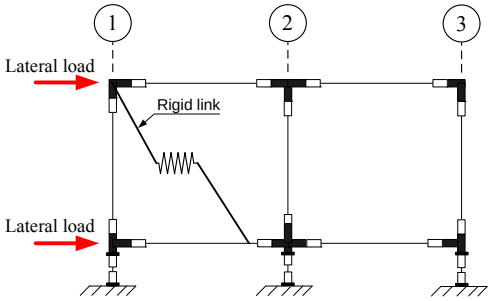

(c) Frame B

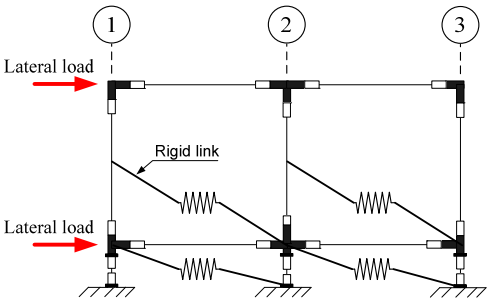

(d) Frame C

Figure 4-14. Analytical model

In the analytical model, the fiber elements are used in plastic hinge regions at the end of beams and columns. According to the equation proposed by Pauley and Priestley (1992), the plastic hinge length of columns is 0.185 m, and the plastic hinge

length of beams is 0.224 m. The masonry infill walls are modeled as a horizontal spring. The horizontal spring model cannot represent the behavior of forces transferred to frame columns that causes the shear failure in frame columns. Beam-column joints are assumed to be rigid, and floor slabs are assumed as rigid diaphragms.

4.4.2 Comparison of experimental and analytical results

The comparison of lateral load vs lateral displacement relationship for each frame is shown in Figure 4-15. From the figure, it can be seen that the analytical model can capture the initial stiffness well. However, the lateral displacement from the analysis is slightly larger after **Point a** at a load of about 250 kN. Displacements in the analysis exceed displacements in the experiment because the masonry infill wall in Frame B reaches the lateral yielding force of the wall at **Point a** as shown in Figure 4-16. At the peak load, the masonry infill wall in Frame B reaches the maximum capacity. In the experiment, it was found that cracks on the masonry infill wall in Frame B significantly widened at the maximum lateral load. The maximum force occurring in short columns under the first floor is 43.7 kN, which is less than the shear capacity of 77.9 kN. Hence, there is no shear failure of the short columns. The maximum loads at the roof level are 21.2 kN, 136.7 kN and 26.8 kN for Frame A, Frame B and Frame C, respectively, as shown in Figure 4-17. Frame B shares the majority of the roof load due to the presence of the infill wall. Figure 4-18 shows the comparison of the roof displacements. The rotation angles of the building roof agree well with experimental results. However, the roof displacement from the analysis is larger at the maximum load as discussed above. Figure 4-19 shows the lateral displacement profile of each frame. The displacements at the first floor are small because of the presence of walls and short columns at the ground level. The displacements at the roof level are significantly larger due to a small amount of walls on the first floor. It is obvious that deformation mainly occurs in the first floor columns and walls.

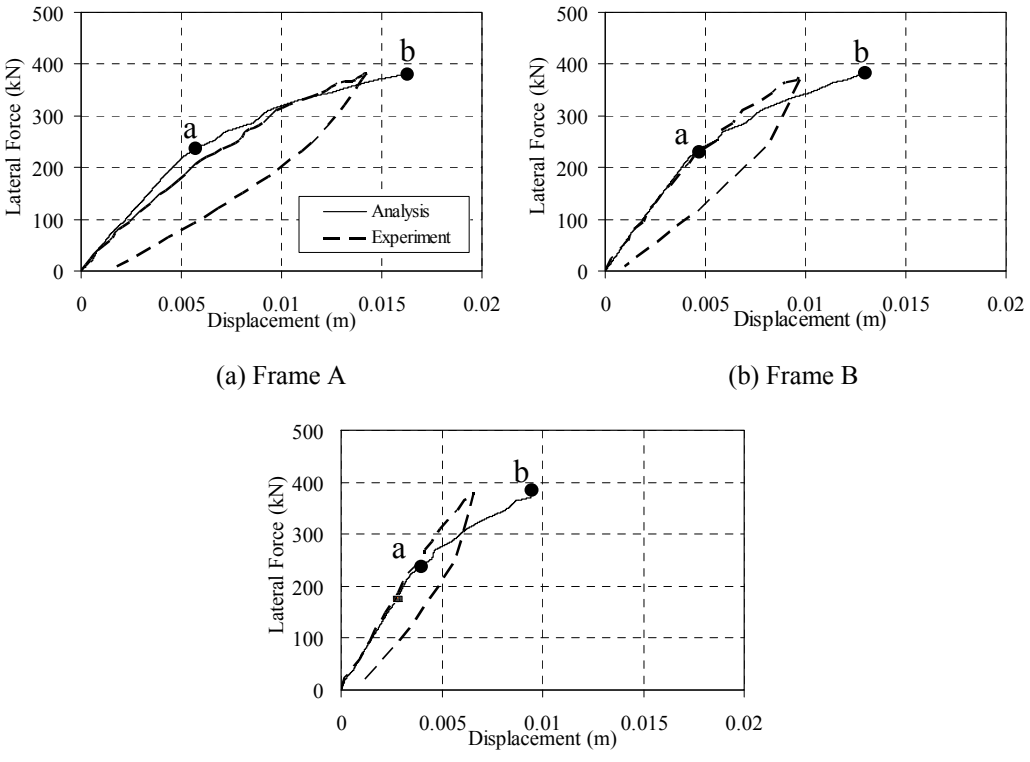

(a) Frame A (b) Frame B

(c) Frame C

Figure 4-15. Comparison of lateral force and displacement relationships

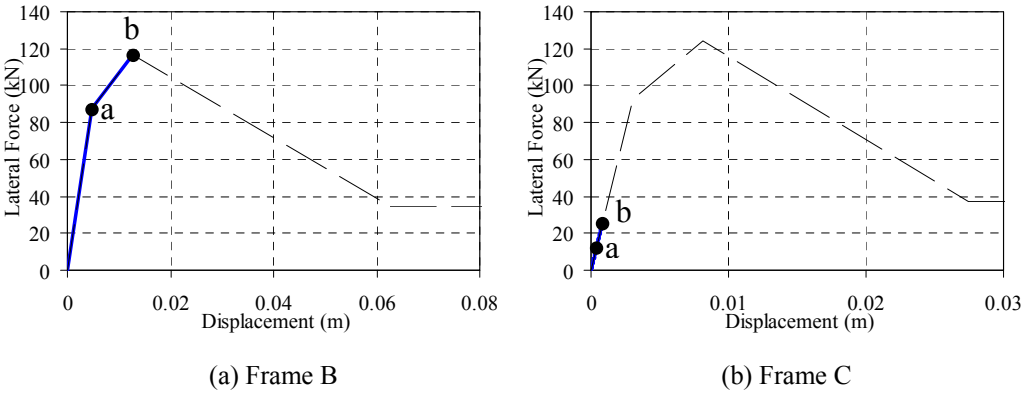

(a) Frame B (b) Frame C

Figure 4-16. Force and deformation relationship of the masonry infill wall

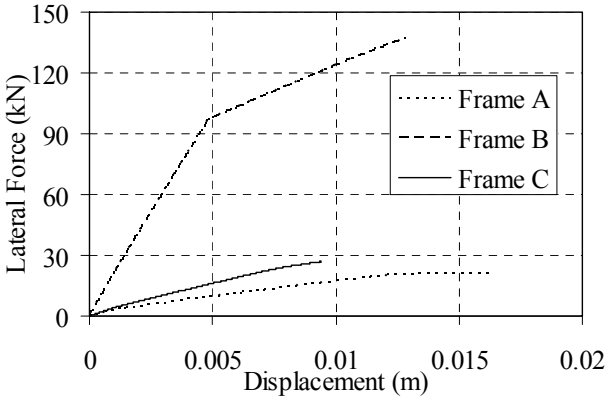

Figure 4-17. Load at the roof level carried by each frame

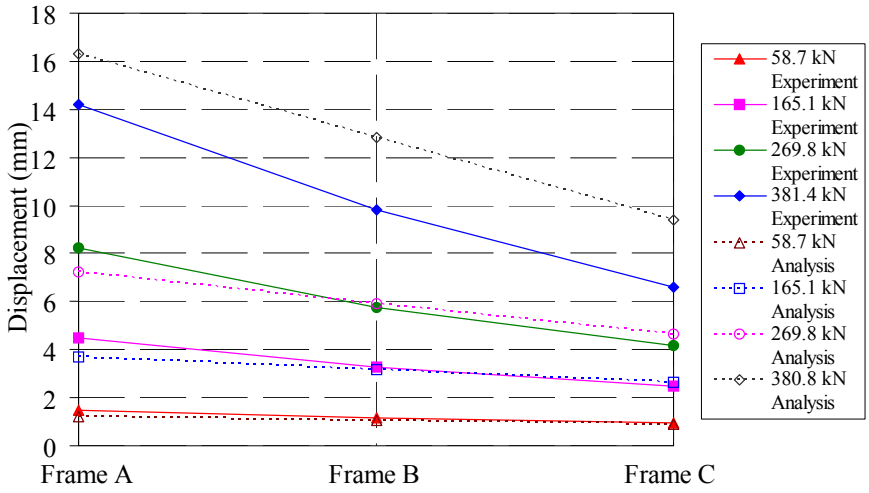

Figure 4-18. Comparison of the roof displacements

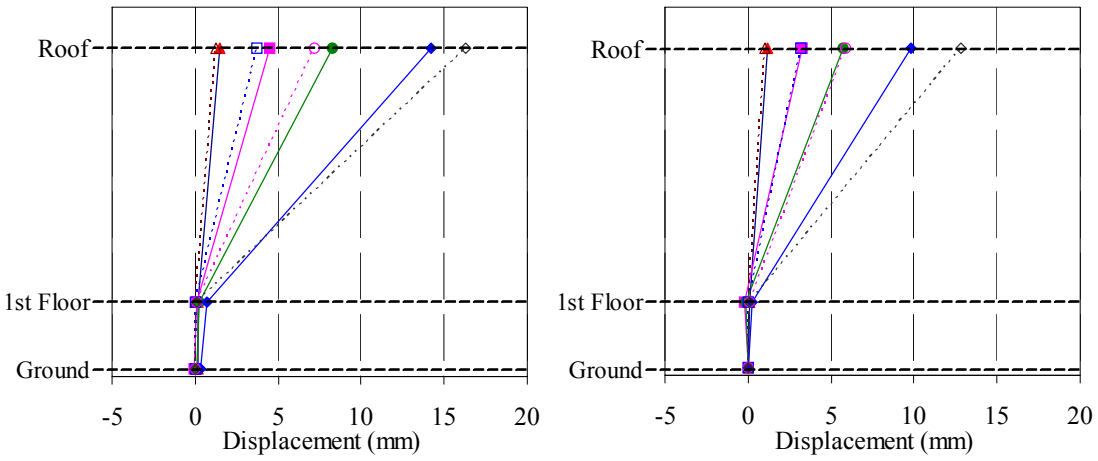

(a) Frame A

(b) Frame B

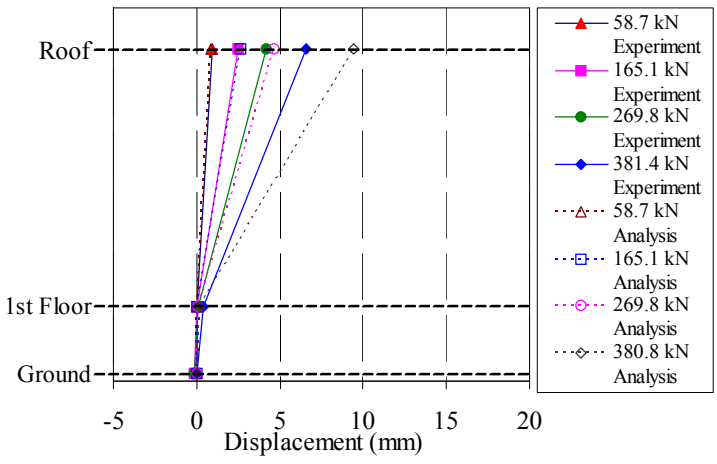

(c) Frame C

Figure 4-19. Comparison of the lateral displacement profile for each frame

CHAPTER V
BUILDING FOR ANALYSIS

5.1 Introduction

This chapter presents the generic building which is used to develop a tsunami fragility curve and to analyze building responses under tsunami loading. Calculated structural indices are described. The one-story generic building is developed from the average values of calculated structural indices.

5.2 Collected Building Details

The December 26th, 2004 Indian Ocean tsunami caused damage to buildings in Indian Ocean countries. 6 provinces in Thailand suffered damage. The damage of buildings was collected in the damage database (CEEEV, 2005 : online). From the damage database, 52% of one-story buildings damaged in columns or beams, and 19% of them collapsed. For buildings taller than one-story, there is no data on collapse, and about 13% of them damaged in columns or beams. It can be seen that one-story buildings suffered more serious damage than buildings taller than one-story. To analyze the behaviors of a one-story RC building under tsunami loading, construction drawings in Phuket province, Thailand are collected. Five construction drawings of a one-story building are selected. The selected construction drawings are general building types which are widely constructed in the Southern part of Thailand. Building data consisted of name, occupancy, Hazus occupancy and locations are listed in Table 5-1.

Table 5-1. Construction drawings of one-story reinforced-concrete building in Phuket province, Thailand

No	Name	Occupancy	Hazus Occupancy	Location
1	2 units one-story house	Residence	RES3A	Kamala
2	One-stories house	Residence	RES1	Cherngtaley
3	4 units one-story house	Apartment	RES3B	-
4	One-story house	Residence	RES1	-
5	One-story house	Residence	RES1	Kamala

Remark RES1 is a single family dwelling,
RES3A is a 2 unit families dwelling,
RES3B is a 3-4 unit families dwelling

5.3 Structural Indices

The generic buildings are developed based on structural indices to develop the analytical tsunami fragility curve and analyze building responses under tsunami loading. The structural indices are calculated from construction drawings. The structural indices used to develop the generic building are floor area, column size, longitudinal reinforcement diameter, stirrups diameter, the compressive strength of concrete, the yield strength of longitudinal reinforcement, the yield strength of stirrups, the ratio of width to length of a building (B/L), the aspect ratio (a/d) (where a, is the distance from maximum moment to point of inflection, d is the distance from the top of section to centroid of the tension reinforcement), the ratio of the in-plane masonry infill wall area to floor area (A_{Inf}/A_{floor}), the axial load ratio ($P/f_c'A_g$) (where P is the axial load, f_c' is the compressive strength of concrete, A_g is the gross section area of column), the reinforcement ratio ($\rho = A_s/b_w d$) (where A_s section area of longitudinal reinforcement, b_w is the width of column section), the volumetric ratio ($\rho_s = V_{stirrup}/V_{core}$) (where $V_{stirrup}$ is the volume of transverse reinforcement, V_{core} is the volume of confined concrete), the shear strength ratio ($\alpha = M_n/aV_n$) (where M_n is the nominal moment, V_n is shear capacity and a is a shear span) and the percentage of wall opening. The shear strength ratio ($\alpha = M_n/aV_n$) is the ratio of the shear force when the member reaches its flexural capacity divided by shear capacity. The calculated and the averaged structural indices are listed in Table 5-2 and Figure 5-1.

Table 5-2. Structural indices from construction drawings

Structural Index	No. of Construction Drawing					Average
	1	2	3	4	5	
Floor Area (m2)	91.8	63.0	144.0	114.0	52.5	93.1
Column (cm xcm)	20x20	15x15	15x15	20x20	20x20	18x18
Longitudinal Reinforcement Diameter (mm)	12	12	12	12	12	12
Stirrups Diameter (mm)	6	6	6	6	6	6
Compressive Strength of Concrete (MPa)	23.5	23.5	23.5	23.5	23.5	23.5
Yield Strength of Longitudinal Reinforcement (MPa)	294	294	294	294	294	294
Yield Strength of Stirrups (MPa)	235	235	235	235	235	235
Width to Length Ratio	0.88	0.32	1.78	1.56	0.78	1.06
Aspect Ratio (a/d)	9.20	14.16	13.05	9.20	7.36	10.60
Wall Area to Floor Area Ratio	0.95	1.42	0.82	0.71	0.75	0.95
Axial Load Ratio (P/f'_cA_g)	0.0086	0.0201	0.0212	0.0302	0.0169	0.0190
Reinforcement Ratio (ρ)	0.0139	0.0267	0.0267	0.0139	0.0139	0.019
Volumetric Ratio (ρ_s)	0.0038	0.0075	0.0057	0.0050	0.0038	0.0052
Shear Strength Ratio ($\alpha = M_n / aV_n$)	0.45	0.41	0.53	0.40	0.52	0.46
Percentage of Front Opening	36.0	29.9	26.6	40.7	16.9	30.0
Percentage of Left Opening	16.2	0.0	0.0	1.1	18.4	7.1
Percentage of Right Opening	16.2	0.0	0.0	1.1	15.7	6.6
Percentage of Back Opening	36.0	27.2	18.4	15.7	6.7	20.8

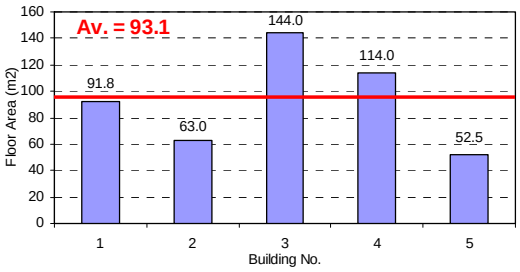

(a) Floor area

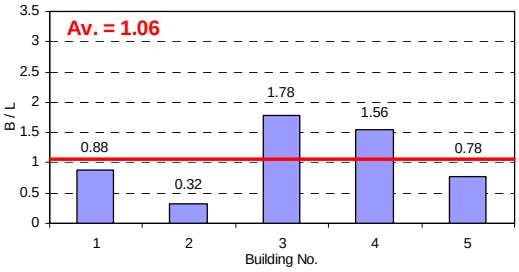

(b) Width to depth of building ratio

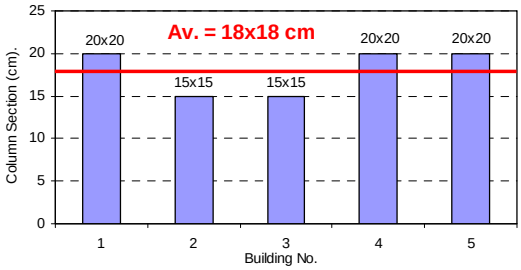

(c) Column section

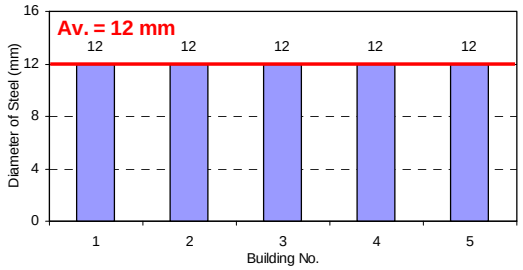

(d) Diameter of longitudinal reinforcement

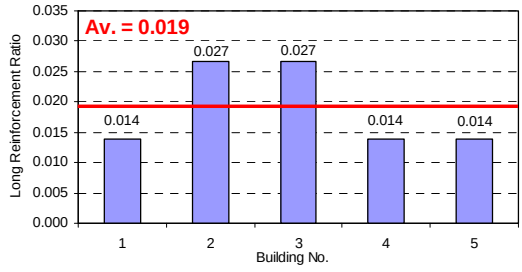

(e) Longitudinal reinforcement ratio

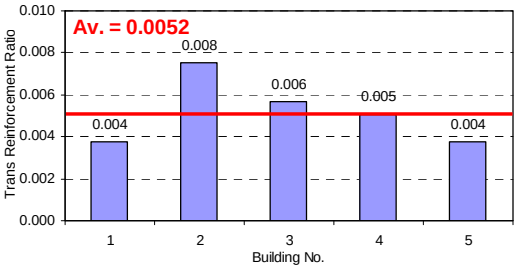

(f) Transverse reinforcement ratio

Figure 5-1. Structural index of construction drawings

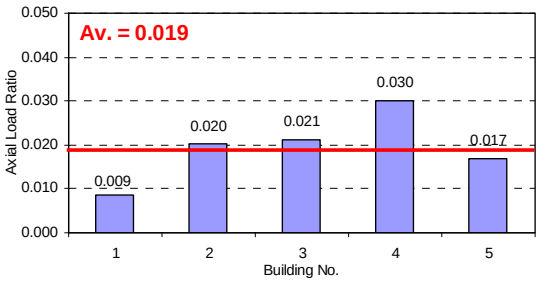

(g) Axial ratio

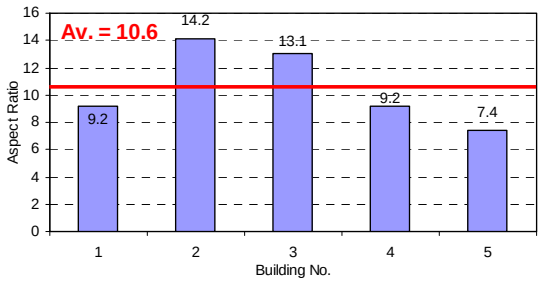

(h) Aspect ratio

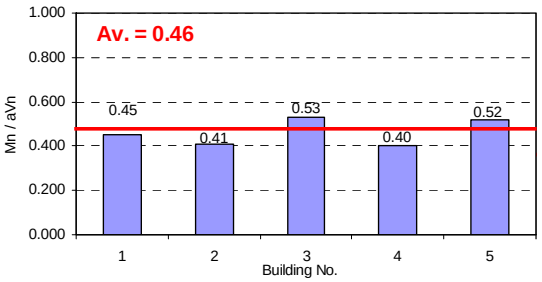

(i) Shear strength ratio

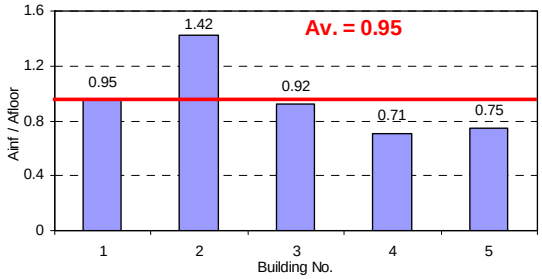

(j) Wall area to floor area ratio

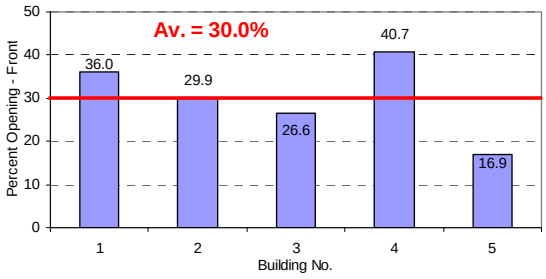

(k) Front Opening Percentage

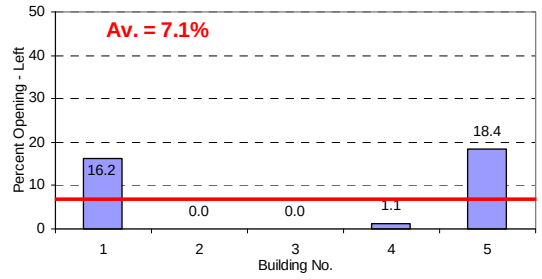

(l) Left Opening Percentage

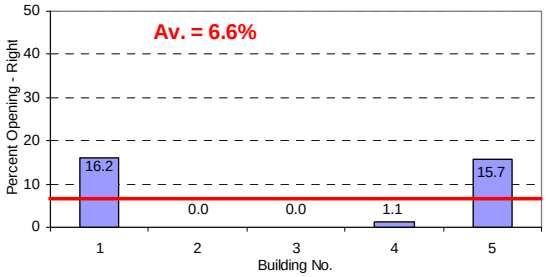

(m) Right Opening Percentage

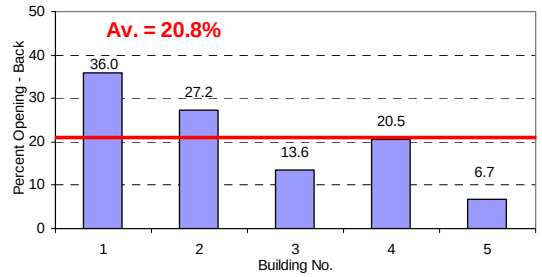

(n) Back Opening Percentage

Figure 5-1. (continued) Structural index of construction drawings

The compressive strength of concrete is 23.5 MPa. The yield strength of longitudinal reinforcement and stirrups are 294 MPa and 235 MPa, respectively. The average ratio of width to length of buildings is 1.06. The average aspect ratio is 10.6. The average ratio of the in-plane wall area to floor area is about 1.0. The average axial load ratio is quite low at 0.019 because of no roof floor. Column sections are lightly reinforced. The average values of the reinforcement ratio and volumetric ratio are

0.019 and 0.005, respectively. The shear strength ratio of all buildings is less than 1.0. It means that the building may fail in the flexure mode. The average value of shear strength ratios is 0.46.

5.4 Development of Generic Building

A generic one-story building is developed from the average values of collected buildings. The building parameters are as following.

1) Column section and reinforcement

From Table 5-2, the average column section is 18 cm x 18 cm, but this section is not a practical section. The column section of the generic building is 20 cm x 20 cm. The longitudinal reinforcement is 4-DB12mm, and stirrups are RB6@150mm. Then, the reinforcement ratio is 0.0139, and the volumetric ratio is 0.0050.

2) Dimension of building

The average floor area is 93.1 m^2, and the average width to length ratio is 1.06. Therefore, the width and length of the generic building are 10 m, and 9 m, respectively. The floor area is 90 m^2 and the width to length ratio is 1.11. The selected column height for generic building is 3.0 m with the aspect ratio of 9.2.

3) Material properties

From construction drawings, the average value of compressive strength is 23.5 Mpa. The average values of yield strength of reinforcement and stirrups are 294 MPa and 234 MPa, respectively. The compressive strength of concrete and yield strength of stirrups are used the same as the average strength of construction drawings. The yield strength of reinforcement of 294 MPa is not a general practice nowadays. The specified yield strength is 392 MPa.

From the selected building parameters for the generic building, the axial load of a column is about 26.76 kN. The axial load ratio of a column is 0.028. The yielding moment of columns is 8.1 kN-m. The shear capacity of columns is 24.30 kN. The shear strength ratio is 0.25 which is controlled by the flexural failure. The comparison of calculated structural indices from construction drawings and the generic building is listed in Table 5-3. A roof beam section is designed directly to carry out its self weight. The roof beam section is 20 cm x 40 cm with the longitudinal reinforcement of 5-DB16mm and stirrups RB6@150mm. The ground plan and roof plan of the

generic building are shown in Figure 5-2. The front view and side view are shown in Figure 5-3. Roof beam and column sections are shown in Figure 5-4.

Table 5-3. Structural indices from construction drawings and generic building

Structural Index	Average Index of Construction Drawings	Generic Building
Floor Area (m2)	93.1	90.0
Column (cm x cm)	18 x 18	20 x 20
Longitudinal Reinforcement Diameter (mm)	12	12
Stirrups Diameter (mm)	6	6
Compressive Strength of Concrete (MPa)	23.5	23.5
Yield Strength of Longitudinal Reinforcement (MPa)	294	392
Yield Strength of Stirrups (MPa)	234	234
Width to Length Ratio	1.06	1.11
Aspect Ratio (a/d)	10.60	9.2
Axial Load Ratio ($P/f_c'A_g$)	0.019	0.028
Reinforcement Ratio (ρ)	0.019	0.0139
Volumetric Ratio (ρ_s)	0.0052	0.0050
Shear Strength Ratio ($\alpha = M_n / aV_n$)	0.38	0.22

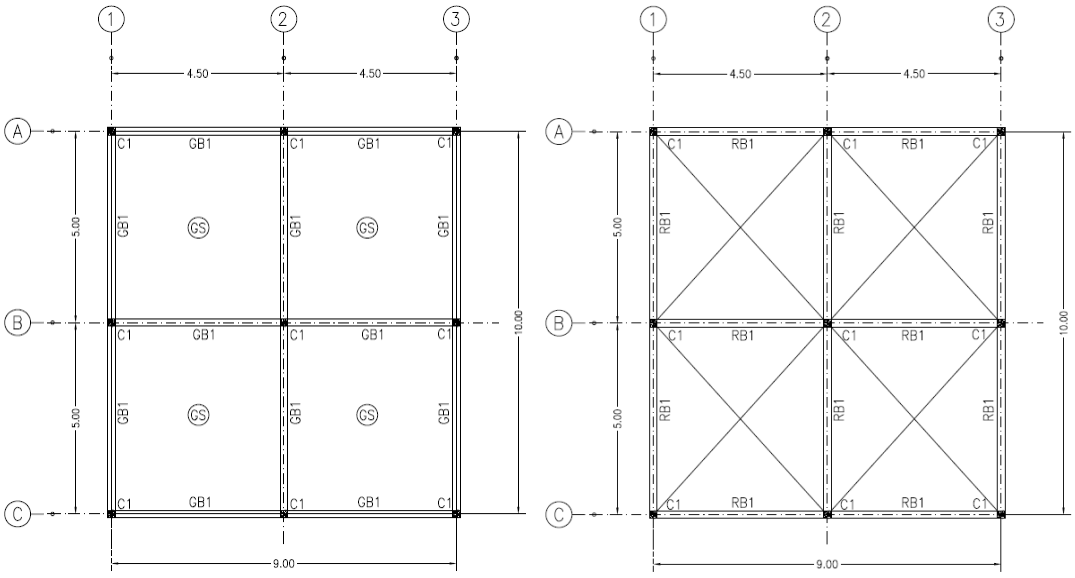

(a) Ground plan (b) Roof plan

Figure 5-2. Plan of generic building

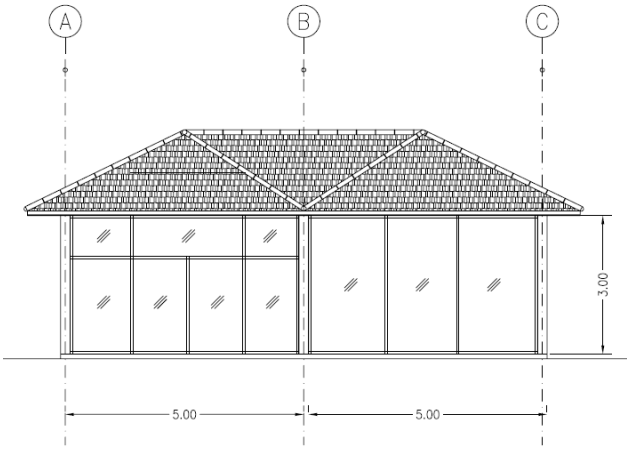

(a) Front view

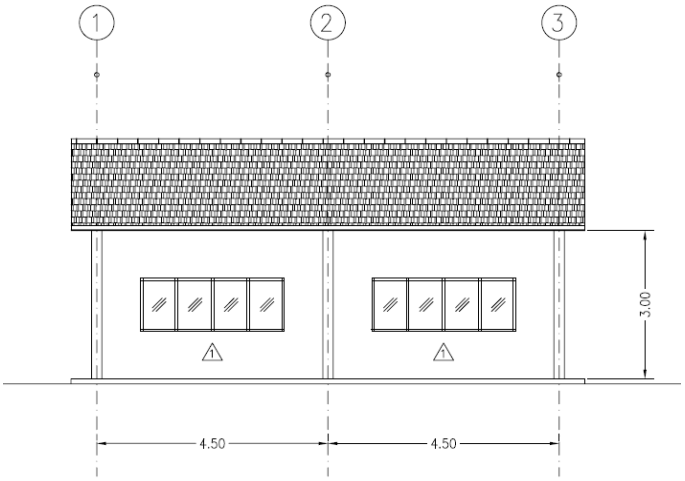

(b) Side view

Figure 5-3. Front view and side view of generic building

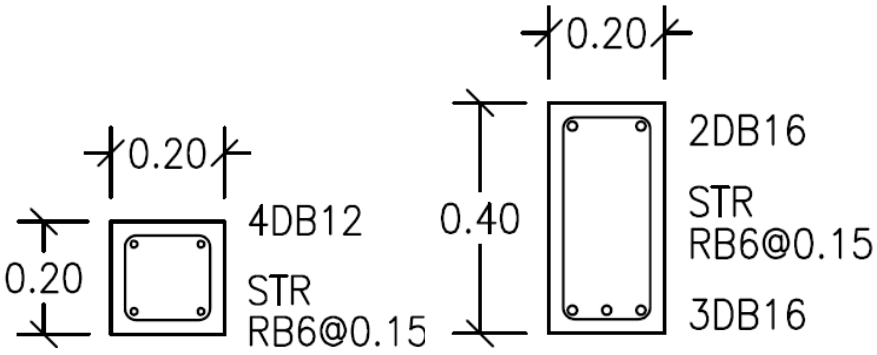

(a) Column section (b) Roof beam section

Figure 5-4. Column and roof beam sections of generic building

CHAPTER VI
BUILDING RESPONSE UNDER TSUNAMI LOADING

6.1 Tsunami Load

A building under the tsunami loading may experience a hydrostatic force, a hydrodynamic force, a buoyancy force, a breaking wave force and a debris impact force, when tsunami flow through the building. The hydrostatic force is the lateral force acting on a building when water is standing or slowly moving. The hydrodynamic force is the uniform lateral force acting on a building due to a flow velocity. The hydrodynamic force consists of the force on the upstream, drag force along the sides and suction force on the downstream side of a building. The buoyancy force is the uplift force. The breaking wave force is the force acting on the building when the wave is breaking in off-shore. The debris impact force is the force due to debris colliding the building.

There are several researchers and design guideline codes who proposed the formulas used to estimate tsunami forces (Ramsden and Raichlen, 1990, Ramsden, 1996, Hamzah et al., 2000, Asakura et al., 2002, Okada et al., 2005, FEMA 55, 2000, CCH, 2000, FEMA P646, 2008). Yeh (2007) suggested that, the hydrodynamic force should be considered to calculate force acting on onshore buildings. Additionally, Lukkunaprasit et al. (2009) found that calculated hydrodynamic forces agreed well with their experimental results. Therefore, the hydrodynamic force is considered in this study.

The hydrodynamic force is considered as a uniform lateral force through the depth. The tsunami flow velocity is increased until collapse by using the force-controlled method. The considered tsunami inundation depths are 0.24 m, 0.4 m, 0.6 m, 0.8 m, 1.0 m, 1.2 m, 1.4 m, 1.6 m, 1.8 m, 2.0 m, 2.2 m, 2.4 m, 2.57 m, 2.8 m 3.0 m and 3.2 m.

6.2 Building Model

The building is analyzed by using 3-dimensional non-linear static pushover analysis by a nonlinear finite element program TDAPIII (ARK Information System 2008). A building model is developed to evaluate force distribution in each member,

the lateral resistance and damage of the building under tsunami loading. The fiber model is used to model plastic hinges by separately considering the behavior of each material. The building model primarily consists of unconfined concrete models, confined concrete models, longitudinal reinforcement models and shear spring models.

6.2.1 Material properties

From the generic building, the compressive strength is 23.5 Mpa. The yield strength of longitudinal reinforcement with a diameter of 12 mm and 16 mm is 392 MPa and the yield strength of stirrups with a diameter of 6 mm is 235 MPa. The compressive strength has an uncertainty due to the production of the concrete batch and measured strength in the testing process (ACI-214R, 2002). The yield strengths of longitudinal reinforcements and stirrups are obtained by the tensile testing of the sampled reinforcements from local companies. There are three samples for the reinforcement with a diameter of 6 mm and 16 mm, and there are two samples for the reinforcement with a diameter of 12 mm. The stress and strain relationships of the reinforcement tensile testing are shown in Appendix A. The tensile testing results of the reinforcement are listed in Table 6-1. The yield strengths of reinforcement with a diameter of 6 mm, 12 mm and 16 mm are 319 MPa, 451 MPa and 549 MPa, respectively.

Table 6-1. Tensile strength of reinforcement from testing

Diameter (mm)	Grade	Yield strength (MPa)	Yield strain	Elastic modulus (GPa)	Strain hardening
ϕ6-mm	SR24	319	0.00365	224	0.01020
ϕ12-mm	SD40	451	0.00240	203	0.00722
ϕ16-mm	SD40	549	0.00330	209	0.00942

6.2.2 Material models

A 3-dimensional fiber model is used in plastic hinge regions at ends of beams and columns. The plastic hinge lengths of beams and columns are evaluated by using the equation proposed by Pauley and Priestley (1992) as equation 4-1. The fiber model comprises an unconfined concrete model, a confined concrete model, and a longitudinal reinforcement model. The fiber sections of columns and beams are shown in Figure 6-1. The plastic hinge length of column is 0.24 m. The plastic hinge lengths of beams are 0.356 m and 0.385 m for the span lengths of 4.5 m and 5.0 m, respectively.

The stress-strain relationship of unconfined concrete is modeled using the equation proposed by Kent and Park (1971) as shown in Figure 2-10. After the peak point, the stress is assumed to be decreased immediately. The stress-strain relationship of confined concrete is modeled using the equation proposed by Hoshikuma et al. (1997) as shown in Figure 2-13, because the amount of confinement used in the study covers the range of the amount of confinement used in typical columns in Thailand. The calculation parameters of concrete used in the analysis are listed in Table 6-2. The stress-strain relationship of the longitudinal reinforcement is modeled using the equation proposed by Menegotto and Pinto (1973) as shown in Figure 2-14. The shear behavior of columns is considered by using a non-linear spring. The equation proposed by Sezen (2002) is used to model a non-linear shear spring behavior as shown in Figure 2-15. The axial load, shear capacity and moment capacity of columns are listed in Table 6-3.

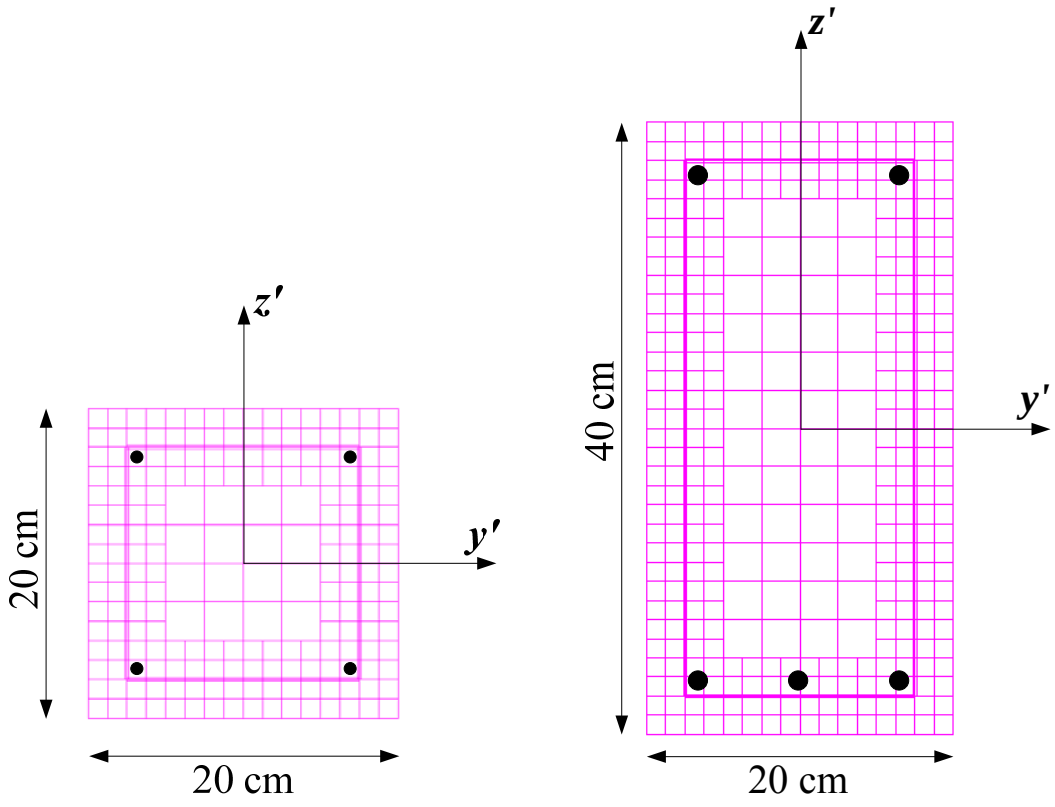

(a) Column (b) Beam

Figure 6-1. Fiber section of columns and beams

Table 6-2. Calculation parameters used in analysis of core concrete

Element	Elastic Modulus (GPa)	Concrete Covering		Concrete Core	
		Strength (MPa)	Strain	Strength (MPa)	Strain
Beam	22.8	23.5	0.0020	24.4	0.00264
Column		23.5	0.0020	24.8	0.00290

Table 6-3. Axial load, shear capacity and yielding moment of columns

Column	Axial Load (kN)	Shear Capacity (kN)	Moment Capacity (kN-m)
A1, A3, C1, C3	10.81	28.76	16.56
A2, C2	16.91	29.02	16.96
B1, B3	17.38	29.04	16.99
B2	26.76	29.42	17.60

6.2.3 Model and load pattern

To represent hydrodynamic force acting uniformly to the building, elements in columns and beams are divided with an interval of 0.2 m and 0.5 m, respectively. For the ends columns, the element size is equal to the plastic hinge length of 0.24 m. As shown in Figure 6-2, the analytical column model comprises the zero length shear springs at the ends, the fiber elements at the plastic hinge regions, and elastic elements. The frame model of this study is shown in Figure 6-3. The frame model comprises the zero length shear springs at the ends of beams and columns, the fiber elements at the plastic hinge regions and elastic elements. Beam-column joint is assumed to be a rigid joint.

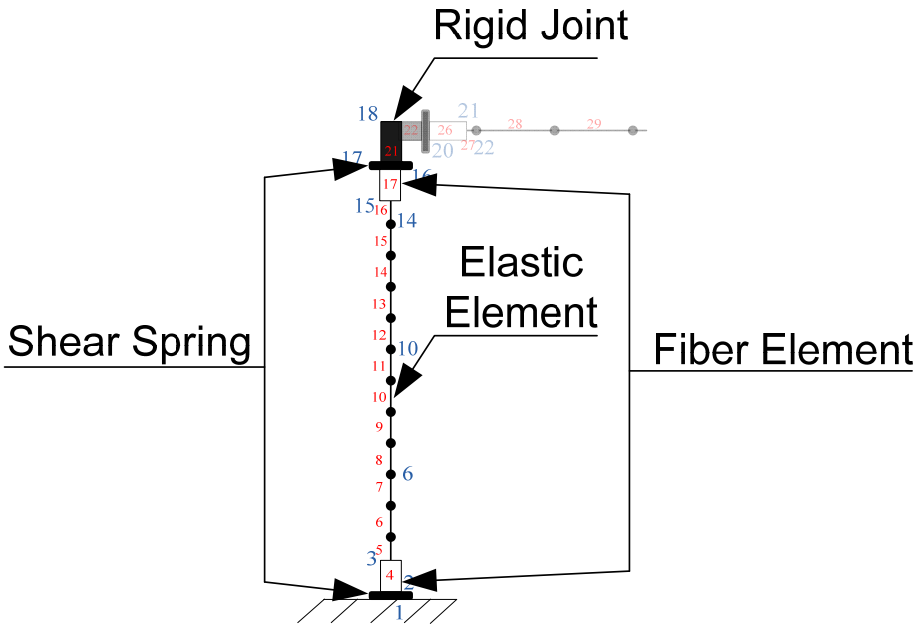

Figure 6-2. Column model

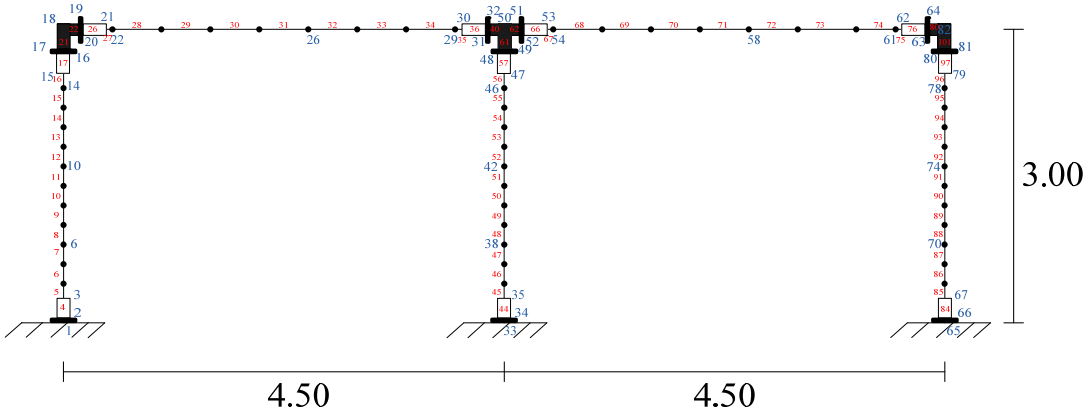

Figure 6-3. Frame model

The hydrodynamic force is considered as a uniform lateral force through the depth. Hence, in this study, the tsunami load pattern is fixed as the tsunami inundation depth. The tsunami flow velocity is increased until collapse by using the force-controlled method. To represent the uniform distributed hydrodynamic force, the tsunami force is distributed to be point loads over tributary areas as shown in Figure 6-4. The tsunami force acts on all columns simultaneously as shown in Figure 6-5.

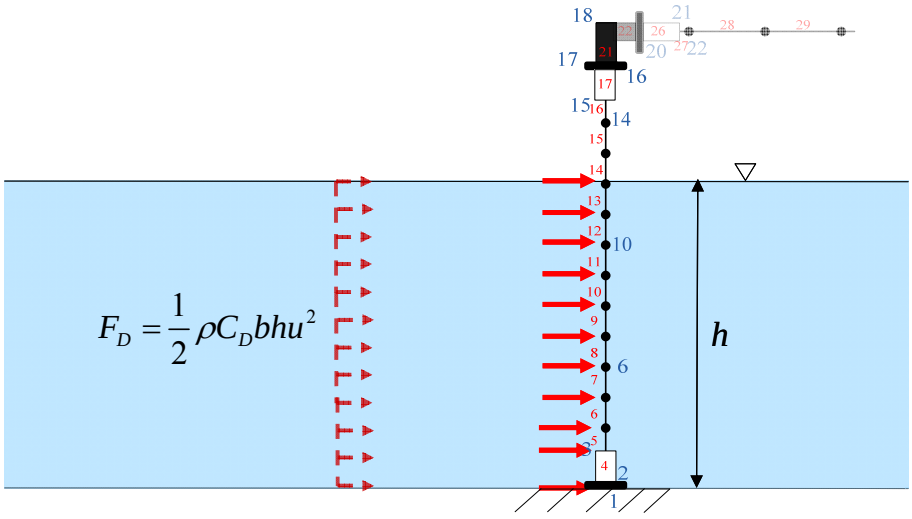

Figure 6-4. Distribution of tsunami load to joint elements

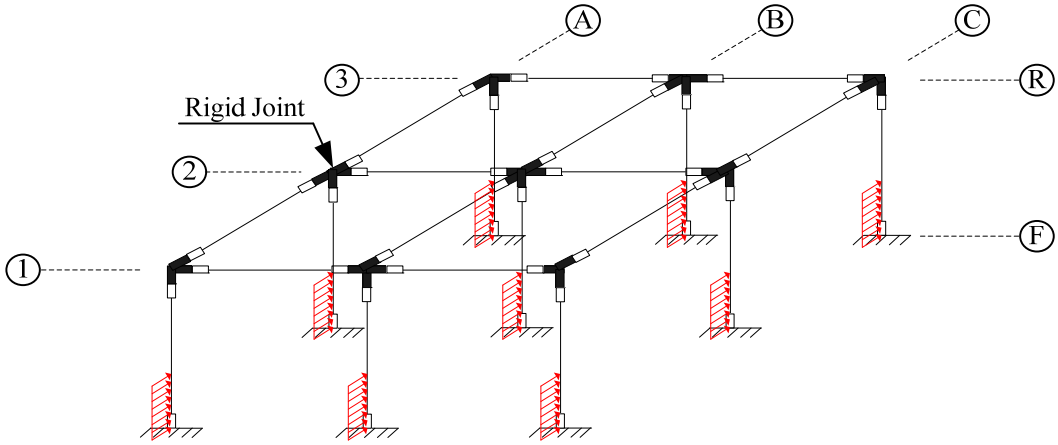

Figure 6-5. Building model and tsunami force acting on columns

6.3 Building Responses

The tsunami flow velocity is increased until collapse. The tsunami inundation depth is considered increasing with an interval of 0.2 m up to a depth of 3.2 m. The analytical results with the maximum load resistances, the maximum displacement and location, and failure mode for each inundation depth are listed in Table 6-4.

Table 6-4. The maximum load resistances, the maximum displacement and location, and failure mode for each inundation depth

No.	Inundation Depth (m)	Max. Load (kN)	Max. Displacement		Failure mode
			(mm)	Location	
1	0.24	259.3	5.5	Col A3, C3	Shear failure in Columns A3 and C3
2	0.40	259.5	6.1	Col A3, C3	Shear failure in Columns A3 and C3
3	0.60	259.7	7.3	Col A3, C3	Shear failure in Columns A3 and C3
4	0.80	259.5	8.8	Col A3, C3	Shear failure in Columns A2 and C2
5	1.00	259.0	10.3	Col A3, C3	Shear failure in Columns A2 and C2
6	1.20	258.5	12.0	Col A3, C3	Shear failure in Columns A2 and C2
7	1.40	257.9	13.7	Col A3, C3	Shear failure in Columns A2 and C2
8	1.60	257.3	15.6	Col A3, C3	Shear failure in Columns A2 and C2
9	1.80	256.7	18.6	Col A3, C3	Shear failure in Columns A2 and C2
10	2.00	255.5	22.9	Col A3, C3	Shear failure in Columns A2 and C2
11	2.20	254.5	27.2	Col A3, C3	Shear failure in Columns A2 and C2
12	2.40	258.4	37.8	Col A3, C3	Shear failure in Column B3
13	2.57	243.1	40.4	Col A3, C3	Flexural failure in Column B2
14	2.80	223.2	40.3	Col A3, C3	Flexural failure in Column B2
15	3.00	147.2	41.1	Col B3	Flexural failure in Column B2
16	3.20	134.2	41.7	Col B3	Flexural failure in Column B2

6.3.1 Definition of failure

At the collapse point, two failure modes in beams or columns are considered; the shear failure and flexural failure. The shear failure in beams or columns is defined that the shear force in beams or columns reaches shear capacity. The flexural failure

in beams or columns is defined that the stress of the covering concrete reaching its peak which is a crushing in the compression covering concrete.

6.3.2 Tsunami inundation depth of 0.6 m

The building is subjected to the tsunami lateral force for an inundation depth of 0.6 m. The relationship of the lateral force and the maximum roof displacement is shown in Figure 6-6. The maximum lateral force is 259.7 kN. The maximum roof displacement is 7.3 mm at Columns A3 and C3. The lateral force is controlled by the shear failure in Columns A3 and C3. The shear forces of each column are quite equal as listed in Table 6-5. Shear forces in Columns A3 and C3 are 28.76 kN, which reach the maximum shear capacity. The relationship of shear force and deformation of shear spring in Column A3 is shown in Figure 6-7. Figure 6-8 shows the moment and curvature relationship of Column B2 which has the maximum stress of covering concrete. The moment of Column B2 is 6.0 kN-m, which is about 30% of the moment capacity.

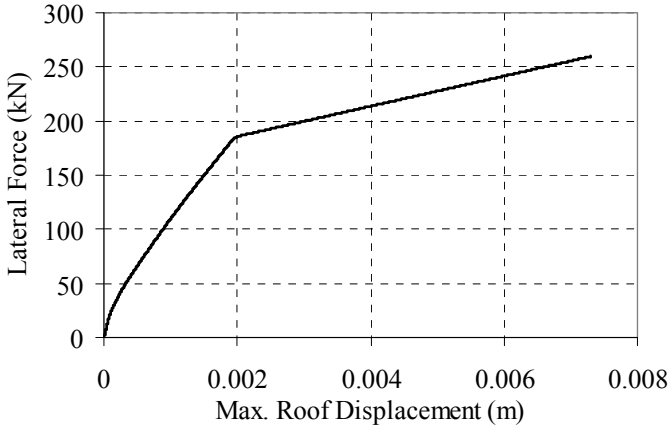

Figure 6-6. Force and maximum roof displacement under as inundation depth of 0.6 m

Table 6-5. Shear force in column under an inundation depth of 0.6 m

Column	A1	A2	A3	B1	B2	B3	C1	C2	C3
Shear Force (kN)	28.72	29.00	28.76	28.79	29.13	28.84	28.72	29.00	28.76

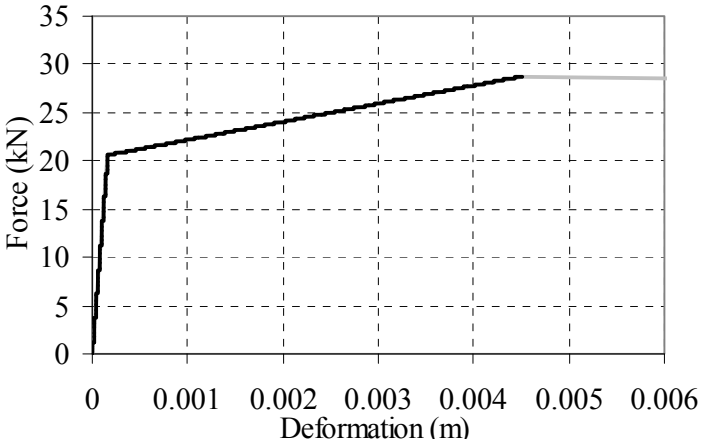

Figure 6-7. Force and deformation relationship of the shear spring in Column A3 under an inundation depth of 0.6 m

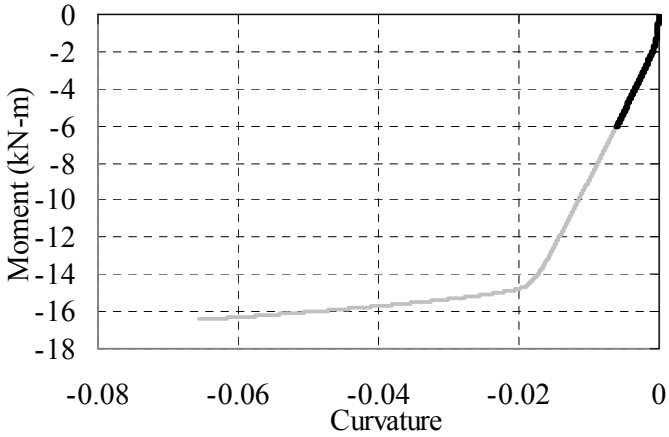

Figure 6-8. Moment and curvature relationship of Column B2 under an inundation depth of 0.6 m

6.3.3 Tsunami inundation depth of 2.2 m

The building is subjected to the tsunami lateral force for an inundation depth of 2.2 m, the relationship of the lateral force and the maximum roof displacement is shown in Figure 6-9. The maximum lateral force is 254.5 kN. The maximum roof displacement is 27.2 mm at Columns A3 and C3. The lateral force is controlled by the shear failure in Columns A2 and C2. The shear forces of each column are listed in Table 6-6. The shear forces in Columns A2 and C2 are 29.02 kN, which reach the maximum shear capacity. The relationship of shear force and deformation of shear spring in Column A2 is shown in Figure 6-10. Figure 6-11 shows the moment and curvature relationship of Column B2 which has the maximum stress of covering concrete. The moment of Column B2 is 17.2 kN-m, which is about 97.7% of the moment capacity.

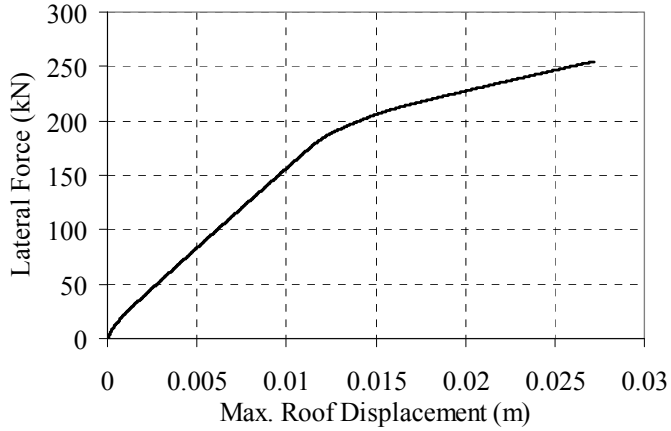

Figure 6-9. Force and maximum roof displacement under an inundation depth of 2.2 m

Table 6-6. Shear force in column under an inundation depth of 2.2 m

Column	A1	A2	A3	B1	B2	B3	C1	C2	C3
Shear Force (kN)	27.61	29.02	27.98	27.79	29.35	28.17	27.61	29.02	27.98

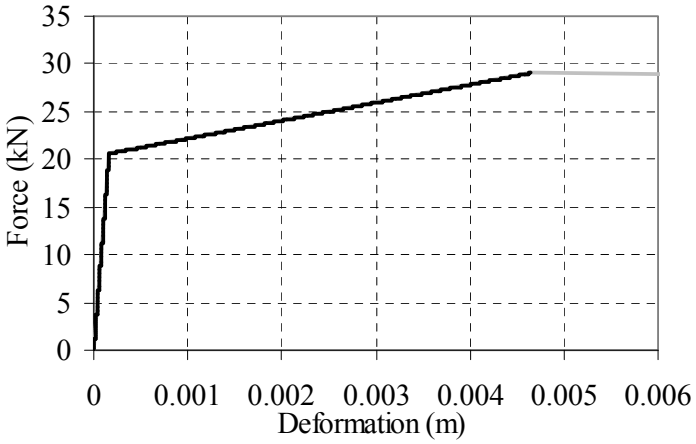

Figure 6-10. Force and deformation relationship of the shear spring in Column A2 under an inundation depth of 2.2 m

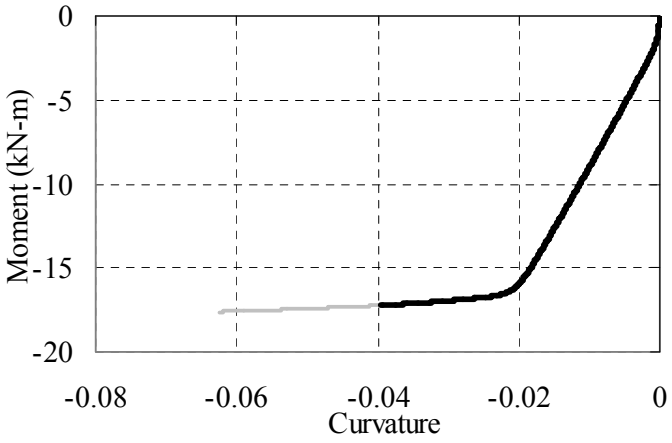

Figure 6-11. Moment and curvature relationship of Column B2 under an inundation depth of 2.2 m

6.3.4 Tsunami inundation depth of 2.4 m

Figure 6-12 shows the relationship of the lateral force and the maximum roof displacement of the building subjected to the tsunami lateral force for an inundation depth of 2.4 m. The maximum lateral force is 258.4 kN. The maximum roof displacement is 37.8 mm at Columns A3 and C3. The lateral force is controlled by the shear failure in Column B3. The shear forces of each column are listed in Table 6-7. The shear force in Column B3 is 29.04 kN, which reach the maximum shear capacity. The relationship of shear force and deformation of shear spring in Column B3 is shown in Figure 6-13. Figure 6-14 shows the moment and curvature relationship of Column B2. The moment of Column B2 is 17.5 kN-m, which is about 99.5% of the moment capacity.

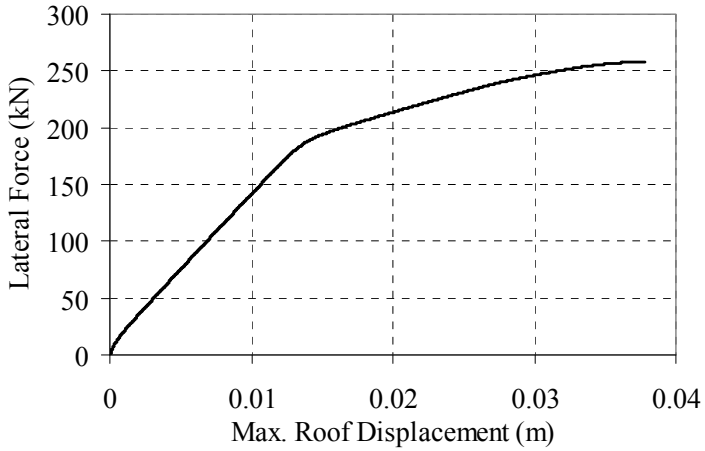

Figure 6-12. Force and maximum roof displacement under an inundation depth of 2.4 m

Table 6-7. Shear force in column under an inundation depth of 2.4 m

Column	A1	A2	A3	B1	B2	B3	C1	C2	C3
Shear Force (kN)	28.15	28.89	28.71	28.47	29.41	29.04	28.15	28.89	28.71

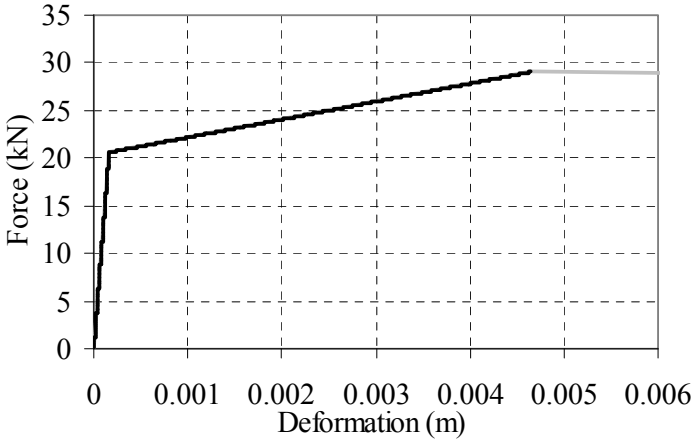

Figure 6-13. Force and deformation relationship of the shear spring in Column B3 under inundation depth of 2.4 m

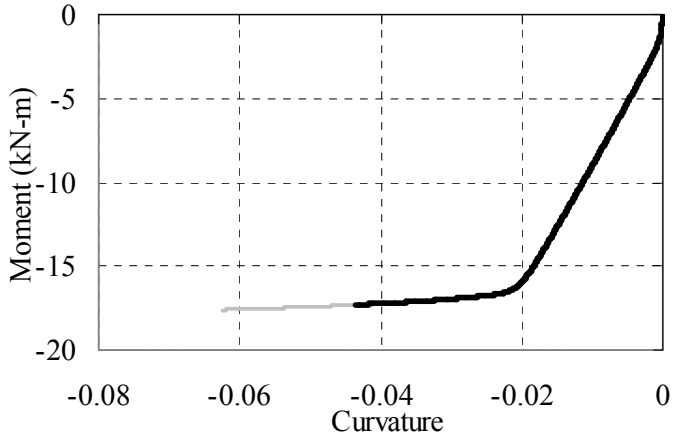

Figure 6-14. Moment and curvature relationship of Column B2 under an inundation depth of 2.4 m

6.3.5 Tsunami inundation depth of 2.57 m

Figure 6-15 shows the relationship of the lateral force and the maximum roof displacement of the building subjected to the tsunami lateral force for an inundation depth of 2.57 m. The maximum lateral force is 243.1. The maximum roof displacement is 40.4 mm at Columns A3 and C3. The lateral force is controlled by the flexural failure in Column B2. The shear forces of each column are listed in Table 6-8. The moment and curvature relationship of Column B2 is shown in Figure 6-16. Figure 6-17 shows the relationship of shear force and deformation of the shear spring in Column B2. The shear force in Column B2 is 27.68 kN.

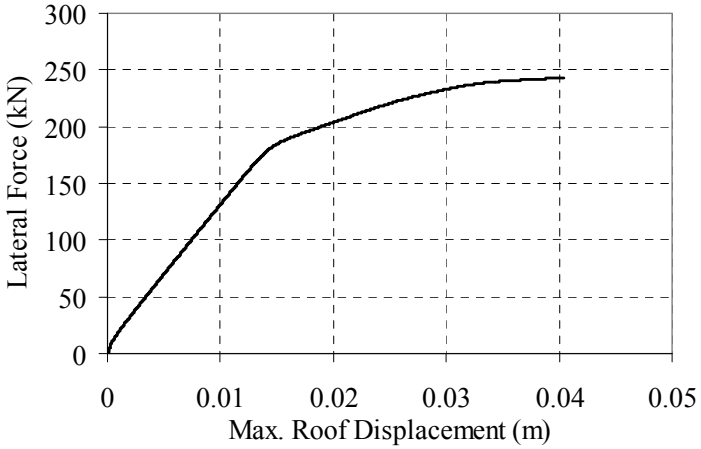

Figure 6-15. Force and maximum roof displacement under an inundation depth of 2.57 m

Table 6-8. Shear force in column under an inundation depth of 2.57 m

Column	A1	A2	A3	B1	B2	B3	C1	C2	C3
Shear Force (kN)	26.44	27.16	27.02	26.78	27.68	27.36	26.44	27.16	27.02

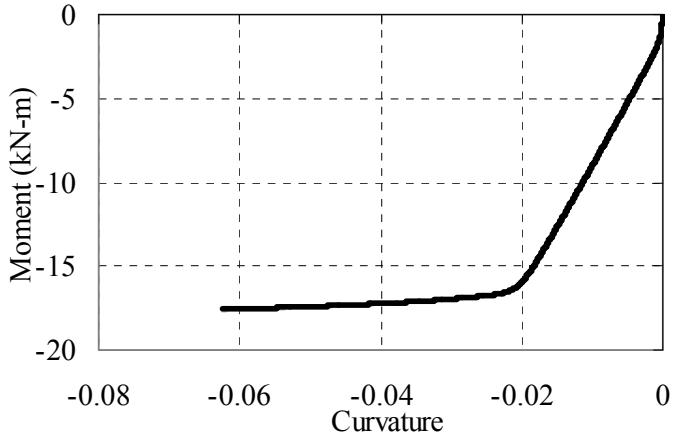

Figure 6-16. Moment and curvature relationship of Column B2 under an inundation depth of 2.57 m

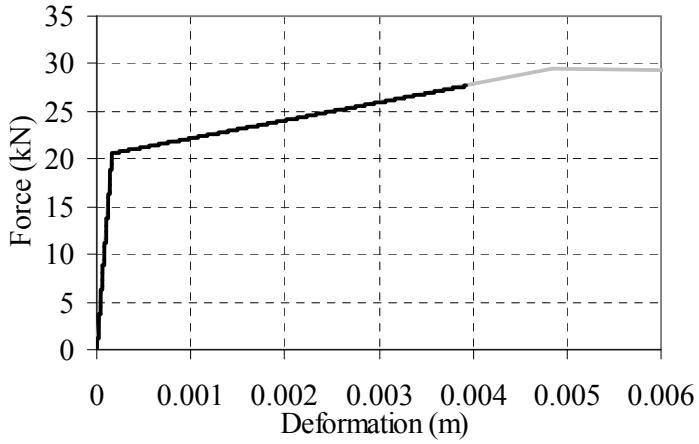

Figure 6-17. Force and deformation relationship of the shear spring in Column B2 under inundation depth of 2.57 m

6.3.6 Tsunami inundation depth of 3.2 m

Figure 6-18 shows the relationship of the lateral force and the maximum roof displacement of the building subjected to the tsunami lateral force for an inundation depth of 3.2 m. The maximum lateral force is 134.2 kN. The maximum roof displacement is 41.7 mm at Column B2. The lateral force is controlled by the flexural failure in Column B2. The shear forces of each column are listed in Table 6-9. The moment and curvature relationship of Column B2 is shown in Figure 6-20. Figure 6-19 shows the relation ship of shear force and deformation of the shear spring in Column B2. The shear force in Column B2 is 15.73 kN.

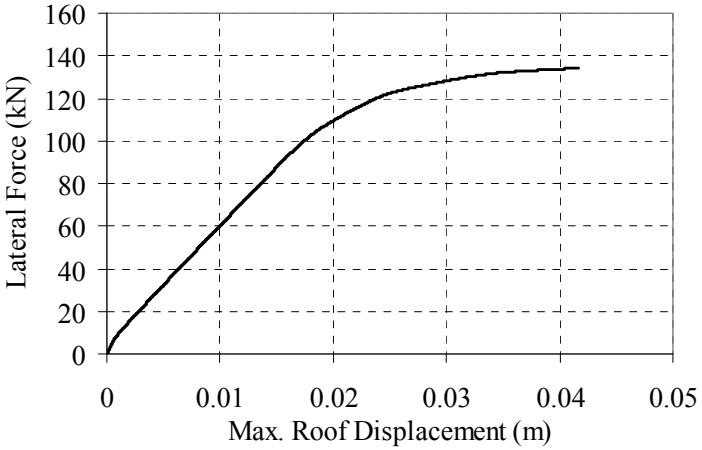

Figure 6-18. Force and maximum roof displacement under an inundation depth of 3.2 m

Table 6-9. Shear force in column under an inundation depth of 3.2 m

Column	A1	A2	A3	B1	B2	B3	C1	C2	C3
Shear Force (kN)	14.18	15.02	14.91	14.77	15.73	15.51	14.18	15.02	14.91

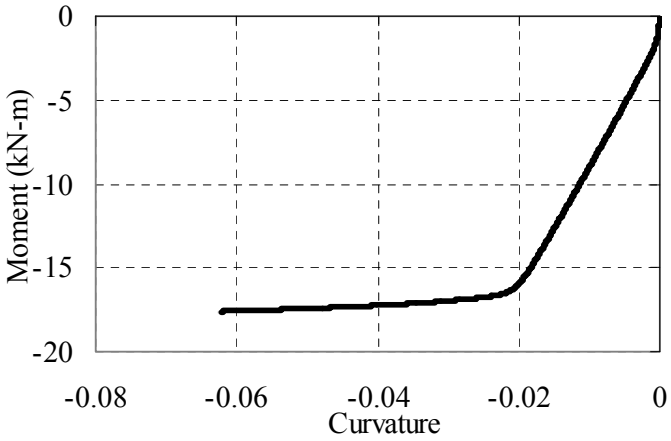

Figure 6-19. Force and deformation relationship of the shear spring in Column B2 under inundation depth of 3.2 m

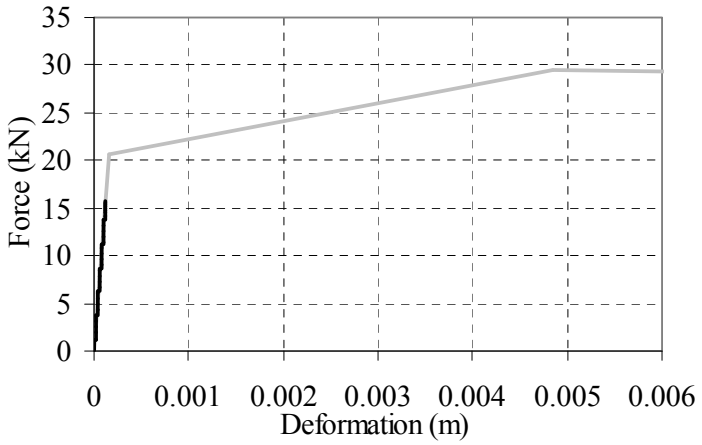

Figure 6-20. Moment and curvature relationship of Column B2 under an inundation depth of 3.2 m

6.3.7 Effect of the inundation depth on building responses

The tsunami inundation depth is considered increasing with an interval of 0.2 m up to a depth of 3.2 m. The analytical results with maximum load resistances, maximum displacement and location, and failure mode of each tsunami inundation depth are listed in Table 6-4. The relationship of the force and maximum roof displacement under all tsunami inundation depths is shown in Figure 6-21. Table 6-10 shows the shear force in all columns under all tsunami inundation depths.

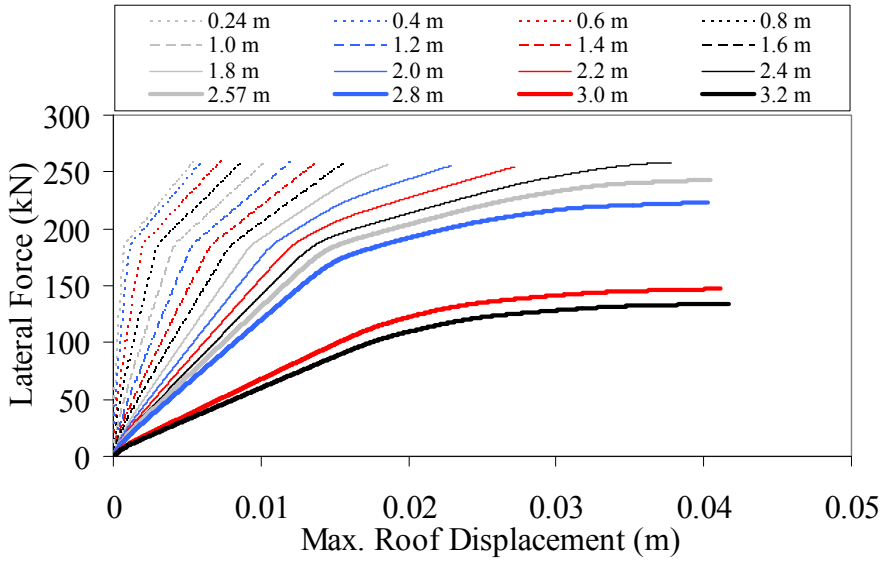

Figure 6-21. Force and maximum roof displacement under tsunami

As listed in Table 6-4 and Figure 6-21, the maximum resistances of the building slightly increase from 259.3 kN to 259.7 kN for the inundation depths of 0.24 m to 0.6 m. The lateral resistance is controlled by the shear failure in Columns A3 and C3. The shear forces of each column are quite equal as listed in Table 6-10. The Columns A3 and C3 have the least shear capacity.

Table 6-10. Shear force in column under all tsunami inundation depths

No.	Inundation Depth (m)	Shear Force in Columns (kN)								
		A1	A2	A3	B1	B2	B3	C1	C2	C3
1	0.24	28.74	28.89	28.76	28.78	28.97	28.81	28.74	28.89	28.76
2	0.40	28.73	28.94	28.76	28.79	29.03	28.83	28.73	28.94	28.76
3	0.60	28.72	29.00	28.76	28.79	29.13	28.84	28.72	29.00	28.76
4	0.80	28.66	29.02	28.72	28.73	29.16	28.80	28.66	29.02	28.72
5	1.00	28.57	29.02	28.64	28.65	29.16	28.72	28.57	29.02	28.64
6	1.20	28.47	29.02	28.56	28.55	29.17	28.64	28.47	29.02	28.56
7	1.40	28.36	29.02	28.48	28.44	29.17	28.56	28.36	29.02	28.48
8	1.60	28.24	29.02	28.38	28.33	29.18	28.47	28.24	29.02	28.38
9	1.80	28.04	29.02	28.27	28.22	29.31	28.45	28.04	29.02	28.27
10	2.00	27.81	29.02	28.12	28.00	29.33	28.31	27.81	29.02	28.12
11	2.20	27.61	29.02	27.98	27.79	29.35	28.17	27.61	29.02	27.98
12	2.40	28.15	28.89	28.71	28.47	29.41	29.04	28.15	28.89	28.71
13	2.57	26.44	27.16	27.02	26.78	27.68	27.36	26.44	27.16	27.02
14	2.80	24.23	24.96	24.82	24.57	25.47	25.17	24.23	24.96	24.82
15	3.00	15.65	16.46	16.36	16.20	17.15	16.91	15.65	16.46	16.36
16	3.20	14.18	15.02	14.91	14.77	15.73	15.51	14.18	15.02	14.91

For inundation depths of 0.8 m to 2.2 m, the lateral resistances are about 255 kN which are controlled by the shear failure in Columns A2 and C2. At this stage, the load is shared between the columns in each frame, so the shear failure occurs in the middle column. As shown in Figure 6-22, the flexural moment of Column B2 is significantly increased. The stress of covering concrete in Column B2 is larger than 20 MPa at an inundation depth of 2.0 m as shown in Figure 6-23. The longitudinal reinforcement in Column B2 yields at an inundation depth of 1.8 m as shown in Figure 6-24. At a tsunami inundation depth of 2.4 m, the lateral resistance slightly increases to 258.4 kN. The shear failure of Column B3 controls the lateral resistance of the building. From the stress-strain of covering concrete in Column B2, it is seen that the flexural failure is about to occur.

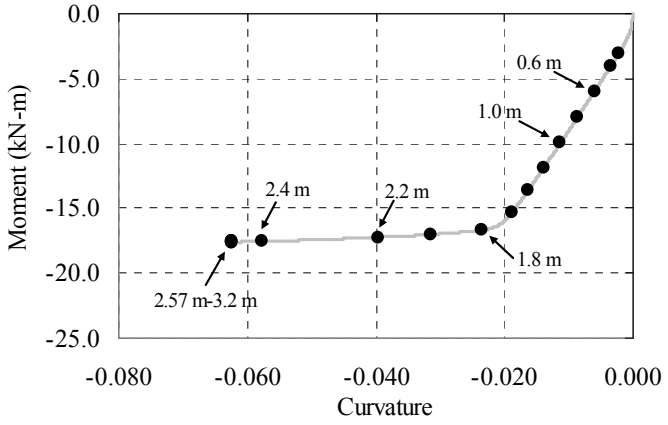

Figure 6-22. Moment and curvature relationship of Column B2 under all inundation depths

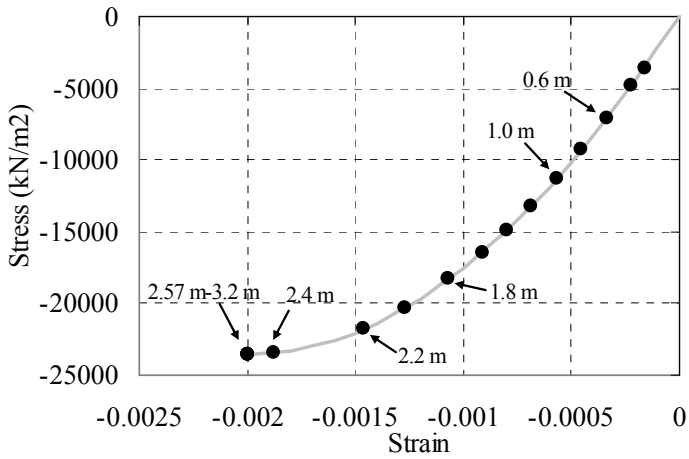

Figure 6-23. Stress-strain relationship of covering concrete of Column B2 under all inundation depths

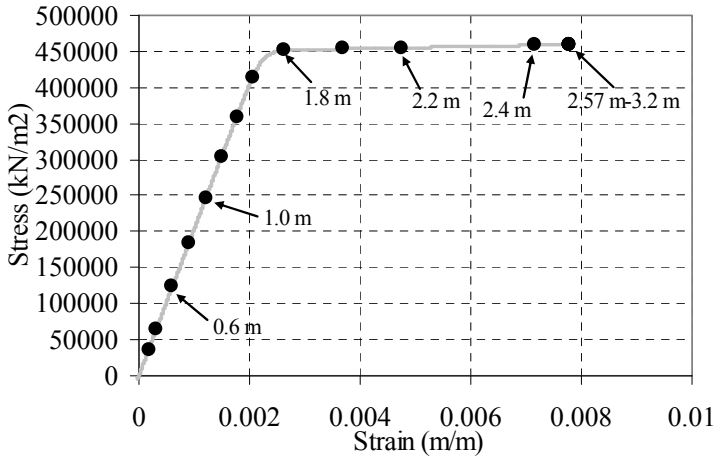

Figure 6-24. Stress-strain relationship of reinforcement of Column B2 under all inundation depths

The failure mode of the building changes from a shear failure to a flexure failure in Column B2 at the inundation depth of 2.57 m with the lateral resistance of 243.1 kN. For inundation depths of 2.8 m to 3.2 m, the lateral resistances are controlled by the flexural failure in Column B2. The maximum resistance decreases from 223.2 kN to 134.2 kN due to a change of the failure mode. At inundation depths of 3.0 m and 3.2, tsunami acts on the roof beams, then the flexural failure occurs rapidly. The maximum resistance decreases significantly. Shear forces in columns are about 15.5 kN.

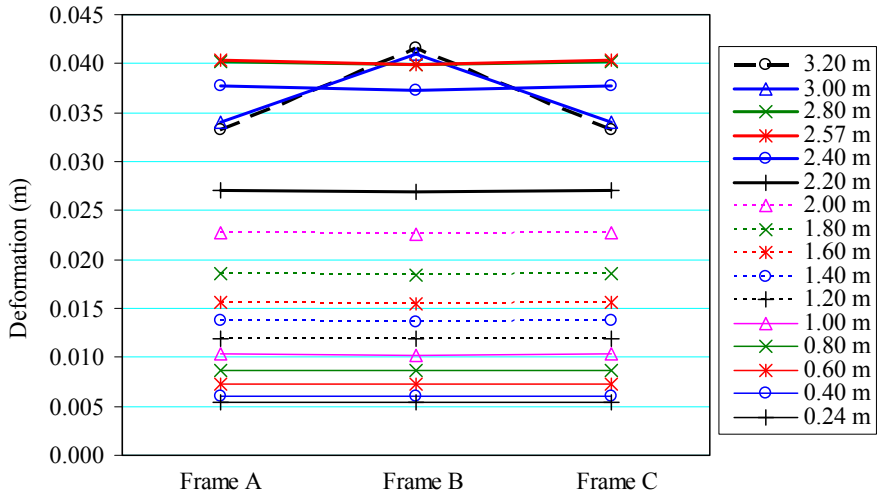

Figure 6-25. Deformation of the middle frame

Figure 6-25 describes the deformations of the middle frame under all tsunami inundation depths. The deformations of all frames are quite equal for inundation depths from 0.24 m to 2.8 m. For inundation depths from 3.0 m to 3.2 m, the deformation of Frame B is larger than the deformation of Frames A and C. The deformation increases according to inundation depth. From an inundation depth of 1.8 m, the deformation increases rapidly due to the yielding of the reinforcement in Column B2. At an inundation depth of 2.4 m, the flexural failure closely occurs, so the deformation increases largely. At inundation depths from 2.57 m and 3.2 m, the deformations are quite equal because the building fails in the same flexure mode.

6.3.8 Building responses and boundaries of tsunami flow velocities

As discussed in Chapter 3, from the study on tsunami flow velocities and analysis of tsunami flow velocities from recorded videos, the tsunami flow velocity is considered in the range from $0.7\sqrt{gh}$ to $2.0\sqrt{gh}$. The relationship of the lateral resistance and inundation depth is plotted with the forces corresponding to the boundaries of tsunami flow velocities as shown in Figure 6-26. In this the tsunami flow velocity range, the building reaches the collapse point for inundation depths from 2.0 m to 2.8 m. For the tsunami inundation depths of 3.0 m to 3.2 m, the tsunami flow velocities at the collapse point are less than $0.7\sqrt{gh}$.

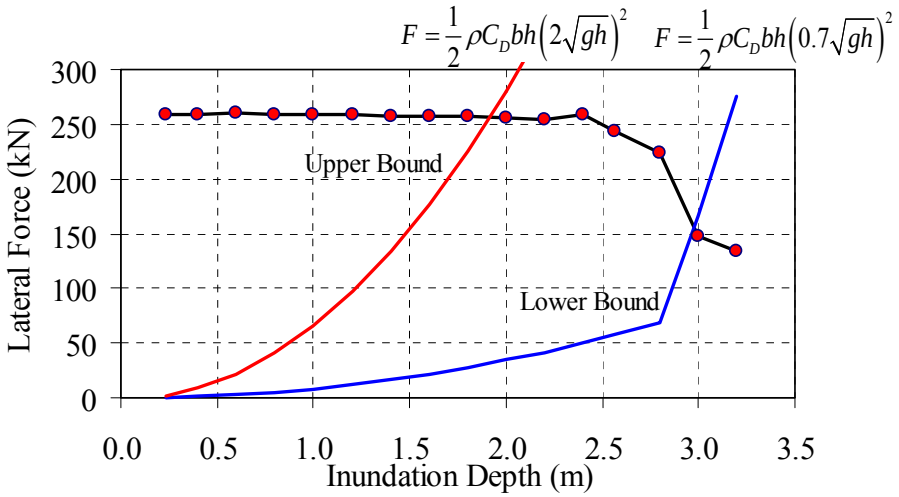

Note: ρ is water density, C_D is drag coefficient, b is width of structure, h is inundation depth and g is gravitational acceleration

Figure 6-26. Relationship of lateral resistance and inundation depth with the force corresponding to the boundaries of tsunami flow velocities

6.4 Effects of Uncertainty of Compressive Strength of Concrete

The compressive strength of concrete has an uncertainty due to the production of the concrete batch and measured strength in the testing process (ACI-214R, 2002). The uncertainty of compressive strength of concrete is assumed as the normal distribution as shown in Figure 6-27. To analyze the effect of the uncertainty of compressive strength of concrete to building responses under tsunami loading, the distribution of compressive strength with the specified compressive strength of 23.5 MPa need to be known.

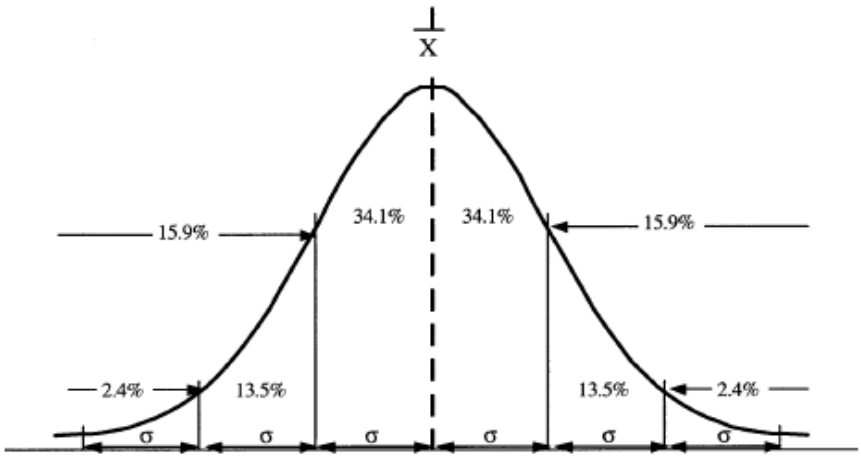

Figure 6-27. The distribution of concrete compressive strength assumed normal distribution (ACI-214R, 2002)

For the specified concrete strength, the concrete strength suggested by ACI-214R (2002) is expressed in equation 6-1, where f'_{cr} is the minimum required average strength, f'_c is the specified compressive strength, s is the standard deviation of the compressive test and z is a constant multiplier for the standard deviation (s) that depends on the number of tests expected to fall below the specified compressive strength. If test data is not available, the minimum required average strength can be computed by equation 6-2 (ACI-214R, 2002).

$$f'_{cr} = f'_c + zs \tag{6-1}$$

$$f'_{cr} = f'_c + 8.3 \text{ MPa} \tag{6-2}$$

Table 6-11. Properties associated with values of z (ACI-214R, 2002)

Chances of Falling below Lower Limit	z
3 in 10 (30%)	0.52
2.5 in 10 (25%)	0.67
2 in 10 (20%)	0.84
1 in 6.3 (15.9%)	1.00
1.5 in 10 (15%)	1.04
1 in 10 (10%)	**1.28**
1 in 20 (5%)	1.65
1 in 40 (2.5%)	1.96
1 in 44 (2.3%)	2.00
1 in 100 (1%)	**2.33**
1 in 200 (0.5%)	2.58
1 in 741 (0.13%)	3.00

The constant multiplying for standard deviation (z) depends on the number of tests expected to fall below the specified compressive strength as listed in Table 6-11. In the other words, the constant multiplier for the standard deviation (z) depends on the quality standard of a concrete plant. To estimate the standard deviation of the compressive test, the constant multiplier for standard deviation (z) need to be known. ACI-214R (2002) suggests that the common used values of the constant multiplier for standard deviation (z) are 1.28 and 2.33. For z of 1.28, the chance of falling below the specified concrete strength is 1 in 10 (10%), which is for a low quality standard concrete plant. For z of 2.33, the chance of falling below the specified concrete strength is 1 in 100 (1%), which is for a low quality standard concrete plant.

In this study, the uncertainty of compressive strength of concrete is used to analyze the responses of the building under tsunami loading and to develop the tsunami fragility curve. To estimate the distribution of compressive strength with the specified compressive strength of 23.5 MPa, the constant multiplier for standard

deviation (z) of 1.28, which is a low quality standard concrete plant, is selected. From equation 6-1 and equation 6-2, it can be known that zs is 8.3 MPa. Therefore, the required average strength is 31.84 MPa, and the standard deviation of the concrete compressive strength uncertainty is 6.48 MPa with the constant multiplier for standard deviation (z) of 1.28. The distribution of concrete strength with the required average strength is 31.84 MPa and the specified compressive strength of 23.5 MPa is shown in Figure 6-28.

Table 6-12. The variation of compressive strengths

	$\mu-3s$	$\mu-2s$	$\mu-s$	μ	$\mu+s$	$\mu+2s$	$\mu+3s$
Compressive Strength (MPa)	12.4	18.9	25.4	31.8	38.3	44.8	51.3

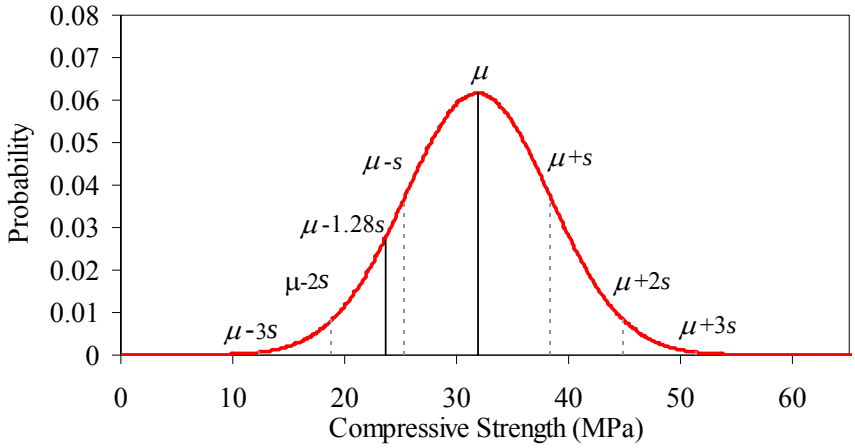

Figure 6-28. The distribution of concrete strength with the required average strength is 31.8 MPa and the specified compressive strength of 23.5 MPa

The variation of compressive strengths is listed in Table 6-12. The specified compressive strength is at $\mu-1.28s$. To analyze the responses of the building under tsunami loading and develop the tsunami fragility curve in this study, the compressive strengths of concrete are selected as 15.7 MPa, 23.5 MPa, 31.4 MPa, 39.2 MPa and 47.1 MPa. The calculation parameters of core concrete of all compressive strengths used in the analysis are listed in Table 6-13. The compressive strengths of core concrete are increased, but the strains at the peak stress are decreased. Table 6-14 shows the shear capacity and moment capacity of columns for all compressive strengths. The shear capacity and moment capacity of columns increase according to compressive strength of concrete. The maximum shear capacity and moment capacity are of the middle column, Column B2, which has the highest axial force. The building responses of the compressive strengths of 15.7 MPa, 23.5 MPa, 31.4 MPa, 39.2 MPa and 47.1 MPa are in Appendix B.

Table 6-13. Calculation parameters used in analysis of core concrete of all compressive strengths

Compressive Strength (MPa)	Elastic Modulus (GPa)	Element	Core Concrete	
			Strength (MPa)	Strain
15.7	18.6	Beam	16.57	0.00296
		Column	16.91	0.00335
23.5	22.8	Beam	24.41	0.00264
		Column	24.76	0.00290
31.4	26.3	Beam	32.26	0.00248
		Column	32.61	0.00267
39.2	29.4	Beam	40.11	0.00239
		Column	40.46	0.00254
47.1	35.9	Beam	47.96	0.00232
		Column	48.31	0.00245

Table 6-14. Shear capacity and yielding moment of columns of all compressive strengths

Compressive Strength (MPa)	Column	Shear Capacity (kN)	Moment Capacity (kN-m)
15.7	A1, A3, C1, C3	27.16	15.68
	A2, C2	27.42	16.05
	B1, B3	27.43	16.08
	B2	27.81	16.64
23.5	A1, A3, C1, C3	28.76	16.56
	A2, C2	29.02	16.96
	B1, B3	29.04	16.99
	B2	29.42	17.60
31.4	A1, A3, C1, C3	30.11	17.33
	A2, C2	30.37	17.73
	B1, B3	30.39	17.76
	B2	30.77	18.38
39.2	A1, A3, C1, C3	31.29	18.05
	A2, C2	31.55	18.45
	B1, B3	31.57	18.49
	B2	31.96	19.11
47.1	A1, A3, C1, C3	32.37	18.73
	A2, C2	32.63	19.14
	B1, B3	32.65	19.17
	B2	33.04	19.81

6.4.1 Effect of compressive strength on failure mode

In this study, two primary failure modes occurred in the building, which are the shear failure and flexural failure. The shear failure in beams or columns is defined that the shear force in beams or columns reaches shear capacity. The flexural failure in beams or columns is defined that the stress of the covering concrete reaching its peak which is a crushing in the compression covering concrete. The failure modes are slightly affected by the uncertainty of compressive strength of concrete. The failure modes are listed in Table B-1, Table 6-4, Table B-2, Table B-3 and Table B-4 for the compressive strength of concrete of 15.7 MPa, 23.5 MPa, 31.4 MPa, 39.2 MPa and

47.1 MPa, respectively. The lateral forces and tsunami inundation depth relationship of various compressive strengths with the failure mode is shown in Figure 6-29.

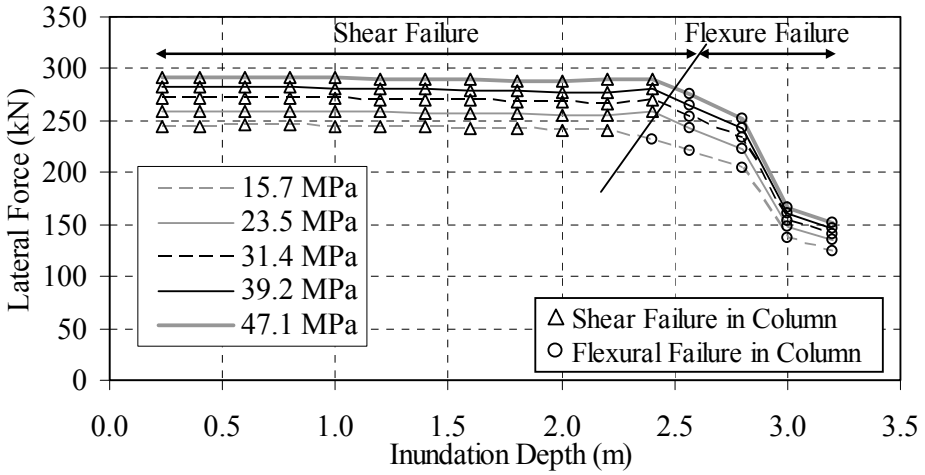

Figure 6-29. Lateral resistance and inundation depth relationship of various compressive strengths with the failure modes

For the inundation depths from 0.24 m to 2.4 m, the lateral resistances are controlled by the shear failure. Only for the compressive strength of 15.7 MPa, the lateral resistance of the building is controlled by the flexural failure in Column B2. The shear failure occurs in Columns A3 and C3 at the low inundation depth. Columns A3 and C3 have the lowest shear capacity. At an inundation depth of 0.6 m, the lateral resistance is controlled by the shear failure in Columns A3 and C3 for the compressive strengths of 15.7 MPa, 23.5 MPa and 31.4 MPa, For the compressive strength of concrete larger than 31.4 MPa, the lateral resistance is controlled by the shear failure in Columns A2 and C2 or in Column B3 because of an increase of the shear capacity of the columns at the corner and shared forces between columns in each frame. For the inundation depths from 2.57 m to 3.2 m, the lateral resistances are controlled by the flexural failure in Column B2.

6.4.2 Effect of compressive strength on lateral resistance

The lateral resistances of building are affected by the uncertainty of compressive strength of concrete. As listed in Table 6-14, the shear capacity and moment capacity of column are increased according to the compressive strength of concrete. The lateral resistance and tsunami inundation depth relationship of various compressive strengths is shown in Figure 6-29. The lateral resistances increase according to the compressive strength of concrete but also depend on the failure mode. For the compressive strengths of 15.7 MPa and 23.5 MPa, the lateral

resistances increase about 14.3 kN for shear failure and about 10.7 kN for flexural failure. For the compressive strengths of 23.5 MPa and 31.4 MPa, the lateral resistances increase about 12.1 kN for shear failure and about 6.2 kN for flexural failure. The lateral resistances increase about 10.6 kN for shear failure and about 5.8 kN for flexural failure for the compressive strengths of 31.4 MPa and 39.2 MPa. For the compressive strengths of 39.2 MPa and 47.1 MPa, the lateral resistances increase about 10.0 kN for shear failure and about 6.0 kN for flexural failure.

6.4.3 Effect of compressive strength on building deformation

The relationship of the maximum deformation and tsunami inundation depth for various compressive strengths is shown in Figure 6-30. The maximum deformations are not affected by the uncertainty of compressive strength of concrete for tsunami inundation depths from 0.24 m to 2.2 m, because the lateral resistance is controlled by the shear failure. At an inundation depth of 2.4 m, the maximum deformations are different; although, the lateral resistance is still controlled by the shear failure, because the flexural moment of Column B2 is significantly increased. For the inundation depths from 2.57 m to 3.2 m, the lateral resistance controlled by the flexural failure, the maximum deformations are clearly affected by the uncertainty of compressive strength. The maximum deformations increase according to the compressive strength of concrete because strains in the tension longitudinal reinforcement increase.

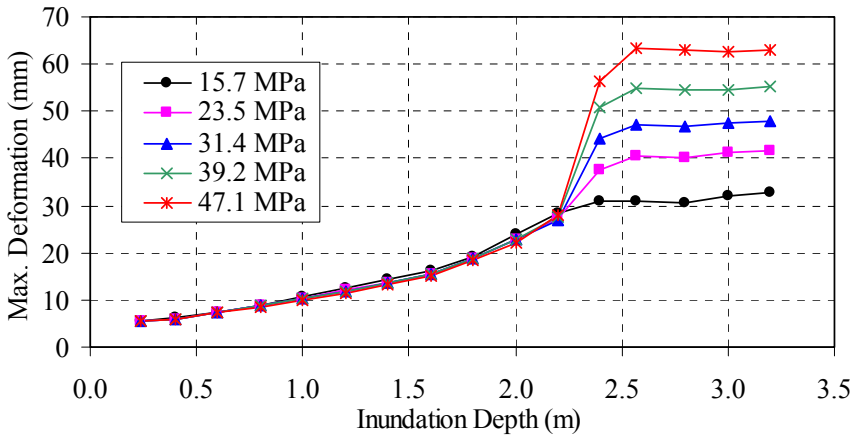

Figure 6-30. Maximum deformation and inundation depth relationship of various compressive strengths

6.4.4 Building responses for all compressive strengths and boundaries of tsunami flow velocities

The tsunami flow velocity is considered in the range from $0.7\sqrt{gh}$ to $2.0\sqrt{gh}$. The relationship of lateral resistance and inundation depth for all compressive strengths is plotted with the forces corresponding to the boundaries of tsunami flow velocity as shown in Figure 6-32. In this tsunami flow velocity range, the building reaches collapse for inundation depths from 2.0 m to 2.8 m. For the tsunami inundation depths of 3.0 m to 3.2 m, the tsunami flow velocities at the collapse point are less than $0.7\sqrt{gh}$.

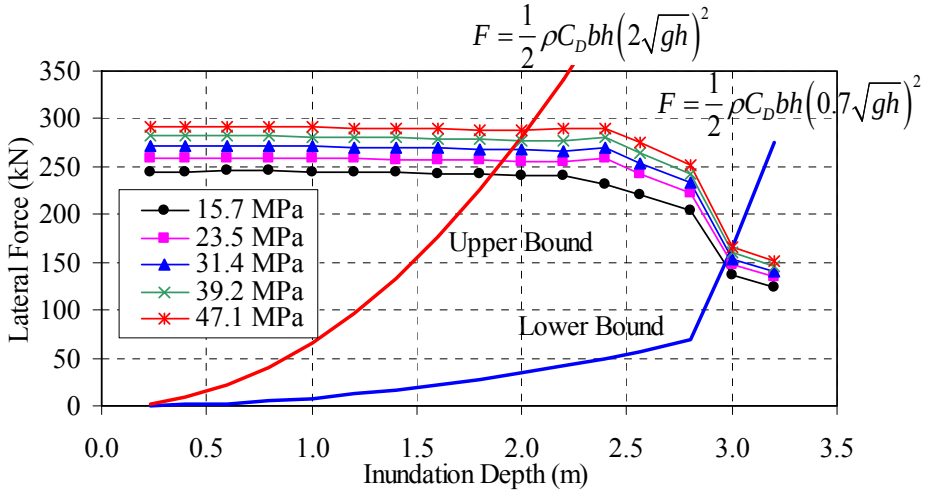

Note: ρ is water density, C_D is drag coefficient, b is width of structure, h is inundation depth and g is gravitational acceleration

Figure 6-31. Lateral resistance and inundation depth relationship of various compressive strengths with the force corresponding to the boundaries of tsunami flow velocities

6.5 Effects of Masonry Infill Walls

It is seen in the correlation analysis of reinforced-concrete building subjected to tsunami loads in Section 4.4 that masonry infill walls play an important role in the lateral load resisting capacity of a building. The effects of masonry infill walls are investigated by considering various arrangement patterns of walls. Masonry infill walls and columns are denoted as in Figure 6-32. Material properties of masonry infill walls are described in Section 4.3.2. Four cases are considered to study the effect of walls on the building responses and to compare with the cases without wall as listed in Table 6-15. The compressive strength of concrete is 23.5 MPa. The yield strength of reinforcement with a diameter of 6 mm, 12 mm and 16 mm are 319 MPa, 451 MPa and 549 MPa, respectively. The masonry infill wall is modeled as a horizontal spring.

The lateral resistance of masonry infill wall is 194.4 kN calculated by the equation proposed by Mostafaei and Kabeyasawa (2004).

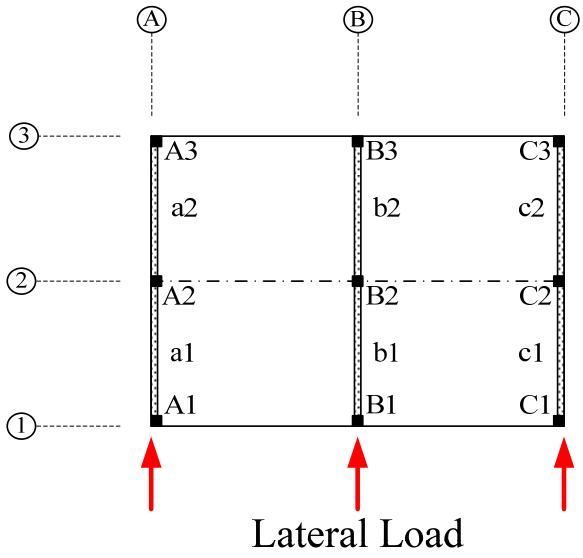

Figure 6-32. Definition of masonry infill walls and columns

Table 6-15. The location and the percentage of masonry infill walls of each case

No.	Case name	Location of masonry infill wall						Percentage of infill wall	Number of locations of loading
		a1	a2	b1	b2	c1	c2		
1	Without wall	-	-	-	-	-	-	0.0	9
2	**a-c**	√	√	-	-	√	√	66.7	5
3	**a-b1-c**	√	√	√	-	√	√	83.3	4
4	**a-b2-c**	√	√	-	√	√	√	83.3	4
5	**a-b-c**	√	√	√	√	√	√	100.0	3

Inundation depths of 1.0 m, 1.6 m, 2.0 m, 2.57 m, 2.8 m, 3.0 m and 3.2 m are considered to analyze the effect of masonry infill wall on building responses. The detailed building responses of four walls arrangement patterns are in Appendix C. The lateral force and tsunami inundation depth relationship of various arrangement patterns of walls is shown in Figure 6-33. The tsunami force acts on only columns which are in contact with the flow. At inundation depths from 1.0 m to 2.8 m, the total laterals of the buildings with masonry infill walls are less than that of the building without masonry infill wall because the loaded areas are less from the presence of walls. Because the loaded areas of each case are different, the resistance in term of the momentum flux (hu^2) is used to compare the responses of buildings with and without masonry infill walls; where h is the tsunami inundation depth (m) and u is the tsunami flow velocity (m/s).

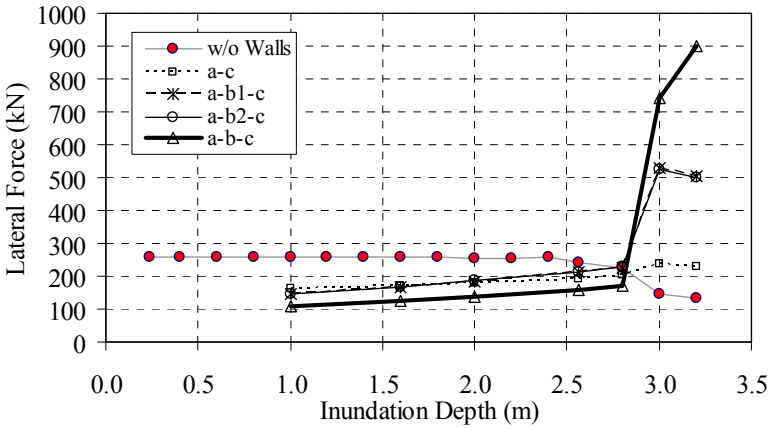

Note: Cases **a-b1-c** and **a-b2-c** are very close.

Figure 6-33. Lateral force and inundation depth relationship of various arrangement patterns of walls

6.5.1 Effect of masonry infill walls on failure mode and lateral resistance

Three failure modes occurred in the building with masonry infill walls, which are the shear failure in columns, flexural failure in columns and failure in walls. The shear failure in columns is defined that the shear force in columns reaches shear capacity. The flexural failure in beams or columns is defined that the stress of the covering concrete reaching its peak which is a crushing in the compression covering concrete. The failure in walls is defined that the lateral force in walls reaches its capacity. The failure modes and the momentum fluxes are listed in Table C-1, Table C-3, Table C-5 and Table C-7 for the wall pattern Cases a-c, a-b1-c, a-b2-c and a-b-c, respectively.

As shown in Figure 6-33, the lateral resistances of the building with masonry infill walls in **Cases a-c**, **a-b1-c**, **a-b2-c** are controlled by the shear failure in column under the inundation depth from 1.0 m to 2.8 m. The lateral resistances of the building with masonry infill walls in **Cases a-b-c** are controlled by the shear failure in column until the inundation depth of 3.0 m. For **Cases a-b1-c** and **a-b2-c**, the lateral resistances are controlled by the failure in wall in Frame B which is the least lateral capacity with a wall in one span. For **Case a-b-c**, at an inundation depth of 3.2 m, the lateral resistances are controlled by the failure in wall in Frame B in the back span.

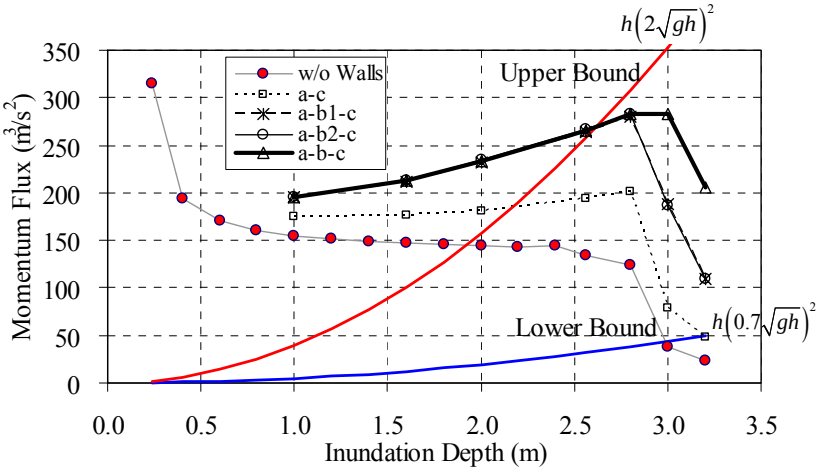

Note: h is inundation depth and g is gravitational acceleration
Cases **a-b1-c** and **a-b2-c** are very close.

Figure 6-34. Momentum flux and inundation depth relationship of various arrangement patterns of walls with the momentum flux corresponding to the boundaries of tsunami flow velocities

The relationship of Momentum flux and inundation depth of various arrangement patterns of walls is plotted with the momentum flux corresponding to the boundaries of tsunami flow velocities as shown in Figure 6-34. The momentum fluxes for the building with masonry infill walls increase with the inundation depths form 1.0 m to 2.8 m. At inundation depths of 3.0 m and 3.2 m, the momentum fluxes decrease because tsunami reaches the beam level. The building with masonry infill walls **Cases a-b1-c** and **a-b2-c** are the same. It means that the location of a wall in Frame B has no effect to the lateral resistance. In the considered tsunami flow velocity range, the building without masonry infill wall reaches the collapse point for inundation depths from 2.0 m to 2.8 m. For the tsunami inundation depths of 3.0 m to 3.2 m, the tsunami flow velocities at the collapse point are less than $0.7\sqrt{gh}$.

6.5.2 Effect of masonry infill walls on building deformation

The maximum deformation and tsunami inundation depth relationship of various arrangement patterns of walls is shown in Figure 6-35. Comparing with the deformations of the building without wall, the deformations of **Case a-c** are about 50% at inundation depths from 1.0 m to 2.8 m. For inundation depths of 3.0 m and 3.2 m, the deformations of **Case a-c** are almost equal to the building without wall because the building is failed by the flexural mode in columns in Frame B. For **Cases a-b1-c**, **a-b2-c** and **a-b-c**, the deformations are very small at inundation depths from 1.0 m to 2.8 m. For the inundation depths of 3.0 m and 3.2 m, the maximum deformations of Cases **a-b1-c**, **a-b2-c** and **a-b-c** increase to about 15 mm.

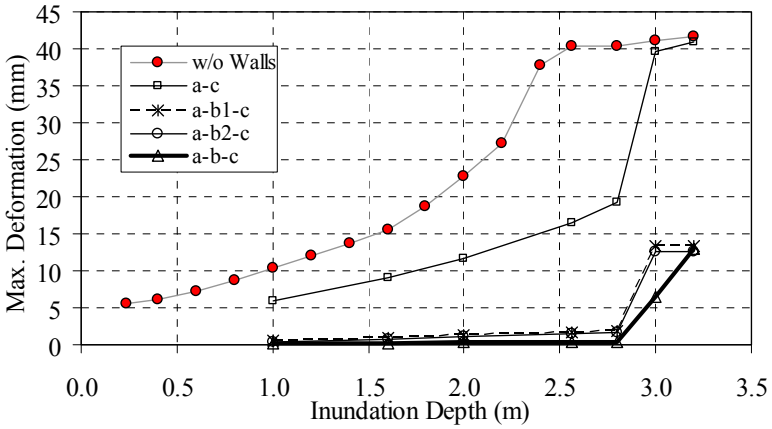

Note: Cases **a-b1-c** and **a-b2-c** are very close.

Figure 6-35. Maximum roof displacement and inundation depth relationship of various arrangement patterns of walls

CHAPTER VII
DEVELOPMENT OF TSUNAMI FRAGILITY CURVE

7.1 Uncertainties

To develop the fragility curve, the uncertainties have to be considered. In this study, the uncertainties are considered in terms of material properties and the tsunami flow velocities.

7.1.1 Compressive strength of concrete

The uncertainties of material properties are the compressive strength of concrete assumed to be a normal distribution (Tantala and Deodatis, 2002). The compressive strength of concrete has an uncertainty due to the production of the concrete batch and measured strength in the testing process (ACI-214R, 2002). From Section 6.4, concrete with a specified compressive strength of 23.5 MPa has a normal distribution with a mean of 31.8 MPa and standard deviation of 6.48 MPa. The distribution of compressive strength of concrete is shown in Figure 7-1. The compressive strengths of concrete of 15.7 MPa, 23.5 MPa, 31.4 MPa, 39.2 MPa and 47.1 MPa are considered to analyze the building responses and develop the tsunami fragility curve.

In the analysis, the tsunami load pattern is fixed by the tsunami inundation depth. The tsunami flow velocity is increased until collapse by using the force-controlled method. One hundred values of compressive strengths are selected in random for each tsunami inundation depth. There are 99 data in considering ranges of compressive strength of concrete. There is one value out of these ranges. The ranges and the number of random data of considering compressive strength of concrete for each tsunami inundation depth are listed in Table 7-1.

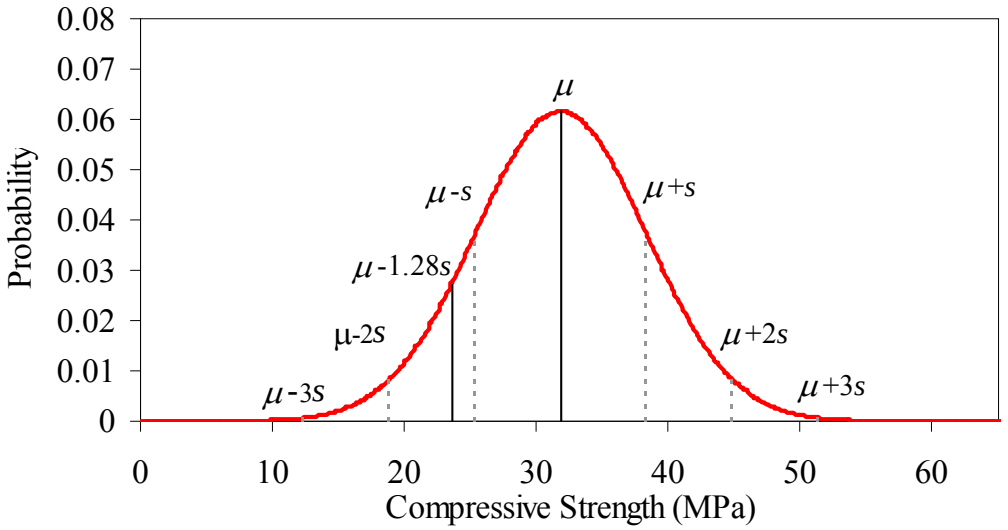

Figure 7-1. The distribution of specified compressive strength of 23.5 MPa with mean of 31.8 MPa and standard deviation of 6.5 MPa

Table 7-1. The ranges of compressive strength and the number of random data in each range for each inundation depth

Compressive. Strength (MPa)	Ranges of Compressive Strength (MPa)		The Number of Random Data
	From	To	
15.7	11.8	19.6	3
23.5	19.6	27.5	16
31.4	27.5	35.3	52
39.2	35.3	43.2	27
47.1	43.2	51.0	1
		Sum	99

7.1.2 Tsunami flow velocity

Due to uncertainties of tsunami flow velocity on land, the uncertainty of tsunami flow velocity from proposed formulations in past studies and past events is discussed in Chapter 3. The proposed estimating tsunami flow velocities are summarized. The uncertainty of tsunami flow velocity has to be in the possible range. To develop tsunami fragility curve in this study, the uncertainty of tsunami flow velocity is considered with in the boundary from $0.7\sqrt{gh}$ to $2.0\sqrt{gh}$. The lower bound and upper bound of tsunami velocities are plotted with the inundation depth as shown in Figure 7-2.

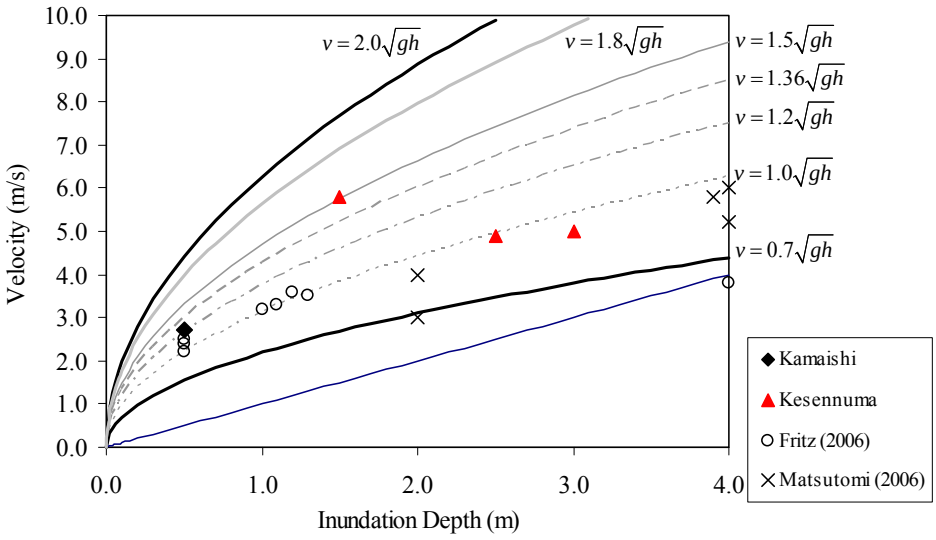

Figure 7-2. Relationship of the lower and upper bound tsunami flow velocity and tsunami inundation depth used to develop tsunami fragility curve

7.2 Estimation of Performance-Based Level

In this study, the tsunami fragility curve of one-story reinforced-concrete building with break away walls is developed based on the damage level. Damage level at the collapse point of the building model is considered to develop the tsunami fragility curve as a function of the tsunami inundation depth. From Chapter 6, the tsunami load pattern is fixed by the tsunami inundation depth. The tsunami flow velocity is increased until collapse by using the force-controlled method. From the proposed velocity boundaries, the lateral resistance and inundation depth relationship of all compressive strengths of concrete is plotted with the force corresponding to the boundaries of tsunami flow velocities from Figure 7-2 for each inundation depth as shown in Figure 7-3.

To develop the tsunami fragility curve, the probability is calculated from the number of data that occurs the considering damage level. Only the tsunami flow velocities between the boundaries are used to develop the tsunami fragility curve. The tsunami flow velocities exceeding the upper bound are not considered. For the tsunami flow velocities less than the lower bound, they are the cases that occur certainly. They are not considered to calculated probability. The tsunami flow velocities at collapse of all compressive strengths of concrete are summarized in Table 7-2. The tsunami flow velocities at collapse point are between the boundaries of tsunami flow velocities starting from the inundation depths from 2.0 m to 2.8 m as the shaded area in Table 7-2. At an inundation depth of 2.0 m, the tsunami flow velocity

at collapse point with the compressive strength of concrete of 47.1 is higher than the upper bound velocity.

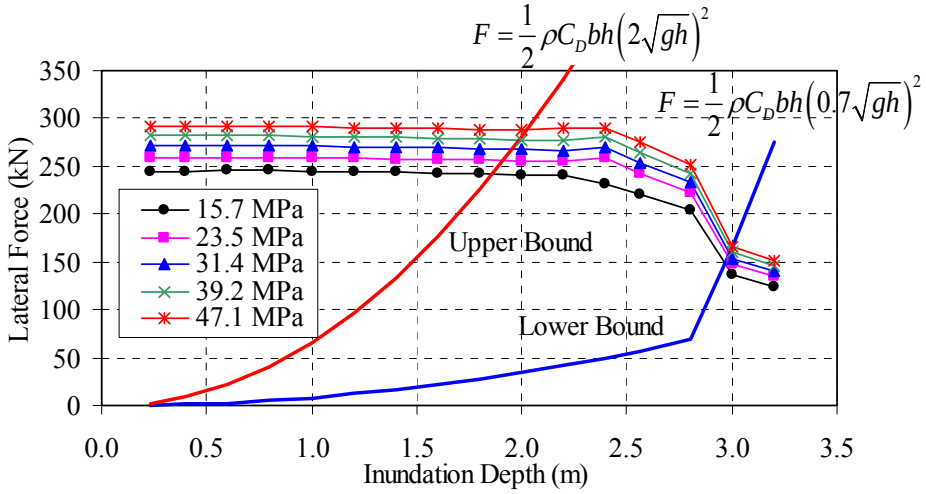

Note: ρ is water density, C_D is drag coefficient, b is width of structure, h is inundation depth and g is gravitational acceleration

Figure 7-3. Lateral resistance and inundation depth relationship of various compressive strengths with the force corresponding to the boundaries of tsunami flow velocities

Table 7-2. The lateral resistances and tsunami flow velocity at collapse of all compressive strengths of concrete

Inundation Depth (m)	Boundary of Velocity (m/s)		Tsunami Flow Velocity (m/s)				
	Lower	Upper	15.7 MPa	23.5 MPa	31.4 MPa	39.2 MPa	47.1 MPa
0.24	1.06	3.04	35.55	36.59	37.44	38.17	38.82
0.40	1.39	3.96	21.42	22.05	22.56	23.00	23.39
0.60	1.70	4.85	16.40	16.88	17.27	17.60	17.90
0.80	1.96	5.60	13.79	14.18	14.51	14.79	15.04
1.00	2.19	6.26	12.11	12.46	12.75	12.99	13.21
1.20	2.40	6.86	10.93	11.24	11.50	11.72	11.92
1.40	2.59	7.41	10.03	10.32	10.55	10.76	10.94
1.60	2.77	7.92	9.31	9.58	9.80	9.99	10.16
1.80	2.94	8.40	8.73	8.98	9.19	9.37	9.53
2.00	3.10	8.86	8.24	8.48	8.67	8.84	8.99
2.20	3.25	9.29	7.82	8.04	8.23	8.40	8.58
2.40	3.40	9.70	7.34	7.74	7.91	8.06	8.20
2.57	3.51	10.03	6.89	7.25	7.41	7.56	7.71
2.80	3.67	10.48	6.36	6.64	6.78	6.92	7.06
3.00	3.80	10.85	3.44	3.58	3.66	3.73	3.80
3.20	3.92	11.21	2.63	2.74	2.80	2.85	2.91

7.3 Development of Tsunami Fragility Curve

In this study, the tsunami fragility curve at the collapse damage level is developed for one-story reinforced-concrete building. Fragility curve is represented as a function of the tsunami inundation depth. From Table 7-1 and Table 7-2, the cumulative probabilities of occurrence building collapse can be expressed by equation

7-1. The calculation of the cumulative probabilities of occurrence is listed in Table 7-3. The total number of data suffered damage level is 494.

$$p_{N_h,k} = \frac{1}{n}\sum_{k=1}^{N_h}\sum_{i=1}^{m} N_{f'_c,i} \tag{7-1}$$

where

$p_{N_h,k}$ is the cumulative probabilities of building collapse for each inundation depth,

$N_{f'_c,i}$ is the number of data suffered damage level of each compressive strength of concrete i,

N_h is the number of tsunami inundation depth that buildings suffered damage level,

m is the number of considering compressive strengths of concrete,

n is the total number of data $n = N_h \sum_{i=1}^{m} N_{f'_c,i}$

Table 7-3. Probability of building collapse under tsunami loading

Inundation Depth (m)	$N_{f'_c,i}$ of each Compressive Strength (MPa)					$\sum_{i=1}^{m} N_{f'_c,i}$	$\sum_{k=1}^{N_h}\sum_{i=1}^{m} N_{f'_c,i}$	Cumulative Probability ($p_{N_h,k}$)
	15.7	23.5	31.4	39.2	47.1			
0.24	0	0	0	0	0	0	0	0.000
0.40	0	0	0	0	0	0	0	0.000
0.60	0	0	0	0	0	0	0	0.000
0.80	0	0	0	0	0	0	0	0.000
1.00	0	0	0	0	0	0	0	0.000
1.20	0	0	0	0	0	0	0	0.000
1.40	0	0	0	0	0	0	0	0.000
1.60	0	0	0	0	0	0	0	0.000
1.80	0	0	0	0	0	0	0	0.000
2.00	3	16	52	27	0	98	98	0.198
2.20	3	16	52	27	1	99	197	0.398
2.40	3	16	52	27	1	99	296	0.598
2.57	3	16	52	27	1	99	395	0.798
2.80	3	16	52	27	1	99	494	0.998
3.00	0	0	0	0	1	1	495	1.000
3.20	0	0	0	0	0	0	495	1.000
					Sum	495		

The fragility curve can be expressed in forms of two-parameter lognormal distribution functions which are median and lognormal standard deviation. The lognormal is used because it agrees well with an uncertainty of failure data (Porter et al., 2007). The estimation of these two parameters is done by the maximum likelihood method (Saxena et al., 2000, Shinozuka et al., 2001, Kim and Shinozuka, 2004). The likelihood function can be written as equation 7-2. The fragility curve can be written under the lognormal function, $F(a)$ as expressed in equation 7-3.

$$M = \prod_{k=1}^{N_h} \left[F\left(a_{N_h}\right) \right]^{p_{N_h,k}} \left[1 - F\left(a_{N_h}\right) \right]^{1-p_{N_h,k}} \tag{7-2}$$

$$F(a) = \Phi \left[\frac{\ln\left(\frac{a}{\alpha}\right)}{\beta} \right] \tag{7-3}$$

where

a_{N_h} is the k-th inundation depth,

$p_{N_h,k}$ is the cumulative probability of building damaged of the k-th inundation depth ,

$\Phi(.)$ is the standardized normal distribution function,

N_h is the total number of considering inundation depth,

α , β are median and lognormal standard deviation of inundation depth in unit of meter.

The parameters α and β are computed in order to maximize $\ln(M)$ by differentiating $\ln(M)$ with respect to α and β and equating to zero as equation 7-4.

$$\frac{d \ln M}{d\alpha} = \frac{d \ln M}{d\beta} = 0 \tag{7-4}$$

Equation 7-4 is solved numerically using a standard optimization algorithm. The process starts from substituting the variables $p_{N_h,k}$ and a_{N_h} into the likelihood function in equation 7-2 and then a standard optimization algorithm is used to obtain two parameters α and β. Finally, the variable $p_{N_h,k}$, a_{N_h} and two parameters are used to plot the fragility curve.

From the standard optimization algorithm, median (α) and lognormal standard deviation (β) are 0.8221 and 0.1145, respectively. The variable $p_{N_h,k}$, a_{N_h}, median and lognormal standard deviation are used to plot the fragility curve of building collapse under tsunami loading. The tsunami fragility curve of one-story reinforced-concrete building with break away walls under tsunami loading with damage level of collapse is shown as Figure 7-4 with the cumulative probability in collapse in Table 7-3. The developed tsunami fragility curve shows the collapse occurrence from inundation depth larger than 1.8 m. It is obvious that collapse occurs for inundation depth higher than 3.2 m.

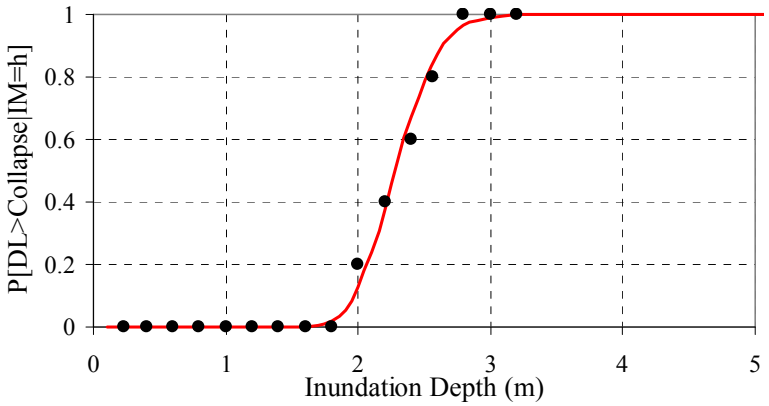

Figure 7-4. Tsunami fragility curve of one-story reinforced-concrete building with break away walls for damage level of collapse

7.4 Discussion on Tsunami Fragility Curve

In Figure 7-5, the developed tsunami fragility curve is compared with the tsunami fragility curves proposed by Foytong and Ruangrassamee (2007), which were developed from observed damage building data in the Southern part of Thailand from the 2004 Indian Ocean tsunami for one-story reinforced-concrete buildings. Three damage levels were considered; damage in secondary members only (Level 1), damage in primary members (Level 2) and collapse (Level 3). Damage Level 1 was defined as there is damage only in non-structural components, i.e., walls and/or roofs. At this damage level, there are cracks on wall or wall punching, or tiles are wiped out, but there is no damage in a beam or a column. Damage Level 2 was defined as there is damage in structural components, i.e., a column, a beam, or a foundation. At this damage level, there are cracks on a beam or a column, but the building is still reparable and it can sustain its gravitational load. Damage Level 3 was defined as a building cannot sustain its gravitational load and it is unreparable.

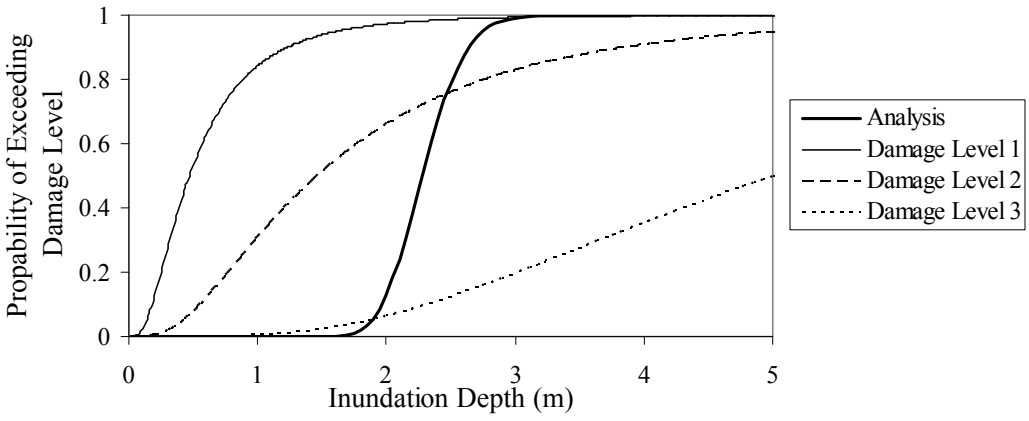

Figure 7-5. Comparison of the analytical fragility curve with the experimental fragility curves proposed by Foytong and Ruangrassamee (2007)

The developed fragility curve lies between Damage Level 2 and Damage Level 3 of the curves from observation. The fragility curve from analysis has probability of damage less than the probability of Damage Level 2. The fragility curve from analysis has probability of damage higher than the probability of damage level 3 (Collapse). The reinforced-concrete building is analyzed with assumption of the break away walls, but buildings in observation have masonry infill walls which enhance the tsunami load resistance of the building. Further study in required to investigate the effect of walls on fragility curves.

CHAPTER VIII
CONCLUSIONS

This research studies on the responses of reinforced-concrete building under tsunami loading and the tsunami fragility curve is developed. Findings can be summarized as follows:

1) After major tsunami events, several researchers reported tsunami heights along coastlines from field survey. However, reported information on tsunami flow velocities on land is scarce. The tsunami flow velocities are estimated from videos during the March 2011 Tohoku, Japan tsunami by estimating movement distances from measured dimensions of objects. The analyzed tsunami flow velocities are about 3 - 5 m/s in Kamaishi City, 2 m/s in Ofunato City, 3 - 6 m/s in Kesennuma City and 1.5 m/s in Iwaki City. Analyzed tsunami flow velocities fall in the range of $1.0\sqrt{gh}$ to $1.5\sqrt{gh}$.

2) The 3-dimensional model of the former office of Thai Meteorological Department is analyzed by using 3-dimensional non-linear static pushover analysis. This building is a one-story reinforced-concrete building suffered the 2004 Indian Ocean tsunami with the inundation depth of 4.4 m. Full scale pushover test of this building was tested by Lukkunaprasit et al. (2010). In the analysis, the fiber model is used to model plastic hinges by separately considering the behaviors of covering concrete, core concrete and steel bar. The shear behavior of columns is considered by using a non-linear spring. The equation proposed by Sezen (2002) is used to model a non-linear shear spring behavior. The masonry infill walls are modeled as a horizontal spring. The horizontal spring model cannot represent the behavior of forces transferred to frame columns that causes the shear failure in frame columns. The equations proposed by Mostafaei and Kabeyasawa (2004) give closer estimates the lateral resistances comparing with the experimental results by Mehrabi et al. (1996). From analysis results, the lateral resistance of building is controlled by the resistance of the masonry infill wall in the middle frame. In the experiment, it was found that cracks on the masonry infill wall in the middle frame significantly widened at the maximum lateral load. The good agreements between the test and analysis are also obtained in terms of initial stiffness and deformations. The model is applied in the analysis of the generic building.

3) The building model developed from the average values of the structural indices of residential houses in Southern Thailand is analyzed for responses under tsunami hydrodynamic forces. At each inundation depth, the tsunami flow velocity is increased until collapse by using the force-controlled method. The collapse point is defined as the point where the shear force reaches shear capacity or concrete reaches its strength. The tsunami force acts on all columns simultaneously. For the inundation depths from 0.24 m to 0.6 m, the lateral resistance of the building is controlled by the shear failure in the corner columns in the back span, because the corner columns shear capacity is the least. The failure mode of the building changes from the shear failure to the flexural failure at an inundation depth of 2.57 m. The lateral resistances controlled by the shear failure are about 258 kN for the inundation depths from 0.24 m to 2.4 m. For the inundation depths from 2.57 m to 3.2 m, the lateral resistances are controlled the flexural failure in the middle column (Column B2). At an inundation depth of 3.2 m, the lateral resistance decreases about 50% from the lateral resistances controlled by the shear failure.

4) From the study on tsunami flow velocity and analysis of tsunami flow velocity from recorded videos, the tsunami flow velocity is considered in the range from $0.7\sqrt{gh}$ to $2.0\sqrt{gh}$. In this the tsunami flow velocity range, the building reaches the collapse point for inundation depth from 2.0 m to 2.8 m. For the tsunami inundation depths of 3.0 m to 3.2 m, the tsunami flow velocities at the collapse point are less than $0.7\sqrt{gh}$.

5) The compressive strength of concrete has slight effects on the failure mode of the building at the same inundation depth. The lateral resistance increases according to the compressive strength. The lateral resistances of the building increase by about 5% - 20% for the shear failure and about 8% - 22% for the flexural failure.

6) The effect of masonry infill walls is investigated. The lateral resistances of the building with masonry infill walls are less than that of the building without masonry infill wall because the areas of loading are reduced. Nevertheless, the tsunami flow velocity at the collapse of the building with masonry infill wall is higher than that of the building without masonry infill walls. As an inundation depth increases, the locations of loads move higher and the effect of masonry infill walls increases. At an inundation depth of 3.2 m that the tsunami reaches the beam level, the lateral resistances represented in terms

of the momentum fluxes for the building with walls provided in both side frames are about twice as large as those without wall. And the momentum fluxes for the building with walls in all frames are about 9 times of those without wall.

7) The analytical tsunami fragility curve for one-story reinforced-concrete building is developed at the collapse damage level by using the maximum likelihood method. The uncertainties are tsunami flow velocities and compressive strengths of concrete. The uncertainty of the tsunami flow velocity is considered in the range from $0.7\sqrt{gh}$ to $2.0\sqrt{gh}$. The developed tsunami fragility curve shows that the building does not collapse for an inundation depth less than 1.8 m and collapses for an inundation depth higher than 3.2 m.

REFERENCES

Anil, O., and Altin, S. (2007). An experimental study on reinforced concrete partially infill frames. Engineering Structures 29 : 449-460.

ACI-214R. (2002). Evaluation of Strength Test Results of Concrete, American Concrete Institute, Detroit.

Ark Information System Co. Ltd. (2008). TDAP3 Reference Manual, V2.10. (In Japanese)

Asakura, R., et al. (2002). The tsunami wave force acting on land structures. Proceedings of the 28th International Conference on Coastal Engineering, Cardiff, Wales : 1191-1202.

ASTM C 1314-03b. (2003). Standard Test Method for Compressive Strength of Masonry Prisms, American Society for Testing and Materials, Pennsylvania, United States.

Bapat, A., and Murty, T. (2008). Field survey of the December 26, 2004 tsunami at Kanyakumari, India. Science of Tsunami Hazards 27(3) : 72-86.

Carrier, G.F., Wu, T.T., and Yeh, H. (2003). Tsunami runup and draw-down on a plane beach. Journal of Fluid Mechanics 475 : 79-99.

CCH. (2000). Department of Planning and Permitting of Honolulu Hawaii, City and County of Honolulu Building Code 16(11), Honolulu, Hawaii.

CEEEV. (2005). Database of Structural Damage [Online]. Available from : http://evr.eng.chula.ac.th/earthquake/DamageSurvey/view.asp [2009, August 25]

Cross, R.H. (1967). Tsunami surge forces. Journal of the Waterways and Harbors Division, ASCE 4 : 201-231.

CU. (2007). Analysis and Development of the Appropriate Design Guideline for Evacuation Shelters and Public Buildings in the Moderate Tsunami Hazard Zone, Chulalongkorn Unversity, Bangkok, Thailand. (In Thai)

Dias, W.P.S., Yapa, H.D., and Peiris, L.M.N. (2009). Tsunami vulnerability functions from field surveys and Monte Carlo simulation. Civil Engineering and Environmental Systems 26(2) : 181-194.

DPRI. (2006). 2004 Indian Ocean tsunami disaster survey report, Disaster Prevention Research Institute, Kyoto University, Japan.

EERI. (2011). The Tohoku, Japan, Tsunami of March 11, 2011: Effects on Structures, Earthquake Engineering Research Institute, Washington, D.C.

FEMA 55. (2000). Coastal Construction Manual Edition 3, Federal Emergency Management Agency, Washington, D.C.

FEMA 306. (1998). Evaluation of Earthquake Damaged Concrete and Masonry Wall Buildings - Basic Procedures Manual, Federal Emergency Management Agency, Washington, D.C.

FEMA 356. (2000). Prestandard and Commentary for the Seismic Rehabilitation of Buildings, Federal Emergency Management Agency, Washington, D.C.

FEMA P646. (2008). Guidelines for Design of Structures for Vertical Evacuation from Tsunamis, Federal Emergency Management Agency, Washington, D.C.

Foytong, P., and Ruangrassamee, A. (2007). Fragility curves of reinforced-concrete buildings damaged by a tsunami for tsunami risk analysis. Proceedings of the 20th KKCNN Symposium Civil Engineering, Jeju, Korea S8 : 47-52.

Fritz, H.M., Borrero, J.C., Synolakis, C.E., and Yoo, J. (2006). 2004 Indian Ocean tsunami flow velocity measurements from survivor videos. Geophysical Research Letters 33(L24605).

Fritz, H.M., et al. (2012). The 2011 Japan tsunami current velocity measurements from survivor videos at Kesennuma Bay using LiDAR. Geophysical Research Letters 39(L00G23).

Ghobarah, A., Aly, N.M., and El-Attar M. (1997). Performance level criteria and evaluation. Proceedings of the International Workshop on Seismic Design Methodologies for the next Generation of Codes, Balkema, Rotterdam : 207–215.

Gomes, A., and Appleton, J. (1997). Nonlinear cyclic stress-strain relationship of reinforcing bars including buckling. Engineering Structures 19(10) : 822-826.

Google Earth. (2010). Google Earth [Online]. Available from : http://earth.google.com/tour.html [2011, November 10]

Hamzah, M.A., Mase, H., and Takayama, T. (2000). Simulation and experiment of hydrodynamic pressure on a tsunami barrier. Proceedings of the 27th International Conference on Coastal Engineering, Sydney, Australia : 1501-1507.

Hoshikuma, J., Kawashima, K., Nagaya, K., and Taylor, A.W. (1997). Stress-strain model for confined reinforced concrete in bridge piers. Journal of the Structural Engineering, ASCE 123(5) : 624-633.

JMA. (2011). The 2011 off the Pacific Coast of Tohoku Earthquake, Japan Meteorological Agency, Japan, Tokyo, Japan.

Kakaletsis, D.J., and Karayannis, C.G. (2008). Influence of masonry strength and openings on infilled R/C frames under cycling loading. Journal of Earthquake Engineering 12 : 197-221.

Karim, K.R., and Yamazaki, F. (2001). Effect of earthquake ground motions on fragility curves of highway bridge piers based on numerical simulation. Earthquake Engineering and Structural Dynamics 30 : 1839-1856.

Kent, D., and Park, R. (1971). Flexural member with confined concrete. Journal of the Structural Division, ASCE 97 : 1969-1990.

Kim, S.H., and Shinozuka, M. . (2004). Development of fragility curves of bridges retrofitted by column jacketing. Probabilistic Engineering Mechanics 19 : 105-112.

Kircil, M.S., and Polat, Z. (2006). Fragility analysis of mid-rise RC frame buildings. Engineering Structures 28 : 1335-1345.

Koshimura, S., Oie, T., Yanagisawa, H., and Imamura, F. (2009). Developing fragilitiy functions for tsunami damage estimation using numerical model and

post-tsunami data from Banda Aceh, Indonesia. Coastal Engineering Journal 3 : 243-273.

Koshimura, S., and Hayashi, S. (2012). Interpretation of tsunami flow characteristics by video analysis. 9thCUEE&4thACEE Joint Conference Proceeding, Tokyo, Japan.

Lee, B.J., Chou, T.Y., Hsiao, C.P., Chung, L.K., Huang, P.H., and Wu, Y.B. (2001). The statistics and analysis of building damage on Chi-Chi earthquake. Host 130 by National Center for Research on Earthquake Engineering : 166-178.

Lukkunaprasit, P., Thanasisathit, N., and Yeh, H. (2009). Experimental verification of FEMA P646 tsunami loading. Journal of Disaster Research 4 : 45-53.

Lukkunaprasit, P., Ruangrassamee, A., Stitmannaithum, B., Chintanapakdee, C., and Thanasisathit, N. (2010). Calibration of tsunami loading on a damage building. Journal of Earthquake and Tsunami 4(2) : 105-114.

Mander, J.B., Priestley, M.J.N., and Park, R. (1988). Theoretical stress-strain model for confined concrete. Journal of the Structural Engineering, ASCE 114(8) : 1804-1849.

Matsutomi, H., and Okamoto, K. (2010). Inundation flow velocity of tsunami on land. Island Arc 19 : 443-457.

Matsutomi, H., Sakakiyama, T., Nugroho, S., and Matsuyama, M. (2006). Aspects of inundated flow due to the 2004 Indian Ocean tsunami. Coastal Engineering Journal 48(2) : 167-195.

Mehrabi, A.B., Shing, P.B., Schuller, M.P., and Noland, J.L. (1996). Experimental evaluation of masonry-infilled RC frames. Journal of Structural Engineering 122 : 228-237.

Menegotto, M., and Pinto, P.E. (1973). Method of analysis for cyclically loaded RC plane frames including changes in geometry and non-elastic behavior of elements under combined normal force and bending. Proceedings of IABSE Symposium on Resistance and Ultimate Deformability of Structures Acted on by Well defined Repeated Loads, Lisbon, Portugal 13.

Mostafaei, H., and Kabeyasawa, T. (2004). Effect of infill masonry walls on the seismic response of reinforced concrete buildings subjected to the 2003 Bam Earthquake strong motion: A case study of Bam telephone center. Bulletin Earthquake Research Institute University of Tokyo 79 : 133-156.

Okada, T., Sugano, T., Ishikawa, T., Ohgi, T., Takai, S., and Hamabe, C. (2005). Structural design method of buildings for tsunami resistance (proposed). Building Technology Research Institute, Building Centre for Japan.

Papadopoulos, G.A., and Imamura, F. (2001). Proposal for a new tsunami intensity scale. Proceedings of the 20th International Tsunami Conference, Seattle : 569-577.

Park, Y.J., and Ang, A.H-S. (1985). Seismic damage analysis of reinforced concrete buildings. Journal of Structural Engineering, ASCE 111(4) : 740 –757.

Paulay, T., and Priestley, M. J. N. (1992). Seismic Design of Reinforced Concrete and Masonry Buildings, New York : John Wiley and Sons, Inc.

Porter, K., Kennedy, R., and Bachman, R. (2007). Creating fragility functions for performance-based earthquake engineering. Earthquake Spectra 23 : 471-489.

Ramsden, J.D. (1996). Tsunamis forces on a vertical wall caused by long waves, bores, and surge on a dry bed. Journal of Waterway, Port, Coastal, and Ocean Engineering 122(3) : 134-141.

Ramsden, J.D., and Raichlen, F. (1990). Forces on vertical wall caused by incident bores. Journal of Waterway, Port, Coastal, and Ocean Engineering 116(5) : 592-613.

Reese, S., Cousins, W.J., Power, W.L., Palmer, N.G., Tejakusuma, I.G., and Nugrahadi, S. (2007). Tsunami vulnerability of buildings and people in South Java field observations after the July 2006 Java tsunami. Natural Hazards and Earth System Sciences 7 : 573-589.

Rossetto, T., et al. (2007). The Indian ocean tsunami of December 26 2004 observations in Sri Lanka and Thailand. Natural Hazards 42 : 105-124.

Saatcioglu, M., Ghobarah, A., and Nistor, I. (2005). The December 26 2004 Sumatra Earthquake and Tsunami, Reconnaissance Report, CAEE, ACGP.

Saxena, V., Deodatis, G., Shinozuka, M., and Feng, M.Q. (2000). Development of fragility curves for multi-span reinforced concrete bridges. Department of Civil and Environmental Engineering, Princeton University, Princeton, United States.

Sezen, H. (2002). Seismic behavior and modeling of reinforced concrete building columns. PhD thesis, Dept. of Civil and Environmental Engineering, University of California at Berkeley, Berkeley, Calif.

Shinozuka, M., Feng, M.Q., Kim, H., Uzawa, T., and Ueda, T. (2001). Statistical analysis of fragility curves. Technical report MCEER, Department of Civil and Environmental Engineering, University of Southern California, Los Angeles, California.

Shoji, G., and Moriyama, T. (2007). Evaluation of the structural fragility of a bridge structure subjected to a tsunami wave load. Journal of Natural Disaster Science 29 : 73-81.

Shuto, N. (1993). Tsunami intensity and disasters. Tsunamis in the World, Edited by Tinti S., Kluwer Academic Publishers, Dordrecht : 197-216.

Su, C.H., and Mirie, R.M. (1980). On head-on collisions between two solitary waves. Journal of Fluid Mechanics 98(3) : 509-525.

Suppasri, A., Koshimura, S., and Imamura, F. (2011). Developing tsunami fragility curves based on the satellite remote sensing and the numerical modeling of the 2004 Indian Ocean tsunami in Thailand. Natural Hazards and Earth System Sciences 11(1) : 173–189.

Tantala, M.T., and Deodatis, G. (2002). Development of seismic fragility curves for tall buildings. 15th ASCE Engineering Mechanics Conference, Columbia University, New York.

The 2011 Tohoku Earthquake Tsunami Joint Survey Group. (2011). Nationwide field survey of the 2011 off the Pacific coast of Tohoku earthquake tsunami. JSCE 67(1) : 63-66.

Tsuji, Y., et al. (2006). The 2004 Indian tsunami in Thailand: Surveyed runup heights and tide gauge records. Earth Planets Space 58 : 223-232.

USGS. (2004). Magnitude 9.1 - Off the West Coast of Northern Sumatra [Online]. Available from : http://earthquake.usgs.gov/earthquakes/eqinthenews/2004/us2004slav/#details [2010, April 21]

USGS. (2009). Magnitude 8.1 - Samoa Islands Region [Online]. Available from : http://earthquake.usgs.gov/earthquakes/recenteqsww/Quakes/us2009mdbi.php [2010, April 21]

USGS. (2011). Magnitude 9.0 - Near the East Coast of Honshu, Japan [Online]. Available from : http://earthquake.usgs.gov/earthquakes/recenteqsww/Quakes/us2010tfan.php [2012, June 10]

Wehbe, N. I., Saiidi, M. S., and Sanders, D. H. (1999). Seismic performance of rectangular bridge columns with moderate confinement. ACI Structural Journal 96(2) : 248-259.

Yamazaki, F., Onishi, J., and Tayama, S. (1999). Earthquake damage assessment of expressway structures in Japan. *Asian-Pacific Symposium on Structural Reliability and its Applications*, Taipei, Taiwan, R.O.C.

Yamazaki, F., and Murao, O. (2000). Fragility curves for buildings in Japan based on experience from the 1995 Kobe Earthquake. Institute of Industrial Science, University of Tokyo, Tokyo, Japan.

Yeh, H. (2006). Maximum fluid forces in the tsunami runup zone. Journal of Waterway, Port, Coastal, and Ocean Engineering 132(6) : 496-500.

Yeh, H. (2007). Design tsunami forces for onshore structures. Journal of Disaster Research 2(6) : 531-536.

Yi, J.H., Kim, S.H., and Kushiyama, S. (2007). PDF interpolation technique for seismic fragility analysis of bridges. Engineering Structures 29 : 1312-1322.

APPENDICES

Appendix A
Stress and Strain Relationship of Reinforcement

A.1 Stress and strain relationship of reinforcement with a diameter of 12 mm

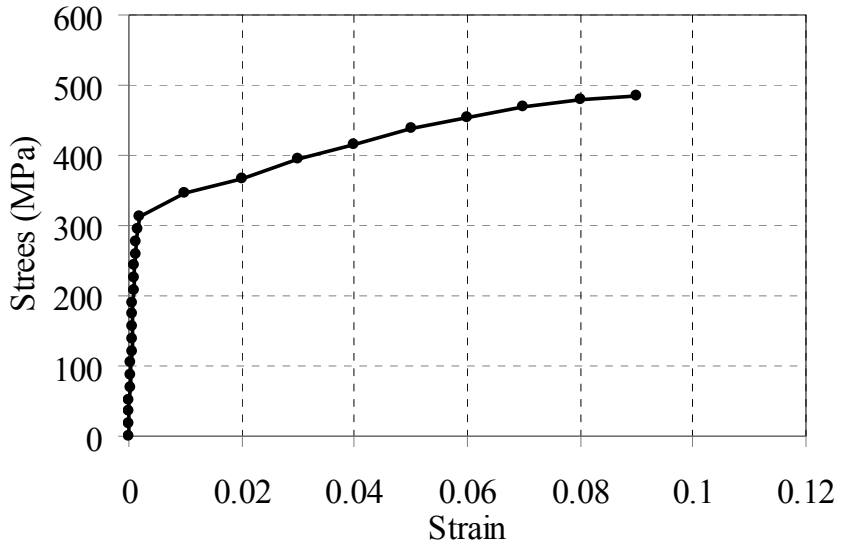

Figure A-1. Stress and strain relationship of the sample No.1 of the reinforcement with a diameter of 6 mm

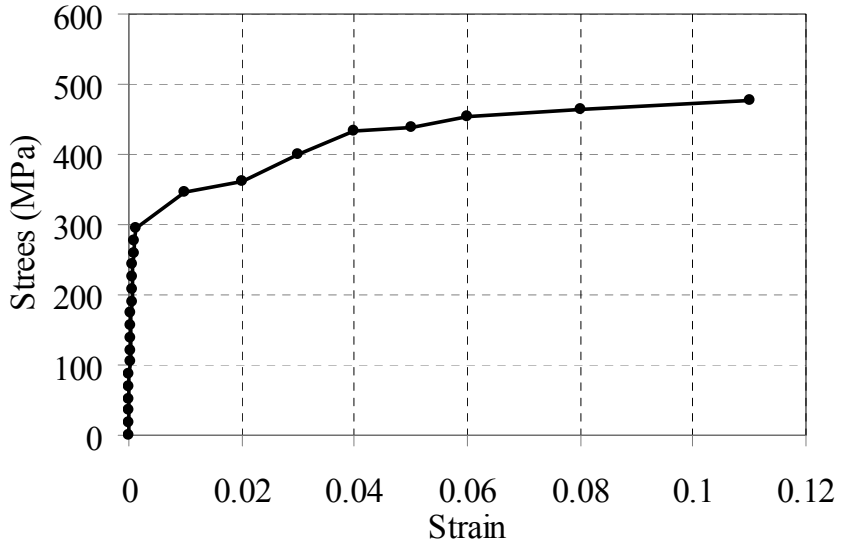

Figure A-2. Stress and strain relationship of the sample No.2 of the reinforcement with a diameter of 6 mm

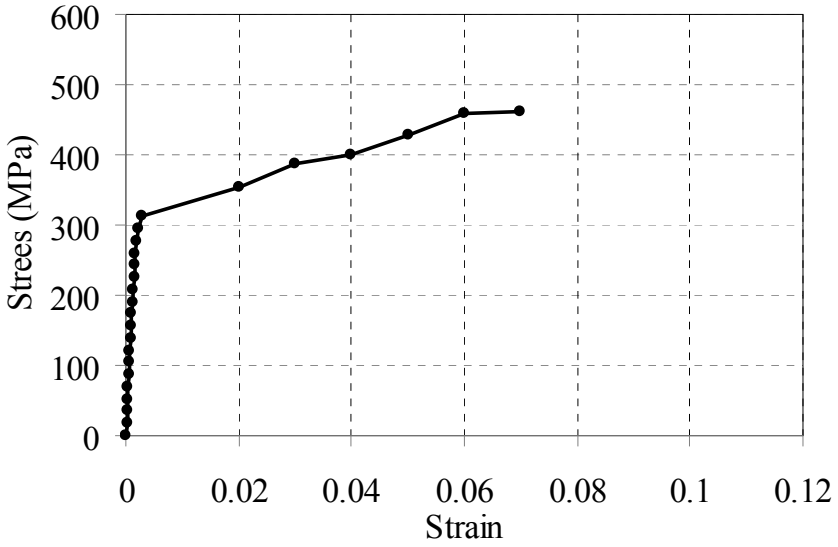

Figure A-3. Stress and strain relationship of the sample No.3 of the reinforcement with a diameter of 6 mm

A.2 Stress and strain relationship of reinforcement with a diameter of 12 mm

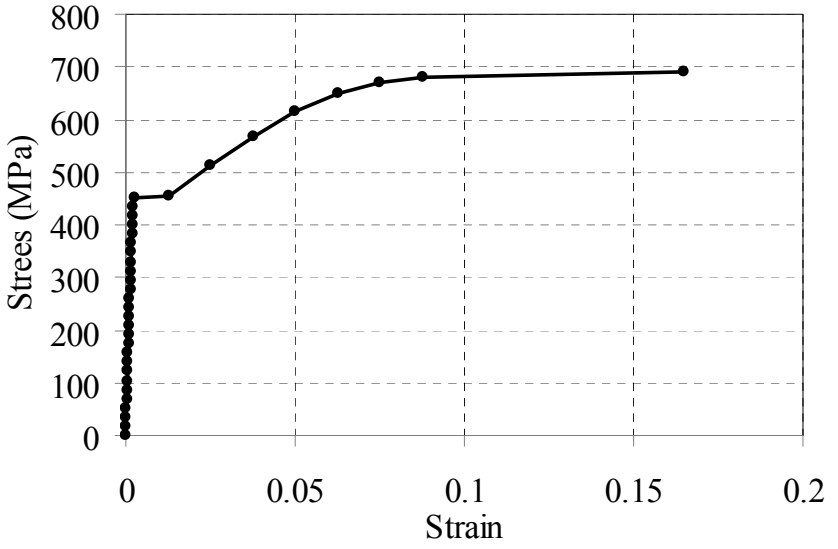

Figure A-4. Stress and strain relationship of the sample No.1 of the reinforcement with a diameter of 12 mm

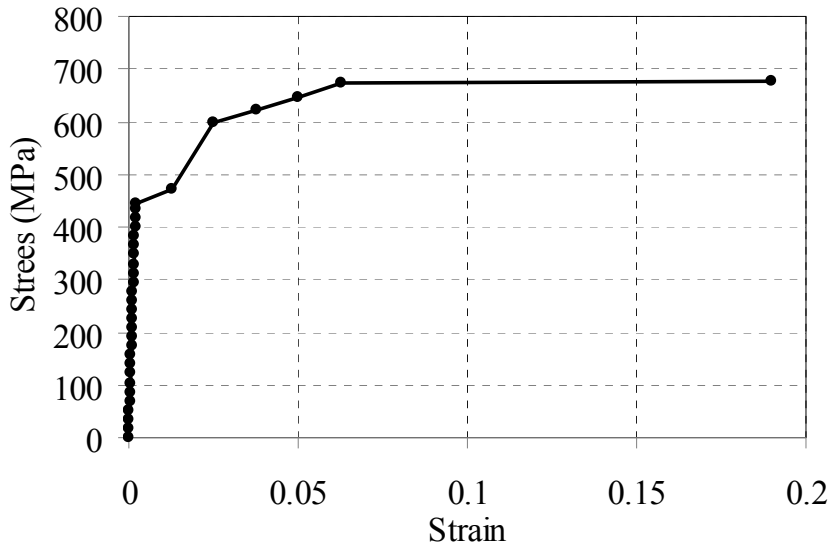

Figure A-5. Stress and strain relationship of the sample No.2 of the reinforcement with a diameter of 12 mm

A.3 Stress and strain relationship of reinforcement with a diameter of 16 mm

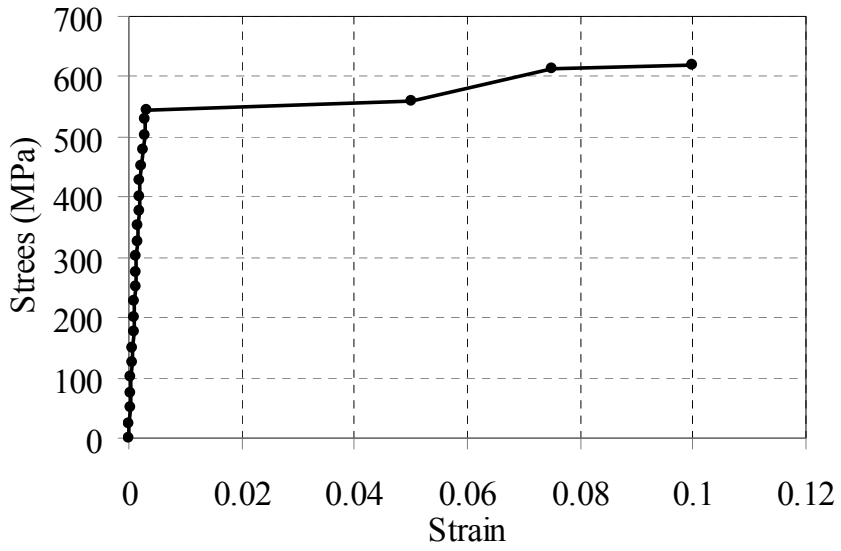

Figure A-6. Stress and strain relationship of the sample No.1 of the reinforcement with a diameter of 16 mm

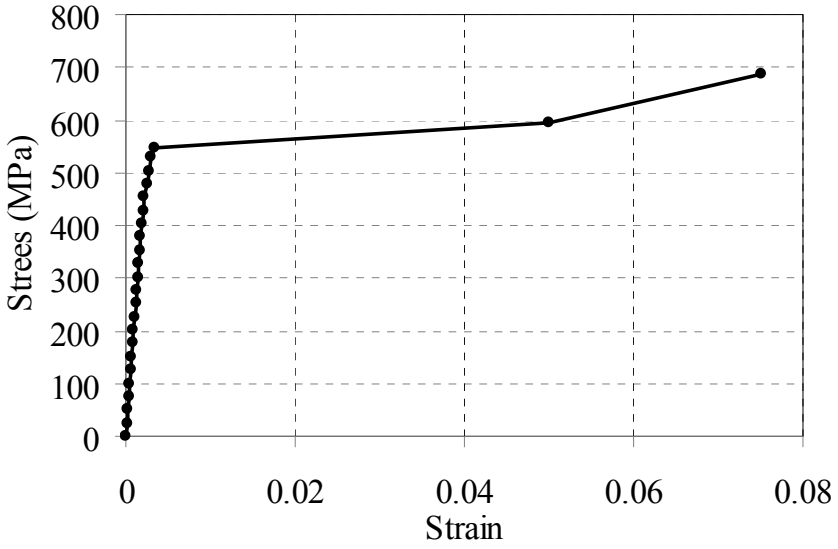

Figure A-7. Stress and strain relationship of the sample No.2 of the reinforcement with a diameter of 16 mm

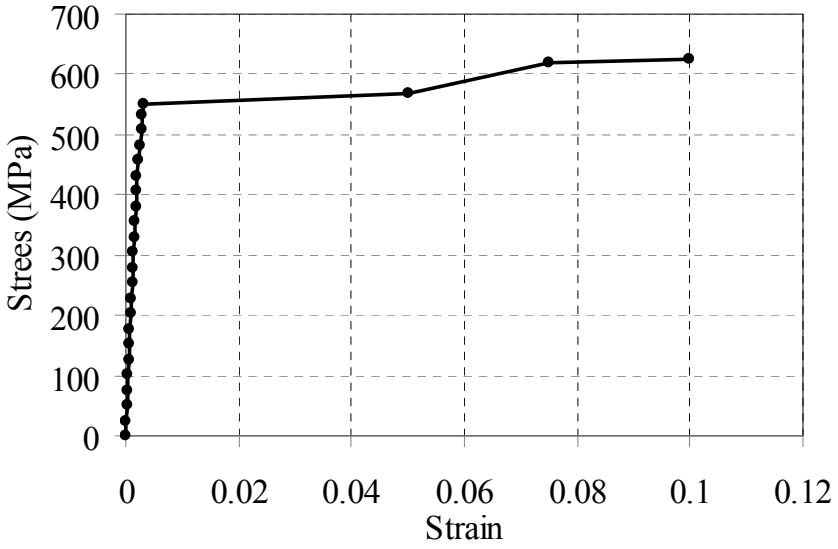

Figure A-8. Stress and strain relationship of the sample No.3 of the reinforcement with a diameter of 16 mm

Appendix B
Building Responses of Various Compressive Strengths of Concrete

B.1 The responses of building with the compressive strength of 15.7 MPa

The analytical results with maximum load resistances, maximum displacement and location, and failure mode of the compressive strength of 15.7 MPa for each inundation depth are listed in Table B-1. Relationship of force and maximum roof displacement under all inundation depths is shown in Figure B-1. The maximum resistances of the building slightly increase from 244.9 kN to 245.2 kN for the inundation depths of 0.24 m to 0.6 m. The lateral resistance of the building is controlled by the shear failure in Columns A3 and C3. The Columns A3 and C3 have the least shear capacity.

Table B-1. Maximum load resistances, maximum displacement and location, and failure mode of the compressive strength of 15.7 MPa

No.	Inundation Depth (m)	Max. Load (kN)	Max. Displacement		Failure mode
			(mm)	Location	
1	0.24	244.9	5.6	Col A3, C3	Shear failure in Columns A3 and C3
2	0.40	245.0	6.2	Col A3, C3	Shear failure in Columns A3 and C3
3	0.60	245.2	7.4	Col A3, C3	Shear failure in Columns A3 and C3
4	0.80	245.2	9.0	Col A3, C3	Shear failure in Columns A2 and C2
5	1.00	244.7	10.6	Col A3, C3	Shear failure in Columns A2 and C2
6	1.20	244.2	12.4	Col A3, C3	Shear failure in Columns A2 and C2
7	1.40	243.6	14.3	Col A3, C3	Shear failure in Columns A2 and C2
8	1.60	243.0	16.3	Col A3, C3	Shear failure in Columns A2 and C2
9	1.80	242.5	19.2	Col A3, C3	Shear failure in Columns A2 and C2
10	2.00	241.5	23.8	Col A3, C3	Shear failure in Columns A2 and C2
11	2.20	240.4	28.5	Col A3, C3	Shear failure in Columns A2 and C2
12	2.40	232.1	31.0	Col A3, C3	Flexural failure in Column B2
13	2.57	219.9	30.8	Col A3, C3	Flexural failure in Column B2
14	2.80	204.8	30.7	Col A3, C3	Flexural failure in Column B2
15	3.00	136.1	32.2	Col B3	Flexural failure in Column B2
16	3.20	124.0	32.9	Col B3	Flexural failure in Column B2

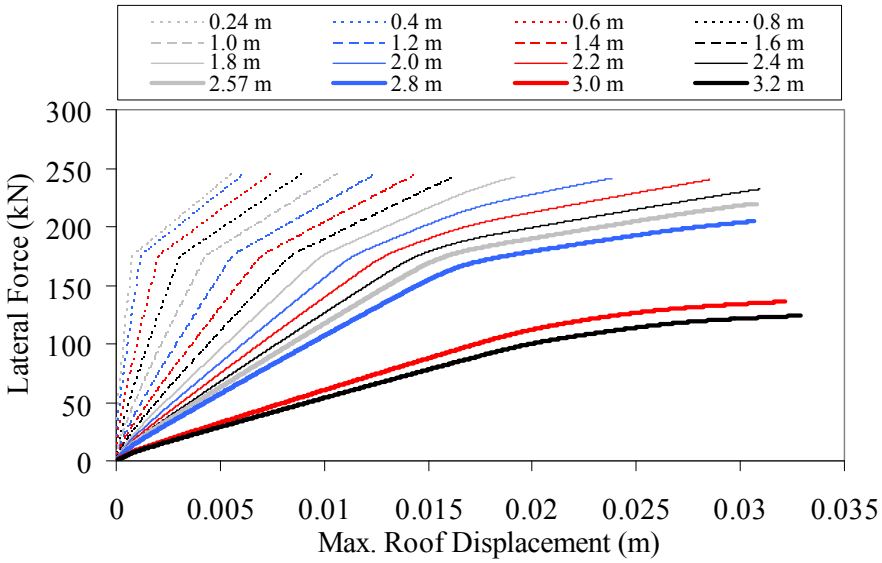

Figure B-1. Force and maximum roof displacement under tsunami of the compressive strength of 15.7 MPa

From tsunami inundation depths of 0.8 m to 2.2 m, the lateral resistances of the building are linearly decreasing from 245.2 kN to 240.4 kN, which are controlled by the shear failure in Columns A2 and C2. At this stage, the load is shared between the columns in each frame, so the shear failure occurs in the middle column of the left and right frames. As shown in Figure B-2, the flexural moment of Column B2 is significantly increased. The stress of covering concrete in Column B2 is larger than 14 MPa at an inundation depth of 1.8 m as shown in Figure B-3. The longitudinal reinforcement in Column B2 yields at an inundation depth of 1.8 m as shown in Figure B-4. Under an inundation depth of 2.2 m, the flexural failure closely occurs.

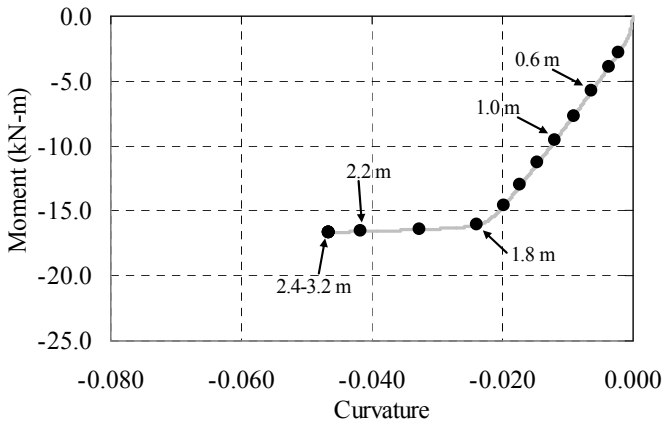

Figure B-2. Moment and curvature relationship of Column B2 under all inundation depths of the compressive strength of 15.7 MPa

The failure mode of the building changes from a shear failure to a flexure failure in Column B2 at an inundation depth of 2.4 m with the lateral resistance of 232.1 kN. For inundation depths of 2.57 m to 3.2 m, the lateral resistances are controlled by the flexural failure in Column B2. The maximum resistances of building are decreased according to inundation depth from 219.9 kN to 124.0 kN due to changing of failure mode. At inundation depths of 3.0 m and 3.2, tsunami acts on the roof beams, then the flexural failure occurs rapidly. The maximum resistance decreases significantly. Shear forces in columns are about 14.5 kN.

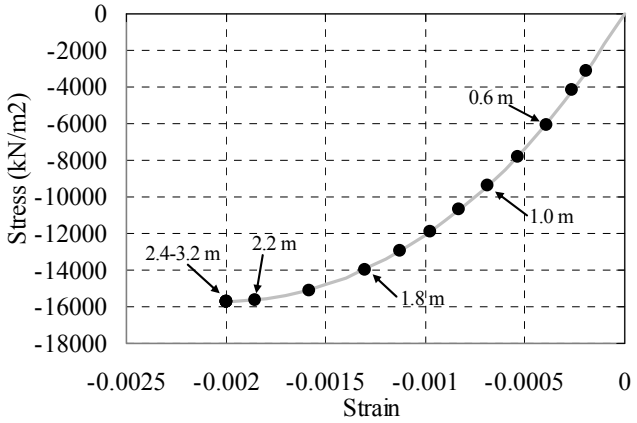

Figure B-3. Stress-strain relationship of covering concrete of Column B2 under all inundation depths of the compressive strength of 15.7 MPa

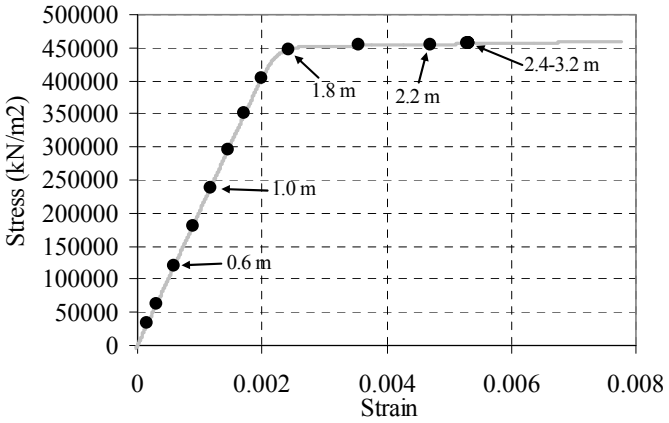

Figure B-4. Stress-strain relationship of reinforcement of Column B2 under all inundation depths of the compressive strength of 15.7 MPa

B.2 The responses of building with the compressive strength of 31.4 MPa

The analytical results with maximum load resistances, maximum displacement and location, and failure mode of the compressive strength of 31.4 MPa for each inundation depth are listed in Table B-2. Relationship of force and maximum roof displacement under all inundation depths is shown in Figure B-5. The maximum resistances of building slightly increase from 271.5 kN to 271.9 kN for the inundation depths of 0.24 m to 0.6 m. The lateral resistance of building is controlled by the shear failure in Columns A3 and C3. The Columns A3 and C3 have the least shear capacity.

From inundation depths of 0.8 m to 2.2 m, the lateral resistances of building are linearly decreasing from 271.5 kN to 266.8 kN, which are controlled by the shear failure in Columns A2 and C2. At this stage, the load is shared between the columns in each frame, so the shear failure occurs in the middle column of the left and right frames. As shown in Figure B-6, the flexural moment of Column B2 is significantly increased. The stress of covering concrete in Column B2 is larger than 25 MPa at an inundation depth of 2.2 m as shown in Figure B-7. The longitudinal reinforcement in Column B2 yields at an inundation depth of 1.8 m as shown in Figure B-8. Under an inundation depth of 2.4 m, the lateral resistance slightly increases to 270.1 kN. The shear failure of Column B3 controls the lateral resistance of building. From the stress-strain of covering concrete in Column B2, the flexural failure closely occurs.

Table B-2. Maximum load resistances, maximum displacement and location, and failure mode of the compressive strength of 31.4 MPa

No.	Inundation Depth (m)	Max. Load (kN)	Max. Displacement		Failure mode
			(mm)	Location	
1	0.24	271.5	5.4	Col A3, C3	Shear failure in Columns A3 and C3
2	0.40	271.7	6.0	Col A3, C3	Shear failure in Columns A3 and C3
3	0.60	271.9	7.3	Col A3, C3	Shear failure in Columns A3 and C3
4	0.80	271.6	8.7	Col A3, C3	Shear failure in Columns A2 and C2
5	1.00	271.0	10.2	Col A3, C3	Shear failure in Columns A2 and C2
6	1.20	270.5	11.8	Col A3, C3	Shear failure in Columns A2 and C2
7	1.40	269.9	13.5	Col A3, C3	Shear failure in Columns A2 and C2
8	1.60	269.3	15.4	Col A3, C3	Shear failure in Columns A2 and C2
9	1.80	268.5	18.6	Col A3, C3	Shear failure in Columns A2 and C2
10	2.00	267.4	22.7	Col A3, C3	Shear failure in Columns A2 and C2
11	2.20	266.8	27.0	Col A3, C3	Shear failure in Columns A2 and C2
12	2.40	270.1	44.2	Col A3, C3	Shear failure in Column B3
13	2.57	254.1	47.1	Col A3, C3	Flexural failure in Column B2
14	2.80	233.3	46.9	Col A3, C3	Flexural failure in Column B2
15	3.00	153.7	47.4	Col B3	Flexural failure in Column B2
16	3.20	140.1	47.9	Col B3	Flexural failure in Column B2

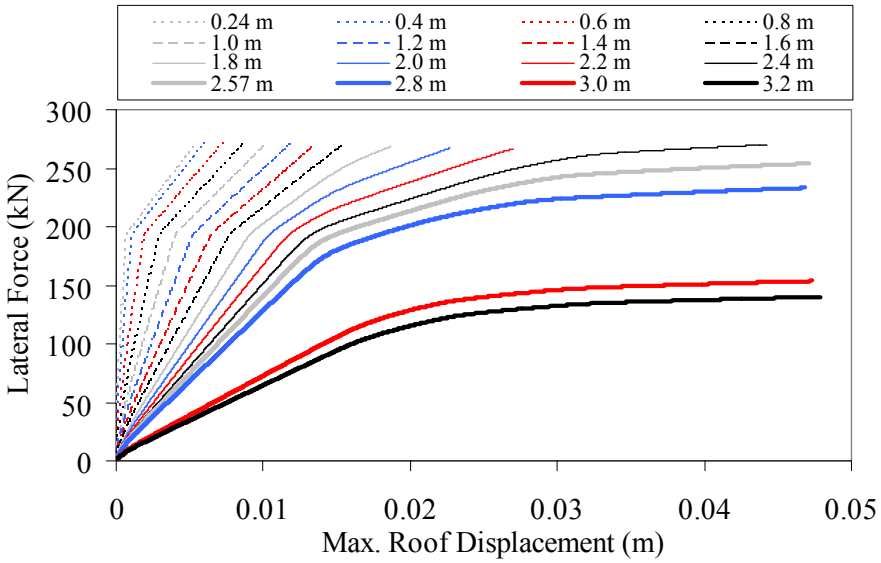

Figure B-5. Force and maximum roof displacement under tsunami of the compressive strength of 31.4 MPa

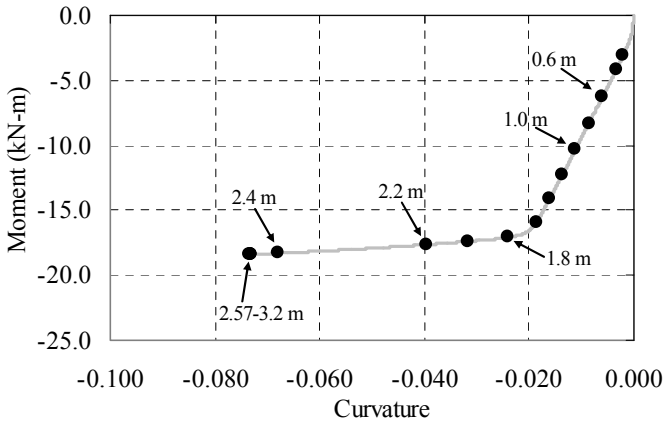

Figure B-6. Moment and curvature relationship of Column B2 under all inundation depths of the compressive strength of 31.4 MPa

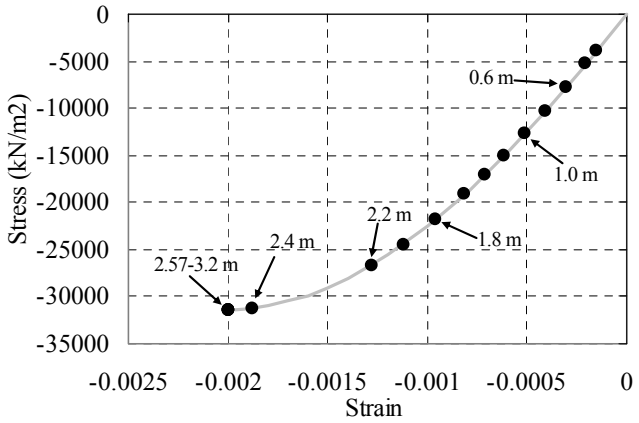

Figure B-7. Stress-strain relationship of covering concrete of Column B2 under all inundation depths of the compressive strength of 31.4 MPa

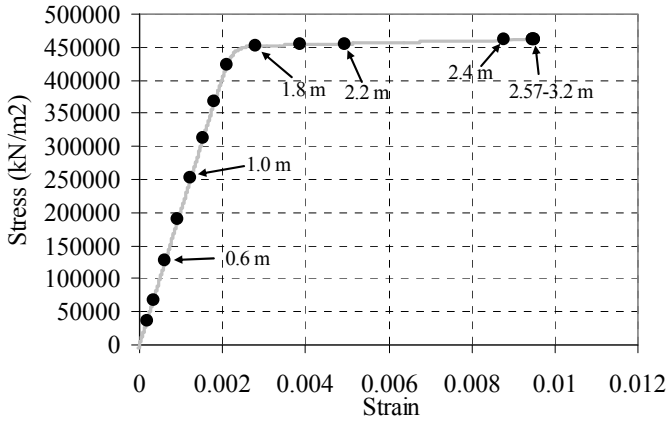

Figure B-8. Stress-strain relationship of reinforcement of Column B2 under all inundation depths of the compressive strength of 31.4 MPa

The failure mode of building changes from a shear failure to a flexure failure in Column B2 at an inundation depth of 2.57 m with the lateral resistance of 254.1 kN. For tsunami inundation depths of 2.8 m to 3.2 m, the lateral resistances are controlled by the flexural failure in Column B2. The maximum resistance of building is decreased according to inundation depths from 233.3 kN to 140.1 kN due to changing of failure mode. At tsunami inundation depths of 3.0 m and 3.2, tsunami acts on the roof beams, then the flexural failure occurs rapidly. The maximum resistance decreases significantly. Shear forces in columns are about 16.3 kN.

B.3 The responses of building with the compressive strength of 39.2 MPa

The analytical results with maximum load resistances, maximum displacement and location, and failure mode of the compressive strength of 39.2 MPa for each inundation depth are listed in Table B-3. Relationship of force and maximum roof displacement under all inundation depths is shown in Figure B-9. The maximum resistances of the building slightly increase from 282.2 kN to 282.4 kN for the inundation depths of 0.24 m to 0.4 m. The lateral resistance of the building is controlled by the shear failure in Columns A3 and C3. The Columns A3 and C3 have the least shear capacity.

Table B-3. The maximum load resistances, the maximum displacement and location, and failure mode of the compressive strength of 39.2 MPa

No.	Inundation Depth (m)	Max. Load (kN)	Max. Displacement		Failure mode
			(mm)	Location	
1	0.24	282.2	5.4	Col A3, C3	Shear failure in Columns A3 and C3
2	0.40	282.4	6.0	Col A3, C3	Shear failure in Columns A3 and C3
3	0.60	282.6	7.3	Col A3, C3	Shear failure in Columns A2 and C2
4	0.80	282.1	8.7	Col A3, C3	Shear failure in Columns A2 and C2
5	1.00	281.6	10.2	Col A3, C3	Shear failure in Columns A2 and C2
6	1.20	281.0	11.8	Col A3, C3	Shear failure in Columns A2 and C2
7	1.40	280.4	13.5	Col A3, C3	Shear failure in Columns A2 and C2
8	1.60	279.8	15.4	Col A3, C3	Shear failure in Columns A2 and C2
9	1.80	278.9	18.9	Col A3, C3	Shear failure in Columns A2 and C2
10	2.00	277.7	22.8	Col A3, C3	Shear failure in Columns A2 and C2
11	2.20	277.8	27.5	Col A3, C3	Shear failure in Column B2
12	2.40	280.4	50.7	Col A3, C3	Shear failure in Column B3
13	2.57	264.4	54.8	Col A3, C3	Flexural failure in Column B2
14	2.80	242.7	54.5	Col A3, C3	Flexural failure in Column B2
15	3.00	159.7	54.7	Col B3	Flexural failure in Column B2
16	3.20	145.6	55.2	Col B3	Flexural failure in Column B2

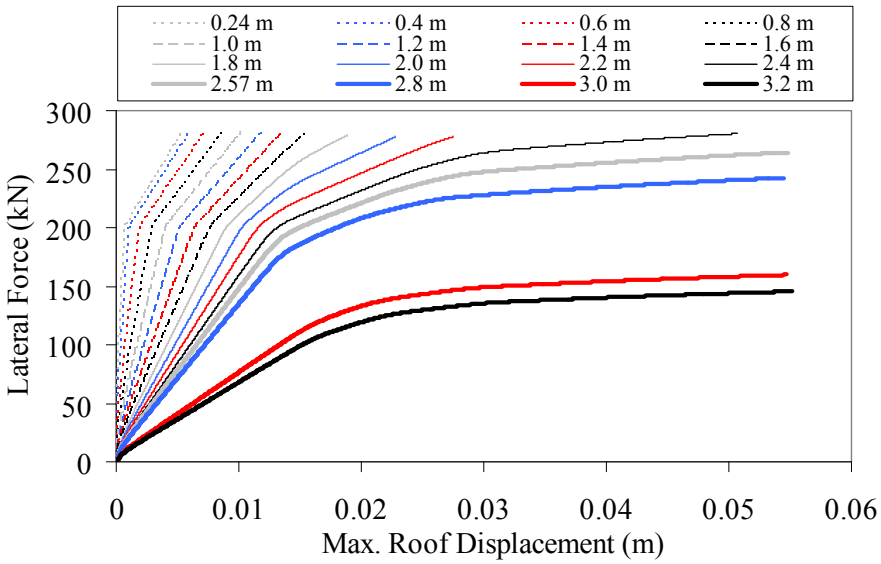

Figure B-9. Force and maximum roof displacement under tsunami of the compressive strength of 39.2 MPa

From tsunami inundation depths of 0.6 m to 2.0 m, the lateral resistances of the building are linearly decreasing from 282.5 kN to 277.8 kN, which are controlled by the shear failure in Columns A2 and C2. At this stage, the load is shared between the columns in each frame, so the shear failure occurs in the middle column of the left and right frames. As shown in Figure B-10, the flexural moment of Column B2 is significantly increased. The stress of covering concrete in Column B2 is larger than 30 MPa at an inundation depth of 2.2 m as shown in Figure B-11. The longitudinal reinforcement in Column B2 yields at an inundation depth of 1.8 m as shown in

Figure B-12. Under inundation depths of 2.2 m and 2.4 m, the shear failure of Columns B2 and B3 control the lateral resistance, respectively. The lateral resistances slightly increase from 277.8 kN to 280.4 kN. From the stress-strain of covering concrete in Column B2, the flexural failure closely occurs

The failure mode of the building changes from a shear failure to a flexure failure in Column B2 at an inundation depth of 2.57 m with the lateral resistance of 264.4 kN. For inundation depths of 2.8 m to 3.2 m, the lateral resistances are controlled by the flexural failure in Column B2. The maximum resistances of building decrease according to inundation depth from 242.7 kN to 145.6 kN due to changing of failure mode. At inundation depths of 3.0 m and 3.2, tsunami acts on the roof beams, then the flexural failure occurs rapidly. The maximum resistance decreases significantly. Shear forces in columns are about 17.0 kN.

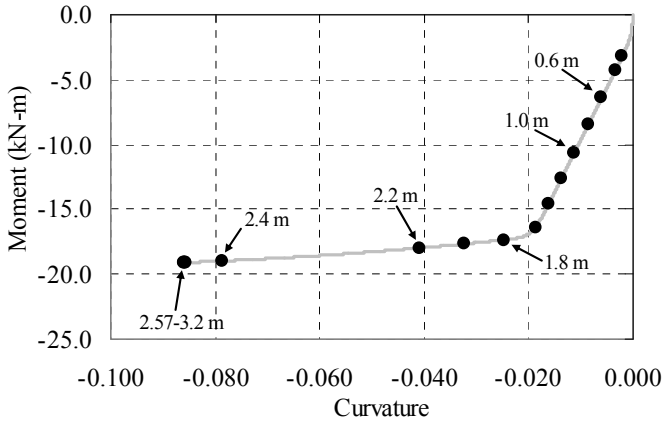

Figure B-10. Moment and curvature relationship of Column B2 under all inundation depths of the compressive strength of 39.2 MPa

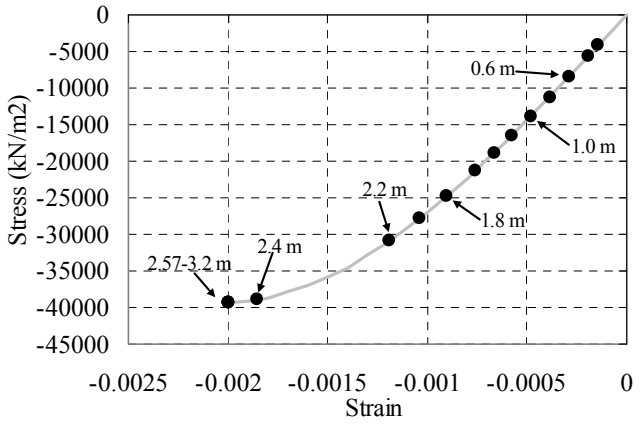

Figure B-11. Stress-strain relationship of covering concrete of Column B2 under all inundation depths of the compressive strength of 39.2 MPa

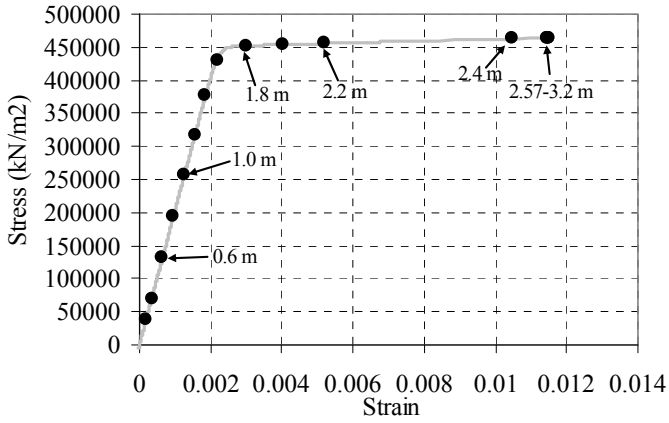

Figure B-12. Stress-strain relationship of reinforcement of Column B2 under all inundation depths of the compressive strength of 39.2 MPa

B.4 The responses of building with the compressive strength of 47.1 MPa

The analytical results with maximum load resistances, maximum displacement and location, and failure mode of the compressive strength of 47.1 MPa for each inundation depth are listed in Table B-4. Relationship of force and maximum roof displacement under all inundation depths is shown in Figure B-13. The maximum resistances of the building slightly increase from 292.0 kN to 292.2 kN for the inundation depths of 0.24 m to 0.4 m. The lateral resistance of the building is controlled by the shear failure in Columns A3 and C3. The Columns A3 and C3 have the least shear capacity.

Table B-4. Maximum load resistances, maximum displacement and location, and failure mode of the compressive strength of 47.1 MPa

No.	Inundation Depth (m)	Max. Load (kN)	Max. Displacement		Failure mode
			(mm)	Location	
1	0.24	292.0	5.4	Col A3, C3	Shear failure in Columns A3 and C3
2	0.40	292.2	6.00	Col A3, C3	Shear failure in Columns A3 and C3
3	0.60	292.2	7.2	Col A3, C3	Shear failure in Columns A2 and C2
4	0.80	291.7	8.6	Col A3, C3	Shear failure in Columns A2 and C2
5	1.00	291.3	10.0	Col A3, C3	Shear failure in Columns A2 and C2
6	1.20	290.7	11.6	Col A3, C3	Shear failure in Columns A2 and C2
7	1.40	290.1	13.2	Col A3, C3	Shear failure in Columns A2 and C2
8	1.60	289.5	15.0	Col A3, C3	Shear failure in Columns A2 and C2
9	1.80	288.6	18.4	Col A3, C3	Shear failure in Columns A2 and C2
10	2.00	287.5	22.0	Col A3, C3	Shear failure in Columns A2 and C2
11	2.20	289.7	27.9	Col A3, C3	Shear failure in Column B2
12	2.40	289.9	56.3	Col A3, C3	Shear failure in Column B3
13	2.57	275.0	63.4	Col A3, C3	Flexural failure in Column B2
14	2.80	252.4	63.0	Col A3, C3	Flexural failure in Column B2
15	3.00	166.0	62.6	Col B3	Flexural failure in Column B2
16	3.20	151.4	63.1	Col B3	Flexural failure in Column B2

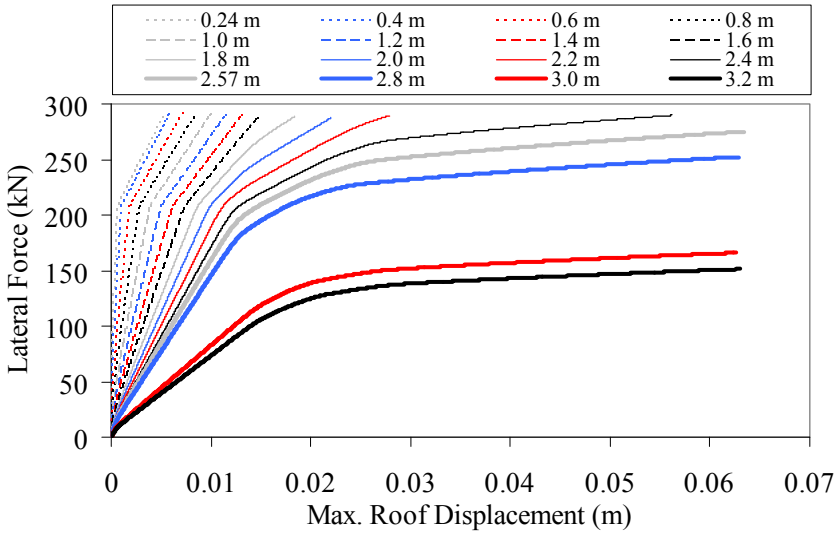

Figure B-13. Force and maximum roof displacement under tsunami of the compressive strength of 47.1 MPa

From tsunami inundation depths of 0.6 m to 2.0 m, the lateral resistances of the building are linearly decreasing from 292.2 kN to 287.4 kN, which are controlled by the shear failure in Columns A2 and C2. At this stage, the load is shared between the columns in each frame, so the shear failure occurs in the middle column. As shown in Figure B-14, the flexural moment of Column B2 is significantly increased. The stress of covering concrete in Column B2 is larger than 35 MPa at an inundation depth of about 2.2 m as shown in Figure B-15. The longitudinal reinforcement in Column B2 yields at an inundation depth of 1.8 m as shown in Figure B-16. Under an inundation depth of 2.2 m, the shear failure of Column B2 controls with the lateral resistance of 289.7 kN. The shear failure of Column B3 controls with the lateral resistance of 289.9 kN under an inundation depth of 2.4 m. From the stress-strain of covering concrete in Column B2, the flexural failure closely occurs

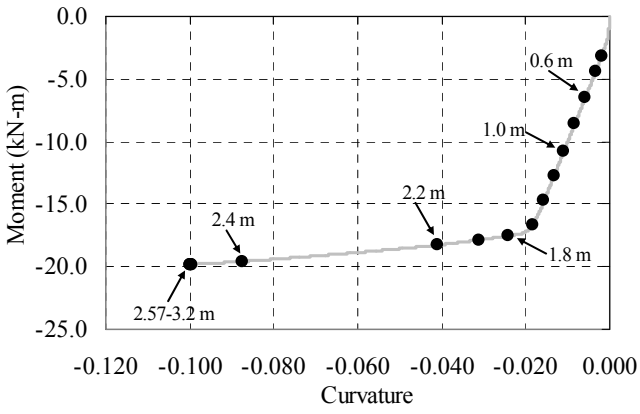

Figure B-14. Moment and curvature relationship of Column B2 under all inundation depths of the compressive strength of 47.1 MPa

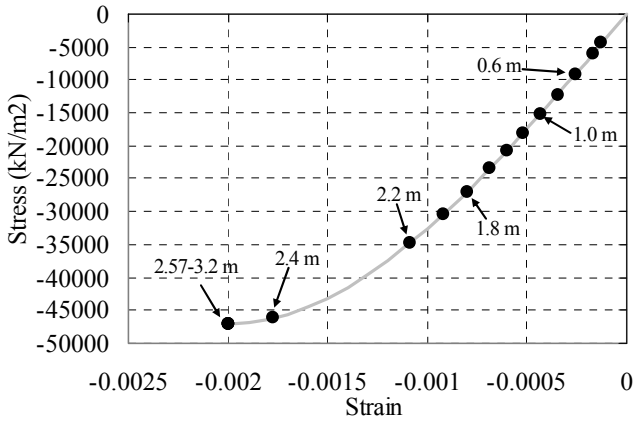

Figure B-15. Stress-strain relationship of covering concrete of Column B2 under all inundation depths of the compressive strength of 47.1 MPa

The failure mode of the building changes from a shear failure to a flexure failure in Column B2 at an inundation depth of 2.57 m with the lateral resistance of 275.0 kN. For inundation depths of 2.8 m to 3.2 m, the lateral resistances are controlled by the flexural failure in Column B2. The maximum resistances of the building are decreased according to inundation depth from 252.4 kN to 151.4 kN due to changing of failure mode. At inundation depths of 3.0 m and 3.2, tsunami acts on the roof beams, then the flexural failure occurs rapidly. The maximum resistance decreases significantly. Shear forces in columns are about 17.6 kN.

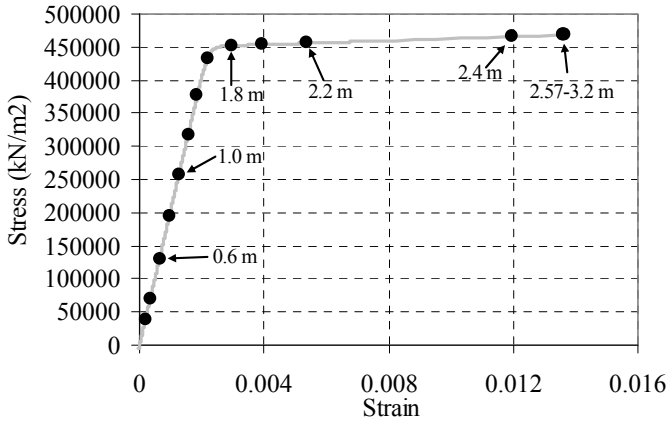

Figure B-16. Stress-strain relationship of reinforcement of Column B2 under all inundation depths of the compressive strength of 47.1 MPa

Appendix C
Building Responses of Various Arrangement Patterns of Walls

C.1 The responses of building with wall pattern Case a-c

The analytical results with maximum load resistance, maximum momentum flux (hu^2), maximum displacement and location, and failure mode of the wall pattern **Case a-c** for each inundation depth are listed in Table C-1. Relationship of force and inundation depth is shown in Figure C-1. The maximum resistances of the building increase from 161 kN to 202 kN for the inundation depths of 1.0 m to 2.8 m. The lateral resistances are controlled by the shear failure in Columns B1. For the inundation depths of 3.0 m to 3.2 m, the maximum resistances decrease from 237 kN to 228 kN controlled by the flexural failure in Columns B2.

Table C-1. Maximum load resistance, maximum momentum flux, maximum displacement and location, and failure mode of the wall pattern **Case a-c**

No.	Inundation Depth (m)	Max. Load (kN)	hu^2 (m^3/s^2)	Max. Displacement		Failure mode
				(mm)	Location	
1	1.00	161.6	174.45	5.9	Col B3	Shear failure in Columns B1
2	1.60	171.2	175.93	9.1	Col B3	Shear failure in Columns B1
3	2.00	179.2	181.34	11.7	Col B3	Shear failure in Columns B1
4	2.57	193.6	193.25	16.4	Col B3	Shear failure in Columns B1
5	2.80	202.3	201.11	19.3	Col B3	Shear failure in Columns B1
6	3.00	236.7	78.24	39.6	Col B3	Flexural failure in Column B2
7	3.20	228.0	47.58	40.9	Col B3	Flexural failure in Column B2

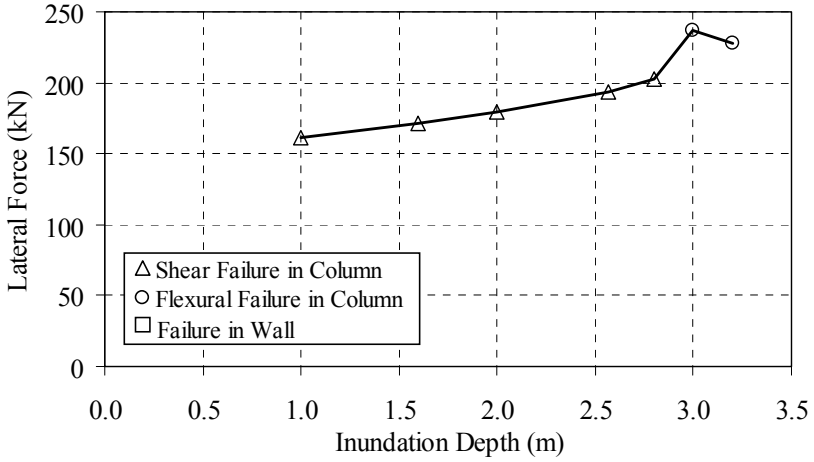

Figure C-1. Lateral force and inundation depth relationship of the wall pattern **Case a-c**

Table C-2. Sharing load between masonry infill walls and building frame of the wall pattern **Case a-c**

Case	h (m)	Max. Load (kN)	Load in Walls (%)			Load in Frame (%)	Sum
			Frame A	Frame B	Frame C		
1	1.00	161.6	6.9	0.0	6.9	86.2	100.0
2	1.60	171.2	10.1	0.0	10.1	79.7	100.0
3	2.00	179.2	12.5	0.0	12.5	75.0	100.0
4	2.57	193.6	16.0	0.0	16.0	68.0	100.0
5	2.80	202.3	17.7	0.0	17.7	64.7	100.0
6	3.00	236.7	32.7	0.0	32.7	34.5	100.0
7	3.20	228.0	35.4	0.0	35.4	29.2	100.0

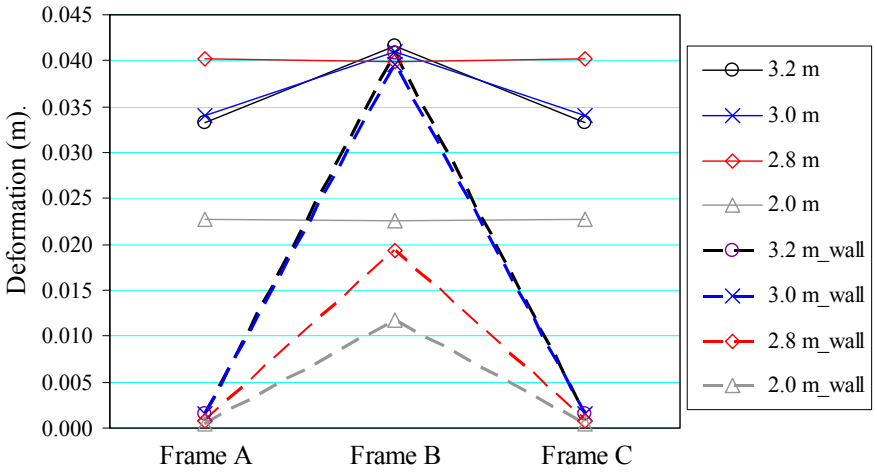

Figure C-2. Comparison of deformation of the middle frame between without wall and the wall pattern **Case a-c**

The sharing load between masonry infill walls and building frame of the wall pattern **Case a-c** of all inundation depths are listed in Table C-2. The masonry infill walls in Frames A and C share the load increasingly according to the inundation depth. The infill walls share the load about 14% at an inundation depth of 1.0 m. The load is shared to masonry infill walls up to 35% at an inundation depth of 2.8 m. At an inundation depth of 3.0 m, the masonry infill walls share the load about 65%, and 71% for the inundation depth of 3.2 m.

The comparison of the middle frame between without wall and the wall pattern **Case a-c** is shown in Figure C-2. The deformations of Frames A and C of the building with masonry infill walls for all inundation depths are very small. For Frame B without masonry infill wall, the deformations for inundation depths of 1.0 m to 2.8 m, which are controlled by the shear failure in column, are less than the deformations of the building without masonry infill wall about 50%. For the inundation depths of 3.0 m to 3.2 m controlled by the flexural failure in Column B2, the deformations of Frame B are almost equal to the deformations of the building without masonry infill wall.

C.2 The responses of building with wall pattern Case a-b1-c

The analytical results with maximum load resistance, maximum momentum flux (hu^2), maximum displacement and location, and failure mode of the wall pattern **Case a-b1-c** for each inundation depth are listed in Table C-3. Relationship of force and inundation depth is shown in Figure C-3. The maximum resistances increase from 145 kN to 225 kN for the inundation depths of 1.0 m to 2.8 m. The lateral resistances are controlled by the shear failure in Columns B1. For the inundation depths of 3.0 m to 3.2 m, the maximum resistances decrease from 531 kN to 228 kN controlled by the failure in Wall **b1**.

Table C-3. Maximum load resistance, maximum momentum flux, maximum displacement and location, and failure mode of the wall pattern **Case a-b1-c**

No.	Inundation Depth (m)	Max. Load (kN)	hu^2 (m^3/s^2)	Max. Displacement		Failure mode
				(mm)	Location	
1	1.00	144.5	194.9	0.6	Col B3	Shear failure in Columns A1
2	1.60	165.0	212.0	0.9	Col B3	Shear failure in Columns B1
3	2.00	183.1	231.6	1.2	Col B3	Shear failure in Columns B1
4	2.57	211.0	263.3	1.7	Col B3	Shear failure in Columns B1
5	2.80	225.4	280.1	1.9	Col B3	Shear failure in Columns B1
6	3.00	531.0	188.1	13.3	Col B3	Failure in Wall **b1**
7	3.20	502.5	109.5	13.3	Col B3	Failure in Wall **b1**

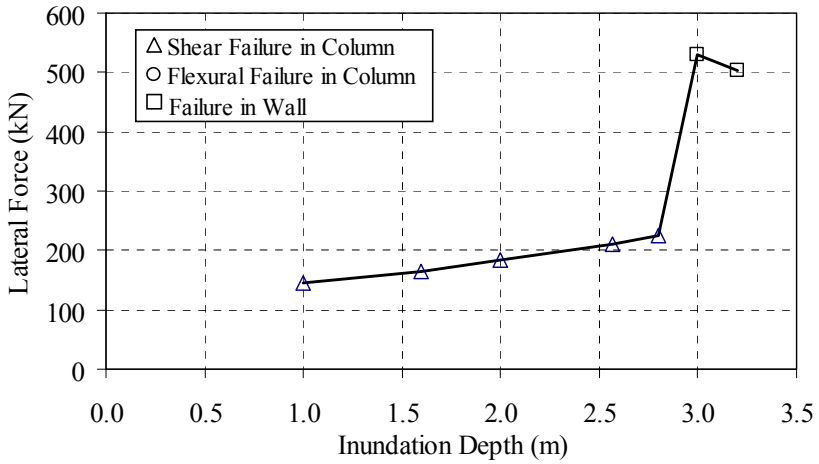

Figure C-3. Lateral force and inundation depth relationship of the wall pattern **Case a-b1-c**

Table C-4. Sharing load between masonry infill walls and building frame of the wall pattern **Case a-b1-c**

Case	h (m)	Max. Load (kN)	Load in Walls (%)			Load in Frame (%)	Sum
			Frame A	Frame B	Frame C		
1	1.00	144.5	5.3	9.8	5.3	79.6	100.0
2	1.60	165.0	7.9	14.4	7.9	69.8	100.0
3	2.00	183.1	9.7	17.7	9.7	62.9	100.0
4	2.57	211.0	11.8	21.4	11.8	54.9	100.0
5	2.80	225.4	12.7	23.0	12.7	51.6	100.0
6	3.00	531.0	21.9	36.6	21.9	19.6	100.0
7	3.20	502.5	23.3	38.7	23.3	14.7	100.0

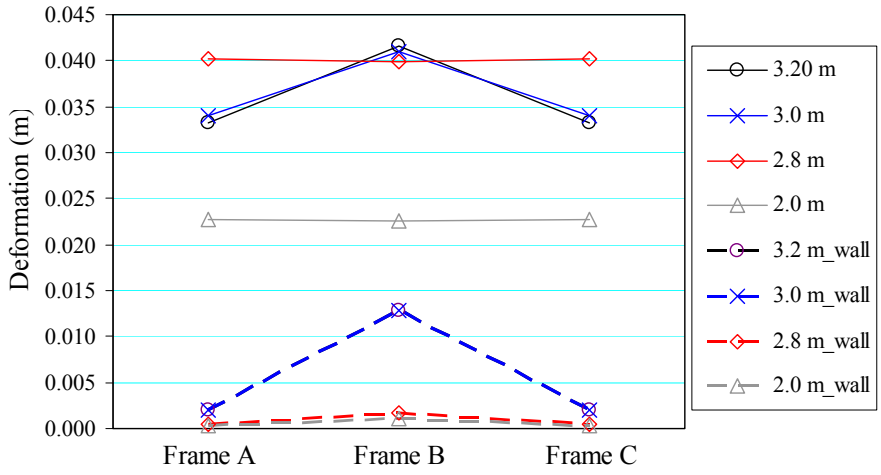

Figure C-4. Comparison of deformation of the middle frame between without wall and the wall pattern **Case a-b1-c**

The sharing load between masonry infill walls and building frame of the wall pattern **Case a-b1-c** of all inundation depths are listed in Table C-4. The masonry infill walls share the load increasingly according to the inundation depth. The wall in Frame B shares the load highest. The infill walls share the load about 20% at an inundation depth of 1.0 m. The load is shared to masonry infill walls up to 48% at an inundation depth of 2.8 m. At an inundation depth of 3.0 m, the masonry infill walls share the load about 80%, and up to 85% for the inundation depth of 3.2 m.

The comparison of the middle frame between without wall and the wall pattern **Case a-b1-c** is shown in Figure C-4. The deformations of Frames A and C of the building with masonry infill walls for all inundation depths are very small. For Frame B with masonry infill wall in the front span, the deformations for inundation depths of 1.0 m to 2.8 m, which are controlled by the shear failure in column, are also small as both edge frames. For the inundation depths of 3.0 m to 3.2 m controlled by the failure in Wall **b-1**, the deformations of Frame B increase largely which are about 30% of the deformation of the building without masonry infill wall.

C.3 The responses of building with wall pattern Case a-b2-c

The analytical results with maximum load resistance, maximum momentum flux (hu^2), maximum displacement and location, and failure mode of the wall pattern **Case a-b2-c** for each inundation depth are listed in Table C-5. Relationship of force and inundation depth is shown in Figure C-5. The maximum resistances increase from 145 kN to 186 kN for the inundation depths of 1.0 m to 2.0 m. The lateral resistances are controlled by the shear failure in Columns A1. The maximum resistances increase from 213 kN to 228 kN for the inundation depths of 2.57 m to 2.8 m. The lateral resistances are controlled by the shear failure in Columns B1. For the inundation depths of 3.0 m to 3.2 m, the maximum resistances decrease from 527 kN to 500 kN controlled by the failure in Wall **b2**.

Table C-5. Maximum load resistance, maximum momentum flux, maximum displacement and location, and failure mode of the wall pattern **Case a-b2-c**

No.	Inundation Depth (m)	Max. Load (kN)	hu^2 (m^3/s^2)	Max. Displacement		Failure mode
				(mm)	Location	
1	1.00	145.0	195.6	0.5	Col B3	Shear failure in Columns A1
2	1.60	166.2	213.5	0.8	Col B3	Shear failure in Columns A1
3	2.00	185.5	234.7	1.1	Col B3	Shear failure in Columns A1
4	2.57	213.4	266.3	1.5	Col B3	Shear failure in Columns B1
5	2.80	228.0	283.4	1.7	Col B3	Shear failure in Columns B1
6	3.00	526.7	186.6	12.5	Col B3	Failure in Wall **b2**
7	3.20	499.2	108.8	12.5	Col B3	Failure in Wall **b2**

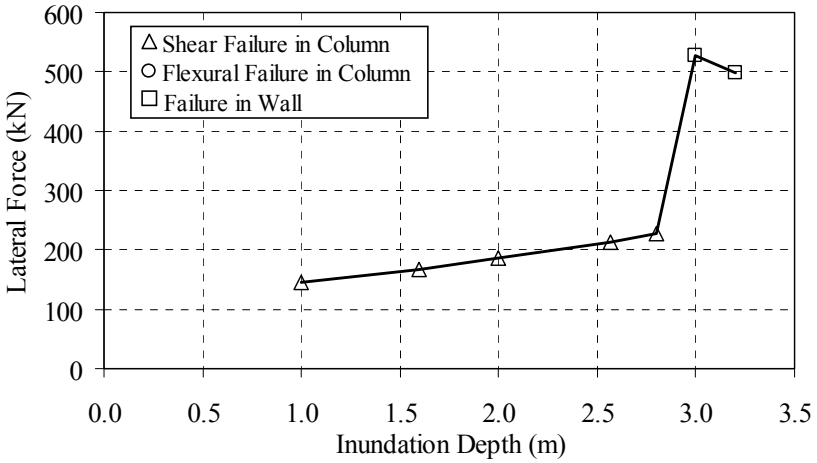

Figure C-5. Lateral force and inundation depth relationship of the wall pattern **Case a-b2-c**

Table C-6. Sharing load between masonry infill walls and building frame of the wall pattern **Case a-b2-c**

Case	h (m)	Max. Load (kN)	Load in Walls (%)			Load in Frame (%)	Sum
			Frame A	Frame B	Frame C		
1	1.00	145.0	5.4	9.9	5.4	79.2	100.0
2	1.60	166.2	8.0	14.6	8.0	69.3	100.0
3	2.00	185.5	9.8	18.0	9.8	62.3	100.0
4	2.57	213.4	11.9	21.7	11.9	54.6	100.0
5	2.80	228.0	12.8	23.3	12.8	51.2	100.0
6	3.00	526.7	21.9	36.9	21.9	19.3	100.0
7	3.20	499.2	23.2	38.9	23.2	14.6	100.0

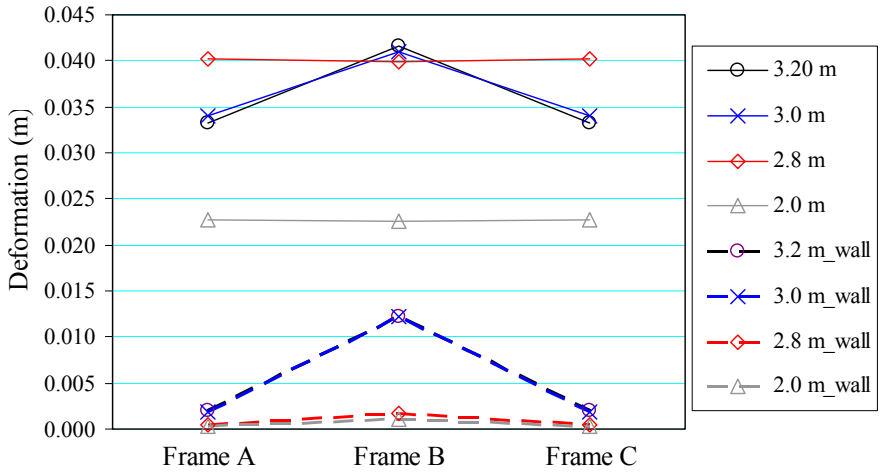

Figure C-6. Comparison of deformation of the middle frame between without wall and the wall pattern **Case a-b2-c**

The sharing load between masonry infill walls and building frame of the wall pattern **Case a-b2-c** of all inundation depths are listed in Table C-6. The masonry infill walls share the load increasingly according to the inundation depth. The wall in Frame B shares the load highest. The infill walls share the load about 21% at an inundation depth of 1.0 m. The load is shared to masonry infill walls up to 49% at an inundation depth of 2.8 m. At an inundation depth of 3.0 m, the masonry infill walls share the load about 81%, and up to 85% for the inundation depth of 3.2 m.

The comparison of the middle frame between without wall and the wall pattern **Case a-b2-c** is shown in Figure C-6. The deformations of Frames A and C of the building with masonry infill walls for all inundation depths are very small. For Frame B with masonry infill wall in the back span, the deformations for inundation depths of 1.0 m to 2.8 m, which are controlled by the shear failure in column, are also small as both edge frames. For the inundation depths of 3.0 m to 3.2 m controlled by the failure in Wall **b-2**, the deformations of Frame B increase largely which are about 30% of the deformation of the building without masonry infill wall.

C.4 The responses of building with wall pattern Case a-b-c

The analytical results with maximum load resistance, maximum momentum flux (hu^2), maximum displacement and location, and failure mode of the wall pattern **Case a-b-c** for each inundation depth are listed in Table C-7. Relationship of force and inundation depth is shown in Figure C-7. The maximum resistances increase from 108 kN to 171 kN for the inundation depths of 1.0 m to 2.8 m. The lateral resistances are controlled by the shear failure in Columns A1. The maximum resistance increases largely to 740 kN at an inundation depth of 3.0 m. The lateral resistance is controlled by the shear failure in Columns B1. For the inundation depth of 3.2 m, the maximum resistance increases to 900 kN controlled by the failure in Wall **b2**.

Table C-7. Maximum load resistance, maximum momentum flux, maximum displacement and location, and failure mode of the wall pattern **Case a-b-c**

No.	Inundation Depth (m)	Max. Load (kN)	hu^2 (m^3/s^2)	Max. Displacement		Failure mode
				(mm)	Location	
1	1.00	108.5	195.2	0.1	Col B3	Shear failure in Columns A1
2	1.60	124.3	212.9	0.2	Col B3	Shear failure in Columns A1
3	2.00	138.6	233.8	0.3	Col B3	Shear failure in Columns A1
4	2.57	159.7	265.6	0.4	Col B3	Shear failure in Columns A1
5	2.80	171.0	283.3	0.5	Col B3	Shear failure in Columns A1
6	3.00	740.4	282.4	6.5	Col B3	Shear failure in Columns B1
7	3.20	900.8	205.4	12.9	Col B3	Failure in Wall **b2**

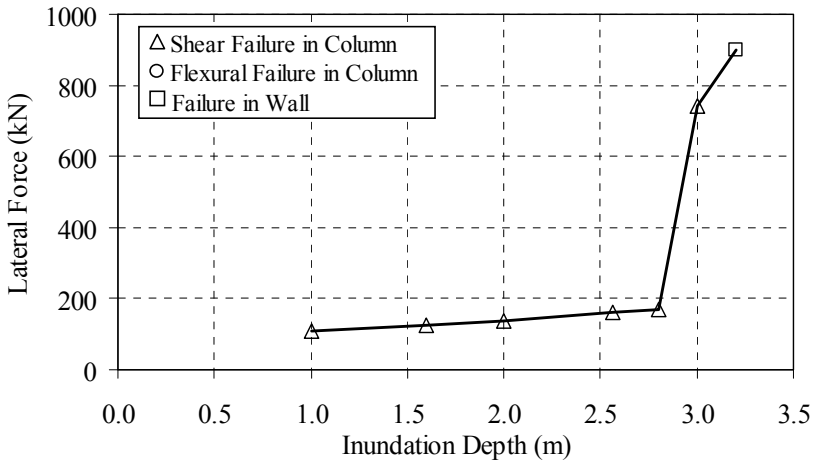

Figure C-7. Lateral force and inundation depth relationship of the wall pattern **Case a-b-c**

Table C-8. Sharing load between masonry infill walls and building frame of the wall pattern **Case a-b-c**

Case	h (m)	Max. Load (kN)	Load in Walls (%)			Load in Frame (%)	Sum
			Frame A	Frame B	Frame C		
1	1.00	108.5	6.9	7.0	6.9	79.2	100.0
2	1.60	124.3	10.2	10.3	10.2	69.3	100.0
3	2.00	138.6	12.6	12.6	12.6	62.2	100.0
4	2.57	159.7	15.2	15.2	15.2	54.3	100.0
5	2.80	171.0	16.4	16.4	16.4	50.9	100.0
6	3.00	740.4	22.3	41.8	22.3	13.7	100.0
7	3.20	900.8	23.3	43.0	23.3	10.4	100.0

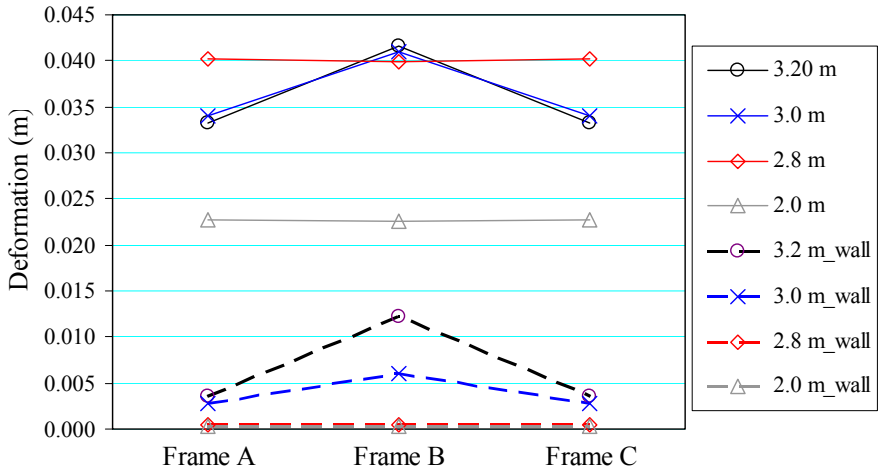

Figure C-8. Comparison of deformation of the middle frame between without wall and the wall pattern **Case a-b-c**

The sharing load between masonry infill walls and building frame of the wall pattern **Case a-b-c** of all inundation depths are listed in Table C-8. The masonry infill walls share the load increasingly according to the inundation depth. The wall in Frame B shares the load highest. The infill walls share the load about 21% at an inundation depth of 1.0 m. The load is shared to masonry infill walls up to 49% at an inundation depth of 2.8 m. At an inundation depth of 3.0 m, the masonry infill walls share the load about 86%, and up to 90% for the inundation depth of 3.2 m.

The comparison of the middle frame between without wall and the wall pattern **Case a-b-c** is shown in Figure C-8. The deformations of Frames A and C of the building with masonry infill walls for all inundation depths are very small. For Frame B, the deformations for inundation depths of 1.0 m to 2.8 m, which are controlled by the shear failure in column, are also small as both edge frames. For the inundation depth of 3.2 m controlled by the failure in Wall **b-2**, the deformations of Frame B increase largely which are about 30% of the deformation of the building model without masonry infill wall.

VITAE

Piyawat Foytong was born in Yasothon, Thailand on November 19, 1982. He received a Bachelor of Engineering degree from the Department of Civil Engineering, Khon Kaen University, Thailand in 2004. He received a Master of Engineering degree from the Department of Civil Engineering, Chulalongkorn University in 2007. In 2008, he received a scholarship from the Office of the Higher Education Commission, Ministry of Education, Thailand to continue his studies in a doctoral program at the Department of Civil Engineering, Chulalongkorn University. While studying, he worked as a research assistant under the supervision of Assistant Professor Anat Ruangrassamee. During his study, he was a visiting research student with Associated Professor Gaku Shoji at University of Tsukuba, Japan from September, 2011 until April, 2012. His research concerns effect of tsunamis on structures and tsunami risk assessment.